Propeller Slipstream Effects on Longitudinal Static Stability

Effect of the Rethorst Correction at the Horizontal Stabilizer

Thomas Keesom

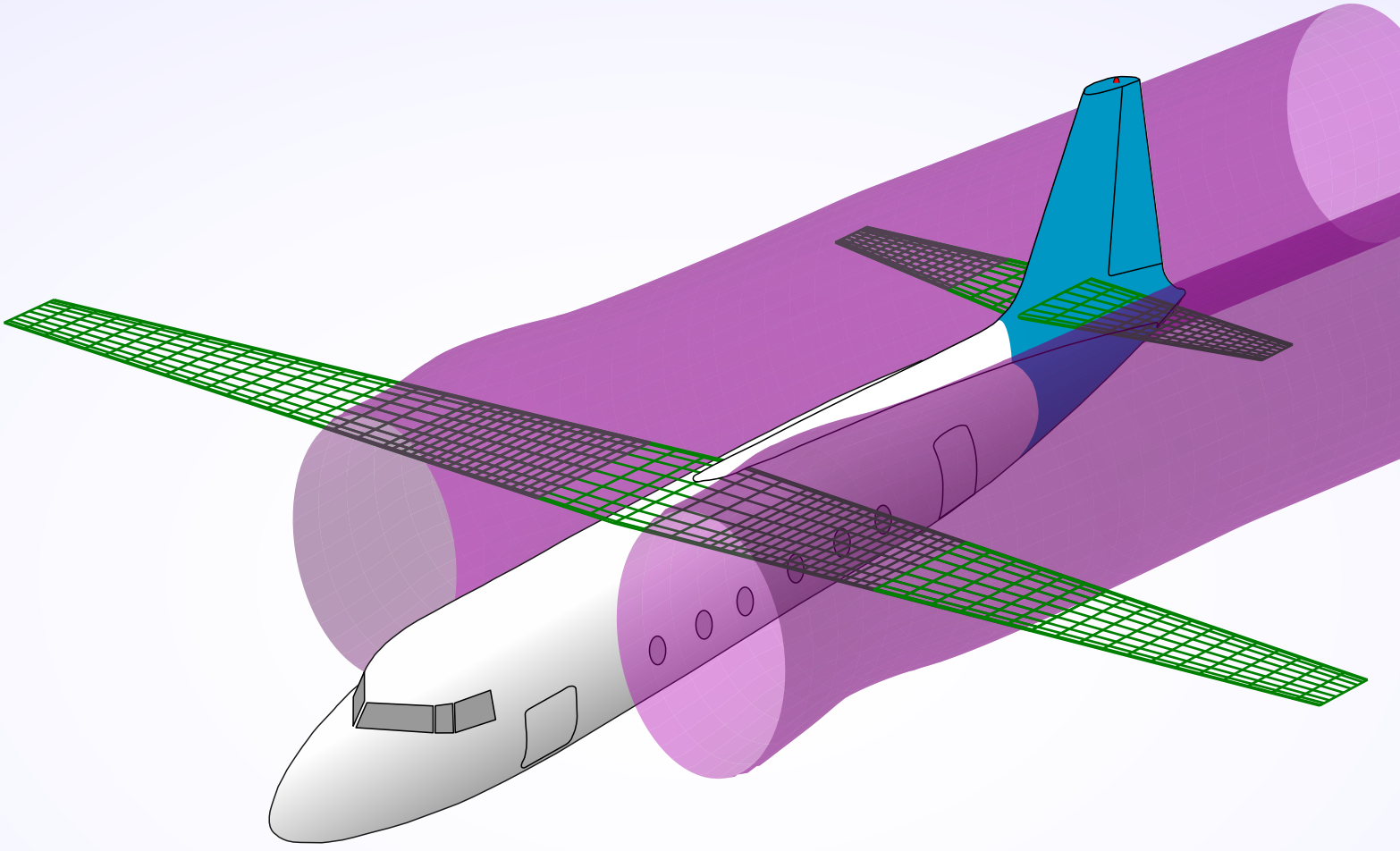

TU Delft Delft University of Technology

Propeller Slipstream Effects on Longitudinal Static Stability

Effect of the Rethorst Correction at the Horizontal Stabilizer

by

Thomas Keesom

in partial fulfillment of the requirements for the degree of

Master of Science
in Aerospace engineering

at the Delft University of Technology,
to be defended publicly on Thursday July 6, 2023 at 13:30.

Student number:	4668170	
Project duration:	August 30, 2021 - July 6, 2023	
Thesis committee:	Dr. ir. M.F.M. Hoogreef,	TU Delft, supervisor
	Dr. ir. R. Vos,	TU Delft, chairman
	Dr. ir. W.J. Baars,	TU Delft, external

TU Delft

Preface

This work counts toward the deliverables agreed upon to obtain the degree of Master of Science in Aerospace Engineering at the Delft University of Technology (TU Delft) and marks the end of my career as a student. My interest in academics has lead to me wanting to do a research oriented thesis project. With the ultimate goal of discovering if academics is a career I would like to pursue. The project brought struggles and challenges with every step of advancement. Despite the challenging aspects, I thoroughly enjoyed the research topic. Working on this research topic has made me realize how much I enjoy doing research.

One of my goals of this thesis project was to do a lot of other extra-curricular activities in parallel. It was important to me to have variety is my daily work schedule. During the second semester of the 2021/2022 academic year, I was the project manager for the Aircraft Manufacturing Laboratory Team 11 where I worked on an RV12 kit aircraft together with seven other enthusiastic students. This project was part of the AE4ASM517 course at TU Delft. I did this course purely for fun. In addition, I was a teaching assistant for Python during the time of the Aircraft Manufacturing Laboratory project. After having been a teaching assistant for Python in the academic year of 2020/2021, which was a great experience, I could not resist to become a Python teaching assistant again in the 2021/2022 academic year after being personally asked.

At the start of the 2022/2023 academic year, I went to San Diego for a six month internship at the San Diego State University to experience the world of academics in the United States. I knew I wanted to go abroad and return to the United States for my internship ever since I went abroad for my minor at the Embry-Riddle Aeronautical University in Daytona Beach, Florida, United States back during the fall of 2019. The internship at San Diego State University taught me a lot more about the process of doing research and gave me the necessary skills to be able to finish this thesis project a few months after I returned to Delft from San Diego.

There are quite some people that I would like to thank. Firstly, my sincerest gratitude goes to my supervisor Maurice Hoogreef, who provided me with the support, the advise, the tools and the expertise necessary for this project. Secondly, I would like to thank Alberto Ruiz Garcia for the incredible one-on-one support with regards to the technical and numerical aspect of this project. The amount of time and effort he put into supporting and helping me in general is indescribable. I would also like to thank Leo Veldhuis, Tomas Sinnige and Robert Nederlof for their involvement in the project. Lastly, a big thanks to my family and friends for the never ending and continuous support.

Thomas Keesom
Delft, July 2023

Summary

The aerospace and aviation industry experiences the trend of the transition back to propeller propulsion as a result of climate goals to battle global warming. Propeller propulsion beats jet propulsion in terms of propulsion efficiency, making propeller relevant for sustainable aircraft design. The slipstream of propellers interacts with the aircraft airframe. The aircraft Longitudinal Static Stability (LSS) and control can be drastically affected when the slipstream interacts with the horizontal stabilizer. Modeling the interaction effects of the propeller slipstream on the horizontal stabilizer is an important aspect of the aircraft design process, which requires a timely and accurate prediction of an aircraft geometry's LSS that constantly changes with design iterations. Vortex Lattice Methods (VLMs) fit these requirements and are often utilized during the beginning stages of aircraft design. However, VLMs have resulted in overpredictions for wing lift in the case where a wing is engulfed in a jet of higher velocity compared to the free stream, such as a propeller slipstream. Rethorst derived a correction to correct for this overprediction in lift under certain assumptions. Applying the so-called Rethorst correction in VLMs results in a great improvement in wing lift predictions for the described scenario, that show great agreement with experimental measurements and Computational Fluid Dynamics (CFD) simulations. The Rethorst correction thus has the potential to accurately predicting the stabilizer lift contribution and improve VLM LSS predictions, when applying the Rethorst correction to a slipstream engulfed horizontal stabilizer. This thesis investigates the applicability of the Rethorst correction at the horizontal stabilizer.

The Rethorst correction application at the horizontal stabilizer requires the derivation assumptions to apply and the stabilizer lift needs to be predicted accurately as a result of applying the correction. The most questionable assumption being the stabilizer symmetrically extending through the propeller slipstream. The slipstream position relative to the stabilizer is dictated by the slipstream deflection, which rarely causes the slipstream center line to line up with the horizontal stabilizer. The Rethorst correction has been assumed to be applicable in situations where the vertical distance between the slipstream center line and wing to propeller radius ratio is low. The scope of this thesis is reduced to conventional high wing, low stabilizer and dual Inboard (IB) propeller configuration aircraft in the cruise condition and configuration, in an effort to make the propeller slipstreams engulf the stabilizer and minimize the vertical distance of the slipstream center line to the stabilizer. The accurate prediction of the stabilizer lift as a result of the Rethorst correction is tested in this thesis by considering the average dynamic pressure and downwash angle at the stabilizer, since an accurate prediction of these quantities mainly dictate the stabilizer lift contribution.

A VLM code is used to tackle the research questions by means of an aircraft case study on the Fokker F-27 aircraft. A slipstream tube model is used to model the induced velocities of the propeller slipstream on the wing and the stabilizer. The exact propeller geometry used for the F-27 and its performance is not available in literature, resulting in a replacement model being created. This inherited code is expanded with the ability to model the horizontal stabilizer and to apply the Rethorst correction to it. With these implementations, the code is renamed to the Aircraft Longitudinal Interaction and Moment Evaluator (ALIME).

The F-27 case study consisted of a propellers off and propellers on analysis. The propellers off analysis serves to validate the implemented geometry of the F-27 and the LSS prediction capability of ALIME. Close predictions for the LSS of the F-27 are obtained by ALIME during the propellers off analysis, as a result of close stabilizer lift and LSS contribution predictions. However, when the propeller is introduced in the propellers on analysis, the change in LSS prediction by ALIME with respect to the propellers off analysis opposes the trend of wind tunnel measurements by existing wind tunnel data. ALIME predicts an increase in LSS with respect to the propeller off analysis, while the wind tunnel experiments show a decrease in LSS. The main reason for the opposite trend in LSS prediction with respect to wind tunnel data is caused by an opposite trend in the predicted average downwash angle at the stabilizer. ALIME predicts the average downwash at the stabilizer to decrease with the introduction of the propeller, increasing the stabilizer's lift contribution and thus the LSS. However the propeller slipstream should increase the average downwash experienced by the stabilizer and decrease its lift and LSS contribution. The average dynamic pressure at the stabilizer is predicted to be overestimated when referencing flight test data on the Fokker 50. Providing another reason why the stabilizer lift contribution is not correctly predicted by ALIME during the propellers on analysis.

This thesis has failed to accurately predict the stabilizer lift contribution using the Rethorst correction and can therefore not draw a conclusion on the applicability of the Rethorst correction at the stabilizer. However, the thesis contributes to the knowledge and research necessary to be able to draw a conclusion.

Applying the jet correction to the wing is found to be beneficial to minimize the distance between the slipstream center line and the stabilizer and thus contributes to the applicability of the Rethorst correction at the stabilizer. Despite this finding, no knowledge is available in literature that supports that the Rethorst correction results in accurate lift predictions in VLMs outside its assumption scope, including when the vertical distance from the slipstream center line is larger than zero. An extra study is thus necessary on the applicability of the Rethorst correction outside is assumption scope, with emphasis on the wing not symmetrically extending symmetrically through the propeller slipstream.

The uncertainty in the propeller geometry and performance largely contributes to the over estimation of the slipstream induced velocity predictions, because the induced velocities are a function of the predicted propeller blade loading. A first step to improve the slipstream induced velocity predictions requires a more representative F-27 propeller model. The used propeller geometry and performance data need to be obtained from the original source. However, effects which are not captured by the slipstream tube model will likely still cause the induced velocities to not match wind tunnel data, such as the nacelle wake inside the slipstream. A deeper analysis on the potential of the slipstream tube model to predict the slipstream induced velocities at the stabilizer is thus required.

Lastly, the wrong trend of a decreasing average downwash at the stabilizer with the introduction of the propeller results from a wrong trend in the vertical induced velocities by the wing and stabilizer surfaces. The propeller slipstream interaction with the wing should increase the wing circulation and thus increase the vertical induced velocities instead of decreasing them. Hinting possible modeling issues in ALIME, which require more research on ALIME.

Contents

List of Figures

List of Tables

Acronyms

2D	Two-Dimensional
3D	Three-Dimensional
a.c.	aerodynamic center
AIC	Aerodynamics Influence Coefficient
ALIME	Aircraft Longitudinal Interaction and Moment Evaluator
AoA	Angle of Attack
AR	Aspect Ratio
BEM	Blade Element Method
CCW	Counter Clock Wise
CFD	Computational Fluid Dynamics
CP	Control Point
CW	Clock Wise
FN	Fuselage-Nacelle
HTC	High Thrust Case
IB	Inboard
ID	IB Down
IU	IB Up
LE	Leading Edge
LL	Lifting Line
LSS	Longitudinal Static Stability
LTC	Low Thrust Case
MAC	Mean Aerodynamic Chord
NLL	Nationaal Luchtvaart Laboratorium
OB	Outboard
RPM	Rotations Per Minute
SRF	Swirl Recovery Factor
TE	Trailing Edge
TU Delft	Delft University of Technology
VLM	Vortex Lattice Method
WFN	Wing, Fuselage and Nacelle
WTMP	WingTip Mounted Propeller
XFLR5	X FLyeR 5

Symbols

A	Axial force	N
B	Number of propeller blades	–
C	Coefficient	–
D	Diameter	m
I'	First order derivative of I	–
I	Bessel function of second kind	–
J	Advance ratio	–
K'	First order derivative of K	–
K	Bessel function of the second kind	–
N	Normal force	N
P	Power	W
P	Arbitrary point in space	–
Q	Torque	N m
R	Radius	m
S	Surface area	m^2
T	Thrust coefficient	–
T	Thrust	N
V	Velocity	$m s^{-1}$
$\bar{V}$	Average velocity	$m s^{-1}$
$\bar{\varepsilon}$	Average downwash angle	°
$\bar{c}$	Mean Aerodynamic Chord (MAC)	m
$\bar{q}$	Average dynamic pressure	Pa
Γ	Circulation	–
α	AoA	°
$\bar{\alpha}$	Average AoA	°
β	Pitch	°
$\mathbf{\Gamma}$	Circulation vector	–
η	Efficiency	–
γ	Vorticity	–
$\lambda\beta$	An integration variable for the odd part of the Rethorst correction	–
λ	An integration variable for the odd part of the Rethorst correction	–
$\mathbb{S}$	Sears function	–
$\mathbf{C}$	Aerodynamics Influence Coefficient (AIC) matrix	–
$\mathbf{G}$	Rethorst correction matrix	–
$\mathbf{V}$	Velocity vector	$m s^{-1}$
$\mathbf{r}$	Distance vector in Three-Dimensional (3D) space	m
$\lvert\mathbf{r}\rvert$	Magnitude of $\mathbf{r}$	m
μ	Velocity ratio: V_o / V_j	–
ν	Polynomial order	–
ϕ	Propeller azimuth	°
ρ	Density	$kg m^{-3}$
σ	Reduced frequency	Hz
θ	Propeller twist	°
ε	Wing twist	°
ε	Error	–
ε	Downwash angle	°
ξ	Non-dimensionalized x-coordinate, with the propeller radius: x_{CP} / R_p	–
ζ	Non-dimensionalized y-coordinate, with the propeller radius: y_{CP} / R_p	–

b	Wing span	m
c	Chord length	m
e	Spanwise location of the left horse shoe vortex egde	m
f'	Derivative of the function f	–
f	Spanwise location of the right horse shoe vortex egde	m
f	Function	–
g	Airfoil camber line	m
i	Incidence angle	°
l	Moment arm	m
m	Number of spanwise VLM panels	–
n	Number of chordwise VLM panels	–
n	Propeller rotation speed	Hz
p	Order of Bessel function	–
q	Dynamic pressure	Pa
r	Propeller radial stations	m
t	Time	s
x	Coordinate along the aircraft longitudinal axis	m
y	Coordinate along the aircraft lateral axis	m
z	Coordinate along the aircraft vertical axis	m

Subscripts

0	Zero lift
CP	Control Point (CP) location
D	Drag force
L	Lift force in 3D
M	Moment in 3D
N	Normal force
P	Power
Q	Torque
T	Thrust
α	Derivative with respect to the AoA: $\frac{d}{d\alpha}$
∞	Free stream
v	Belonging to the method by Conway
$a.c.$	Aerodynamic center
a	Axial
c	Coefficient
d	Sectional drag force
eff	Effective
$even$	Even part
f	Fuselage
hh	Horizontal stabilizer-on-horizontal stabilizer VLM horse shoe vortex interaction
hub	Propeller hub
hw	Horizontal stabilizer-on-wing VLM horse shoe vortex interaction
h	Horizontal stabilizer
ind	Induced
i	Counter index
j	Inside the jet
l	Sectional lift force
max	Maximum
n	Nacelle
n	Normal/Orhtogonal
odd	Odd part
o	Outside the jet
p	Propeller
ref	Reference point
r	Root
s	Slipstream
tot	Total
t	Tip
t	Tangential
wfn	Wing-fuselage-nacelle
wh	Wing-on-horizontal stabilizer VLM horse shoe vortex interaction
ww	Wing-on-wing VLM horse shoe vortex interaction
w	Wing
x	In the x-direction
y	In the y-direction
z	In the z-direction

Superscripts

$'$	Different Definition
$'$	Distribution
$*$	The difference between the *farfield* and *3D* methods when calculating the AICs
$3D$	Calculated using the *3D* method to calculate the AICs
$calc$	Calculated using semi-empirical methods
far	Calculated using the *farfield* method to calculate AICs
m	In the m-direction
num	Evaluated numerically using the ALIME
n	In the n-direction
ref	Reference value
tun	Measured values in the wind tunnel

1

Introduction

Global warming is accounting for increasing the earth's average temperature compared to pre-industrialization levels. It will result in permanent and irreversible effects on climate change if the average temperature is allowed to rise above 1.5°C. Decarbonization lies at the heart of battling global warning. Goals set for decarbonization by the European Commission state to reduce CO_2, NO_x and noise emissions by 75%, 90% and 65% respectively by the year 2050 relative to 2000 [14].

The climate goals have resulted in a trend within the field of aerospace and aviation that demand more efficient and sustainable aircraft designs and means of propulsion. One current trend involves the transition back to propeller propulsion. Propellers have higher propulsive efficiency compared to jet propulsion [31], which is achieved by the small acceleration of a larger amount of air in the propeller slipstream, compared to a large acceleration of a small amount of air inside a jet. The propeller slipstream however, interacts with the airframe of the aircraft. The interaction effects are caused mainly by the induced velocities of the propeller slipstream. When interacting with the aircraft's stabilizing surfaces, propeller slipstream effects can drastically affect the static stability and control characteristics of conventional aircraft [45, 38, 39]. Static stability, or LSS specifically, is a main subject of interest during the aircraft certification and design process. In fact, certification requirements state that an aircraft should be longitudinally stable in all conditions normally encountered in service [2].

LSS is mainly determined by the lift contribution of the horizontal stabilizer when considering conventional configuration aircraft. Conventional meaning a main wing with IB mounted propellers near the middle of the fuselage and a horizontal stabilizer at the rear. The horizontal stabilizer generates a corrective lift contribution when the aircraft encounters a disturbance in its pitch. If an aircraft is longitudinally statically stable, a pitch disturbance results in a stabilizer lift contribution that then creates a pitch change opposing the disturbance.

Understanding how the stabilizer generates lift requires an understanding of the flow field at and behind the wing in the presence of the propeller slipstream. The flow field at the wing, between the wing and the stabilizer and the final flow field encountered by the horizontal stabilizer are now individually discussed for conventional configuration aircraft featuring tractor IB propellers.

The flow field at the wing is defined by the wing, propeller slipstream and fuselage interaction. The propeller slipstream interacts with the main wing after the slipstream is generated by the propeller. The propeller slipstream has an axial and tangential flow component, which both interact with the main wing. The axial flow component locally increases the dynamic pressure over the wing, locally increasing the lift. The tangential flow component of the slipstream locally increases and decreases the wing AoA at the side of the up and down going propeller blade respectively. The local AoA increase and decrease lead to a local increase and decrease in lift on the side of the up and down going blades respectively [50, 54].

The main wing also directly interacts with the propeller slipstream. The wing recovers some of the swirl in the propeller slipstream as it moves over the wing. Swirl recovery occurs when some of the tangential flow in the slipstream is straightened out by the presence of the main wing, resulting in a suction force at the wing LE that acts as additional thrust [54]. Furthermore, propeller installation height also affects the wing lift in two ways. Firstly, the relative position of the contracting slipstream directly behind the propeller disk and the main wing influences the local AoA experienced by the wing. Secondly, the installation height of the propeller

with respect to the main wing determines how much of the slipstream passes over and under the wing, which affects the wing lift depending on what fraction of the slipstream passes over and under the wing [54]. Also, the slipstream partially passing over and under the wing effectively dissects the slipstream. This dissection of the propeller slipstream affects the slipstream shape by means of slipstream shearing. Cross flows present on the upper and lower wing surface cause the two half of the propeller slipstream to move along the wing axis, changing the sectional slipstream properties [50]. Additionally, the propeller slipstream is deflected vertically by the induced velocities as a result of the presence of other aircraft components. The circulation generated by the main wing as a result of its lift creates in an upwash in front and a downwash behind the wing. This up- and downwash vertically deflects the propeller slipstream up in front of the wing and down behind the wing. In return, the downwash field of the wing is also affected by the presence of the propeller slipstream. The local lift increase on the wing due to the axial flow component of the slipstream results in an increased downwash behind the wing [50, 23]. The presence of the fuselage also effects the wing lift distribution, thus also affecting the wing downwash, further affecting the slipstream deflection. This interaction mainly occurs in the IB area of the wing that is closest to the fuselage [22, 54, 32].

The flow field between the wing and horizontal stabilizer is mainly determined by the downwash field created by the wing as a result of the interaction with the fuselage and propeller slipstream. The vertical deflection of the propeller slipstream in this flow field is dictated by the downwash field as a result of the wing, fuselage and propeller slipstream interactions. The slipstream properties change as the slipstream travels downstream. On its way to the horizontal stabilizer, the propeller slipstream tangential and axial flow momentum diffuses [50]. When seeing the propeller slipstream as a turbulent jet, the slipstream momentum and sectional flow properties get spread out as a function of travel distance of the slipstream [18, 37].

Once the flow reaches the horizontal stabilizer, its effective AoA is lowered as a result of the wing downwash field. How much downwash the horizontal stabilizer locally receives is a function of the wing lift distribution. Lowering the effective AoA lowers the lift contribution of the horizontal stabilizer, decreasing the LSS. Although diffused, the increased dynamic pressure in the propeller slipstream increases the lift contribution of the horizontal stabilizer, increasing its LSS contribution, provided that the propeller slipstream hits the horizontal stabilizer at least partially. The downwash field behind the wing and the dynamic pressure in the propeller slipstream are both a function of the propeller power setting. The LSS is therefore also a function of propeller power setting. [39, 17].

With regards to representing the mentioned aerodynamic interaction effects for propeller slipstream interactions, one can look at models of increasing fidelity. The lowest fidelity modeling involves preliminary calculations, which are based on large data sets of aircraft performance of already existing aircraft, making these calculations of an empirical nature. The input for these calculations is the basic aircraft geometry. A general limitation of empirical calculation is the accuracy of their predictions, limiting to preliminary design stage in aircraft design. Empirical calculations to predict the performance of an aircraft design are described in sources such as Roskam and Torenbeek [43, 52], covering calculations concerning the prediction of aircraft aerodynamic performance, structural weight and more.

Obert presents an empirical method to estimate the effects of slipstream on the LSS of multi-propeller aircraft. The goal is to obtain a first estimate of the increase in lift due to the propeller slipstream, change in tail-off pitching moment and the average dynamic pressure and downwash at the stabilizer. The method is found to yield predictions that are adequate for the primary design phase within aircraft design [38]. Bouquet has implemented the method by Obert with minor implementations for the purpose of integration into a conceptual aircraft design framework. Efforts are made to reduce the amount of assumptions used. Assumptions for a non-changing slipstream tube shape and diffusion into the surrounding flow remain, leading to some incorrect results [13].

A first step in improving modeling fidelity from empirical calculations is achieved with Lifting Line (LL) and VLMs. LL models used to represent a wing consisting of a superposition of horseshoe vortex elements along the span at one chordwise location of the wing, yield good lift predictions for high Aspect Ratio (AR) finite wings. Lower AR finite wings and their lift can be modeled more accurately using VLMs, with the horseshoe elements also placed chordwise along the wing, resulting in a finite wing represented as a lifting surface by a lattice of horseshoe vortex elements. Each vortex element has an unknown circulation strength that can be determined by imposing the boundary condition of the flow being parallel at each vortex elements, i.e. the normal component of the flow of every horseshoe vortex is equal to zero. The lift of the lifting surfaces is determined using the obtained circulation and the Kutta-Joukowski theorum. VLM models are based on incompressible, irrotational, inviscid flow, making the Laplace equation the main equation to describe the

flow. Irrotational flows are also referred to as potential flows. Classical VLM methods simplify the wing geometry by ignore thickness of the wing, placing the lifting surface in a single plane and imposing the boundary conditions in this plane [7, 22]. Increasing the fidelity of a VLM can involve the addition of the compressibility correction or a combination with a slipstream tube model in order to predict the effect of slipstream effects on the wing.

Predictions for the lift distribution made using VLM-slipstream tube model have revealed overprediction of the wing lift as a results of the slipstream swirl or tangential velocity component [54, 4, 16]. Veldhuis noticed that accounting for only 50% of the propeller swirl matches experimental results for the wing lift distribution [54]. This factor of 0.5 is referred to as the Swirl Recovery Factor (SRF), a non-physical correction to the propeller swirl to match experimental data. Alba attempted to find a SRF by integrating the kinetic rotational energy in the disks of the propeller slipstream tube. The square root of the averaged kinetic rotation energy fraction from the propeller hub and the wing TE is taken to be the SRF [4]. Epema also applies a SRF to the propeller tangential velocities in order to match experimental data [16]. The problem with the SRF is that it is not based on real flow phenomena and is merely a multiplication factor to more closely match experimental data.

Prediction for wing lift for a wing encountering a constant velocity jet without a swirl component also result in an over estimations in VLM methods [24, 19]. Rethorst identified that accounting for the extra downwash created by the jet boundary is important for the problem of a wing in a jet. A correction for wing in circular jet based on the jet boundary is derived by Rethorst. The implemention of this Rethorst correction in VLM models has proven to closely match experimental results [42, 41]. Nederlof corrected for the finite height of a propeller slipstream in a LL model using a method that is entirely based on the Rethorst correction, which resulted in close predictions to CFD [35]. A weakness of the correction by Rethorst are the idealizations on which the correction derivation is based. Rethorst warns for the application of the correction in design outside of the considered idealizations of the correction derivation [41].

Panel methods are an extension of VLM methods, which allow for the consideration of more complex geometries, but are based on the same principles as VLM methods. The vortex elements and boundary conditions are imposed on the actual body surfaces of an aircraft wing rather than a flat surface and thus include geometry volume and thickness. Just like VLM methods, panel methods consider potential flow. Panel methods can be further expanded to increase their fidelity. A compressibility correction can be included to allow panel methods to be used at higher mach numbers. The panel singularity distributions on the panel elements can no longer be limited to being constant and the panels themselves can also not be limited to being planar. Resulting in so-called advanced panel methods [29, 22]. Despite the increased fidelity in geometry modeling, panels methods can be unreliable when it comes to predicting lift and LSS characteristics, even without the incorporation of propulsion effects. Lednicer investigated various aircraft configurations using the commercial panel method solver VSAERO. Different paneling configurations for the same aircraft geometry can result in completely different aircraft lift and stability predictions [25, 26].

CFD methods are one of the highest fidelity methods available in the field of aircraft design and aerospace in general. CFD considers virtually no simplifications in geometry and is capable of handling the full nonlinear Navier-Stokes equations that deal with the continuity, momentum and energy of a flow. CFD is thus not limited to including viscous effects. The geometry is also not limited to incorporating propulsors and investigating propulsion effects [6, 7]. Propeller propulsion effects have also been studied extensively using CFD. An example being research done on WingTip Mounted Propellers (WTMPs) using CFD [20]. The methods of CFD involve dividing the flow field around a particular geometry in a discrete number of grid points, also known as the mesh. The flow field parameters velocity, temperature, density and pressure are evaluated at these grid points using the Navier-Stokes equations. CFD can therefore determine the flow in the whole discretized flow field and is not limited to only determining the flow properties on the surface of the geometry like for VLM and panel methods. CFD is therefore specifically useful to study complex flow fields on and away from the geometry surface. The main disadvantage of CFD therefore is the long computational time necessary to solve for the flow properties in all grid points. This computational time quickly increases as a function of the amount of discrete points in the mesh. The validity of the results of CFD methods is also dependent on the quality of the specified mesh. [6, 7].

The aircraft design process is what ultimately determines the aircraft configuration and the degree to which the propeller slipstream interacts with the other aircraft components. The aircraft design process itself is composed of three phases: the conceptual, preliminary and detailed design phases. The conceptual design phase aims to set the fundamental aspects of an aircraft design, think of wing shape and location, horizontal

stabilizer location and configuration of the propulsion system. The main question during this design phase is if the design can meet the design requirements. The preliminary design phase deals with only minor changes to the aircraft configuration and lay-out and ends with a go/no go decision to continue with the design and commit to the manufacturing of it. The aerodynamic performance of the design is determined during this preliminary phase. If it it decided to manufacture the aircraft, the detailed design phase is entered where exact location of nuts and bolts and the shape of all structural elements is determined [5].

During the conceptual and preliminary design phase, the design geometry and propulsion system arrangement is still subjected to change. The aircraft design is optimized by means of design iterations. The aircraft design of each iteration needs to be evaluated in a timely manner to determine the degree to which it meets the design requirements. This in turn, determines what changes are made to the aircraft design in the next design iteration [5]. One of those design requirement being LSS [2]. This is where the modeling of slipstream effects on the stabilizer and LSS comes into play for the field aircraft design.

VLM methods are well suited for obtaining LSS predictions by predicting lift at the horizontal stabilizer and doing so in a quick manner. However, literature has pointed out problems in terms of the overestimation of lift due to the presence of the propeller slipstream. Corrections exist for VLM methods to counter this overestimation of lift. The Rethorst correction from literature has proven to yield accurately lift prediction for wings encountering a circular jet for VLM methods, provided that the assumptions for the derivation of the correction hold. The Rethorst correction therefore has potential to improve VLM lift predictions of a stabilizer encountering a propeller slipstream and improve VLM LSS predictions with the involvement of slipstream effects.

This thesis investigates the application of the Rethorst correction to a horizontal stabilizer that encounters a propeller slipstream. For the Rethorst correction to be applicable to the horizontal stabilizer, two conditions need to be met. The first one being the application of the assumptions of the Rethorst correction at the stabilizer. The assumptions of the Rethorst correction at the stabilizer are only valid for a specific range of situations. The Rethorst correction assumptions at the stabilizer thus define the scope of the thesis. Secondly, applying the Rethorst correction at the stabilizer that encounters a propeller slipstream, should result in an accurate prediction of its lift. The lift at the horizontal stabilizer is mainly dependant on the downwash and dynamic pressure experienced by the horizontal stabilizer. This aspect leads to the main and sub research questions of this project.

Scope

For the Rethorst correction for a wing in a jet, the following assumptions have to apply [42, 41]:

1. The jet extends symmetrically through the wing,
   i.e. the same amount of the jet thus passes above and below the wing.
2. The jet center line is located in the middle of the wing,
   i.e. the same wing length extends to the left and right of the jet center line
3. The velocity distribution in the jet is constant.
4. The jet is circular.
5. The flow is incompressible, ideal and inviscid.

Each assumption is now individually analyzed to evaluate if the assumption holds at the horizontal stabilizer.

Within the VLM methods to which the Rethorst correction is applied, assumption 5 automatically applies by definition.

Assumption 4 requires the propeller slipstream to be circular when reaching the horizontal stabilizer. The propeller slipstream is known to deform because of interacting with the wing in the form of shearing, contract as a result of increased slipstream velocity in combination with continuity and diffuse as a function of distance [50]. However, wind tunnel experiments by Katzoff have pointed out that the slipstream diameter at the horizontal stabilizer is almost the same as the propeller diameter for various aircraft configurations [23]. Assumption 4 is therefore said to be applicable to the horizontal stabilizer.

The velocity inside a propeller slipstream is not constant, making assumption 3 not applicable for the wing nor the horizontal stabilizer in the case of the basic Rethorst correction. However, an extension to the Rethorst correction by Prabhu enables the correction to be determined for an arbitrary smooth velocity distribution inside the jet. The velocity distribution in the slipstream is discretized in elements of constant velocity, for each of which the Rethorst is determined and summed to obtain the complete correction [40]. This combination of Rethorst correction and the extension by Prabhu is referred to as the *jet correction* in this thesis. With the jet correction, assumption 3 can be adhered to for both the wing and horizontal stabilizer.

In reality, assumption 2 is far from realistic. Conventional aircraft designs never feature propellers mounted exactly in the middle of the wing. However, a sensitivity analysis by Nederlof has pointed out that the magnitude of the Rethorst correction quickly goes to zero when moving away from the jet boundary [35], indicating that the Rethorst correction can also be determined accurately when the jet is not located in the middle of the wing. Willemsen and van der Leer have made use of this fact in the modeling of their wing-propeller systems, which includes the jet correction to correct the lift inside the confines of the propeller boundary [56, 27].

Lastly, the first assumption is hardly realistic for the wing and stabilizer for many reasons. Firstly, conventional aircraft hardly feature propeller positioning with the propeller center line at the same height as the main wing. Secondly, the propeller slipstream vertical position changes with distance due to the interaction with the wing. The wing upwash in front of the wing moves up the propeller slipstream, while it is moved down in the trailing downwash flow field behind the wing. Willemsen also encountered this issue with the jet correction. Willemsen assumes that the jet correction is not substantially influenced in the case of low ratios of vertical distances between the wing and slipstream center line relative to propeller radius [56]. This assumption does not imply that the slipstream center line can now be located far away from the the horizontal stabilizer plane. The jet correction will still be the most accurate when the slipstream center line and horizontal stabilizer are not far apart. Because of the nature of the slipstream deflection, the slipstream center line will hardly be aligned with the horizontal stabilizer. To add to the problem, the slipstream deflection is a function of AoA because of its dependence on wing lift. The slipstream vertical location at the horizontal stabilizer therefore also differs with AoA. Making the problem of the vertical distance between the propeller center line and stabilizer even larger.

In an effort to minimize the distance between the slipstream center line and the horizontal stabilizer plane, the scope of considered aircraft configurations to which the jet correction can be applied at the horizontal stabilizer is restricted to:

- Conventional high wing, low horizontal stabilizer configuration:
  The horizontal stabilizer needs to be mounted as close a possible to the propeller center line to make assumption 1 somewhat applicable. Since the aircraft propellers are mounted on the wing for conventional configuration aircraft, the wing and stabilizer vertical positions are required to be as closely together as possible. Meaning that a high wing and low mounted horizontal stabilizers is most ideal. No T-tail or mid-tail stabilizer configurations and no mid or low wing configurations are considered for this thesis.
- Tractor IB propeller configuration:
  Furthermore, in light of assumption 2, the considered aircraft configuration needs to feature two tractor propellers mounted close to the mid span position of the wing. Only in this situation will the slipstream spanwise position line up with the horizontal stabilizer. Without the constraint of IB mounted propellers, the propeller slipstream would hardly interact with the horizontal stabilizer in the first place.
- Cruise condition and configuration:
  In addition, only the cruise condition of aircraft is considered. Characterized by low AoA and high flight speed, the propeller slipstream should encounter a low amount of deflection, because of the low cruise lift coefficient and thus experience a low downwash. The aircraft configuration is also limited to cruise condition, this means no deployment of high lift devices. The deployment of flaps for example, in the flight phases other than cruise, will increase the wing lift, increase the downwash behind the wing and deflect the propeller slipstream away from the horizontal stabilizer.

Despite the narrowing of the scope to limit the vertical distance between the stabilizer and the slipstream center line, an effort needs to be made to quantify this vertical distance to draw a conclusion on the validity of the Rethorst correction assumptions applying at the stabilizer.

Research Questions and Purpose Statement

The following main research question of this thesis project is to investigate:

> *How applicable is the Rethorst correction to the horizontal stabilizer of a conventional high wing, lower mounted stabilizer, IB propeller configuration aircraft?*

The purpose of the research question is to evaluate the prediction of the stabilizer's lift and thus its LSS contribution. To investigate the stabilizer lift and check the validity of the application of the jet correction at the stabilizer, the following sub-questions are identified:

- *What is the average downwash at the horizontal stabilizer with the application of the jet correction?*
- *What is the average dynamic pressure at the horizontal stabilizer with the application of the jet correction?*
- *What is the vertical distance between the slipstream center line and the horizontal stabilizer?*

The plan to tackle the research questions for this thesis is to perform a case study on a reference aircraft using a VLM code that contains an implementation for the jet correction. For this reason, the code by Willemsen and van der Leer is inherited for this thesis project. This code contains the ability to model a wing-propeller system as a lifting surface and higher fidelity slipstream tube model combination, where the contraction and deflection of the slipstream tube can be evaluated [56, 27]. Modifications to this code are required to model the horizontal stabilizer and apply the jet correction. The reference aircraft that is chosen and fits in the scope of this project is the Fokker F-27. A conventional high wing, low stabilizer and dual tractor IB propeller configuration aircraft. At the end of the case study, the assumption of the vertical distance between the propeller center line and the horizontal stabilizer as a result of the slipstream deflection is quantified to verify if the application involving assumption 1 of the Rethorst correction is valid.

The purpose of this thesis project can be summarized to be to:

> *Investigate the applicability of the Rethorst correction at the horizontal stabilizer for the Fokker F-27, by evaluating the average downwash and dynamic pressure at the horizontal stabilizer using a VLM to model the aircraft airframe, a BEM to model the propeller and a potential flow slipstream model for the slipstream induced velocities and a comparison to wind tunnel and flight test data.*

Simplifications

To make the problem of the case study more manageable and reduce its complexity, simplifications for the Fokker F-27 model and the moment coefficient are considered.

Aircraft Model

The following simplifications are considered in this thesis project for the model of the F-27, while still keeping enough model fidelity to answer the research questions:

- No wing and stabilizer dihedral:
  The F-27 has a 2.5° dihedral on the OB span side of the wing starting at the propeller center line. The IB wing section between the propeller section and the wing mid point does not feature any dihedral [53]. This 2.5° dihedral on the OB wing can be neglected, since it not positioned in front of the horizontal stabilizer and therefore does not influence the downwash experienced by the stabilizer.
  The horizontal stabilizer itself features a 6° dihedral angle [53]. The main consequence of neglecting the dihedral is the fact that the horizontal stabilizer position of the section other than the root changes with respect to the propeller slipstream. In fact, ignoring the dihedral will bring the stabilizer close to the propeller center line, which is good for the applicability of the jet correction. However, the simplification changes the geometry of the F-27 model with respect to the real life aircraft.
- No fuselage and propeller nacelles:
  The fuselage and nacelle bodies affect the aircraft moment coefficient in three ways. Firstly, they themselves create a moment that contributes to the total moment of the aircraft. Secondly, by affecting the lift on the wing and horizontal stabilizer due to their presence. Thirdly, they change the aircraft aerodynamic center (a.c.). The first two effects are discussed respectively.
  Modeling the fuselage and nacelles to take into account their moment contributions can be done in various ways. The fuselage and nacelle shape can be represented by means of VLM panels. However, literature has indicated that this method can be unreliable [25, 26]. Another option is to represent the fuselage and nacelles moment contribution by means of the slender body theory. This would enable the determination of a moment contribution of the fuselage and nacelles. However, the fuselage width to length ratio of the F-27 does not fit the requirement of being much less than 1 for slender body theory [22]. Instead, it is chosen to account for the fuselage and nacelle moment contributions using a correction that is already available for the F-27 specifically [53]. This correction is described in more detail in the F-27 case study.
  The fuselage and the propeller nacelles interact with the main wing and stabilizer and affect their lift and their contributions to the moment of the aircraft. The wing lift distribution is altered due to the

presence of the fuselage and nacelles, often resulting in a decrease in lift close to the fuselage and nacelle positions. This interaction is often referred to as the *carry-over effect* of the fuselage and nacelles on the wing. The carry-over effect also results in a different lift coefficient, lift slope compared to the isolated wing. This effect on the wing lift slope however is quite small [44, 32, 21]. The carry-over effect therefore barely affects the LSS, as it is a function of the lift slope, and is therefore not taken into account during the F-27 case study.

- Linear wing twist distribution:
  The twist on the real life F-27 is only applied to the OB wing section beyond the propeller center line position, with the IB wing section section thus not having any twist. The wing twist in the F-27 model in this thesis is applied as a linear change from the root to the tip. A consequence being that the twist impacts the lift of the IB wing section and thus its generated downwash, which is investigated in the verification stage of this thesis.
- No vertical stabilizer:
  In symmetric flight, the vertical stabilizer only contributes to the longitudinal moment of the aircraft by means of its drag created by viscous flow phenomena. The vertical stabilizer does not generate lift during symmetric flight (when it is symmetrically positioned), meaning no generation of induced drag. However, classical VLM methods cannot model the viscous drag component without addition implemented features. Also, the moment contribution due to the vertical tail viscous drag is very small since the magnitude of the viscous drag is small. The viscous drag component contribution can therefore be neglected in the total moment coefficient. In fact, in this case there is no use for the vertical stabilizer to be modeled to begin with. The vertical stabilizer is therefore not included in the F-27 model for this thesis project.

Moment coefficient

The moment of an aircraft is always determined around a so-called moment reference point. The moment around this reference point is equal to the sum of all aircraft forces multiplied with their moment arm relative to the reference point. This includes the lift and drag forces. The calculated moment is unique to the chosen reference point.

The lift force in known to be much larger compared to the drag force during cruise, a factor of 17 larger is not uncommon [51]. In addition, the drag force contribution to the aircraft moment becomes even smaller compared to the lift contribution for cases where the vertical reference point position is close to the application point of the aircraft aerodynamic forces. This applies for the F-27 [53]. The drag force contributions to the aircraft moment are thus neglected in this thesis. The effect of neglecting the drag force contribution to the moment is discussed in the verification part of this thesis.

Thesis Outline

The inherited code by Willemsen and van der Leer used for this thesis project is described in Chapter 2. The implementation required to make it useful for this thesis project are also discussed. In Chapter 3, the inherited code verification and validation is covered. In addition, a sensitivity analysis is performed to investigate the effect of the added implementations. The research questions are tackled in the Fokker F-27 case study in Chapter 4. The conclusions to the research questions and recommendations are discussed in Chapter 5 and 6 respectively. Appendix A and Appendix B contains the geometrical data of the Fokker F-27 aircraft models and the propeller model used in this thesis. Appendix C covers implementations and results of the inherited code that became obsolete for this thesis project that might be useful for future use and or reference. Lastly, a derivation for the LSS of the F-27 is presented in Appendix D.

2

The Aircraft Longitudinal Interaction and Moment Evaluator

This chapter focuses on the Python based tool that is used during this thesis project. Nederlof first used the the tool for his thesis project to investigate the effect of finite slipstream height to improve the modeling of wing-propeller interaction, using a correction derived by Rethorst [35]. The tool is passed down to other students for their master thesis projects. Willemsen performed a sensitivity analysis on WTMP-wing systems [56]. Van der Leer used the tool in combination with an aircraft structures module to investigate the effect of WTMPs on the structural weight and overall weight of an aircraft [27]. In this thesis, the tool is used to evaluate the moment coefficient of a wing-horizontal stabilizer-propeller slipstream system. Implementations are required to meet this goal. In section 2.1 a description of the most relevant elements of the tool for this thesis project is given. The new implementations necessary to evaluate the aircraft moment are discussed in section 2.2.

2.1. Description

A complete description of the tool and its features is given by Willemsen and van der Leer [56, 27]. This section described components of this tool that are relevant to this thesis. Some more detail is provided on modules to create a more complete picture of the described tool, which is necessary for some of the discussion later in the report.

The tool works by iterating between a VLM module to determine the lifting surface properties and a BEM module that determines the propeller performance and the slipstream properties. The wing and propeller slipstream interact with each other. The wing induces an induced velocity on the propeller slipstream and vise versa. This interaction of slipstream on wing creates changes in the wing lift and drag. The induced velocities of the wing create a non-uniform inflow to the propeller, resulting in changes to the propeller thrust and torque and deforms the propeller slipstream. Iterations between the VLM and BEM modules are performed until the change per iteration in C_L, C_D, C_T and C_Q is smaller than the thresholds of $1e{-}3$, $1e{-}4$, $1e{-}3$ and $1e{-}3$ respectively. The system is said to be converged [56].

The VLM module consists of a VLM formulation and a jet correction, which are described in subsection 2.1.1 and 2.1.2 respectively. The BEM module consists of a BEM to calculate the isolated propeller performance map, a non-uniform inflow propeller analysis and a slipstream model. The non-uniform inflow analysis of the propeller is described in subsection 2.1.3. The slipstream model is covered in subsection 2.1.4. The computation of the total aerodynamic forces is discussed in subsection 2.1.5.

2.1.1. VLM Formulation

The VLM is modified from an exciting VLM formulation in Python[1]. It is a VLM formulation that is able to take induced velocities in x and z (V_{x_i} and V_{z_i}) into account in its computations. Allowing it to take into account induced velocities resulting from the presence of other aircraft components, such as a propeller slipstream. The wing is modeled in the $z = 0$ plane, this greatly simplified the calculation, but also introduces a slight error

[1] PyVLM, AeroPython Team, https://github.com/aqreed/PyVLM [Accessed 13/6/2023]

in the induced velocities at high AoA when using cambered airfoils [30]. The camber of the wing is taken into account with the normal velocities. The wing wake is shed in the $z = 0$ plane, leading to a non-force free wake [22].

The circulation vector $\mathbf{\Gamma}_w$ of an isolated wing is determined using the system of the general form described by Equation 2.1.

$$\mathbf{C}_{ww}\mathbf{\Gamma}_w = \mathbf{V}_{n_w} \tag{2.1}$$

Where $\mathbf{C}_{ww}$ are the AICs of the wing-on-wing panel induced velocities calculated using the Biot-Savart law and $\mathbf{V}_{n_w}$ are the normal flow velocities of each panel on the wing [22]. The normal velocities of the VLM panels are given by Equation 2.2. The normal velocities take the camber line slope of the airfoil camber $g(x, z)$ into account, as well as the induced velocities V_{ind_x} and V_{ind_z} [56].

$$\mathbf{V}_{n_w} = V_\infty \left(\frac{\partial g}{\partial x} - \alpha \right) + V_{ind_x} \frac{\partial g}{\partial x} - V_{ind_z} \tag{2.2}$$

AIC Calculation

To determine the AIC matrix, the vertical downwash induced by every horseshoe vortex needs to be calculated in every panel CP. Each horseshoe vortex consists of three elements that each contribute to the downwash induced by the complete horseshoe vortex. First, a bounded vortex filament between the points e and f, that forms the LE of the horseshoe vortex, induces a downwash at an artibrary point P according to Equation 2.3 [22], where $\mathbf{r}_1$ is the distance between P and the first end of the bounded vortex filament and $\mathbf{r}_2$ is the distance between P and the second end of the bounded vortex filament. Lastly, $\mathbf{r}_0$ is the distance between both end of the vortex filament. The bounded vortex filaments are modeled with a viscous core, meaning that the downwash is set to zero when the distance to the bounded vortex filament becomes smaller than a threshold distance of $1e-12m$.

$$\mathbf{V}_{ind}(x, y, z) = \frac{\Gamma}{4\pi} \frac{\mathbf{r}_1 \times \mathbf{r}_2}{|\mathbf{r}_1 \times \mathbf{r}_2|^2} \mathbf{r}_0 \left(\frac{\mathbf{r}_1}{|\mathbf{r}|_1} - \frac{\mathbf{r}_2}{|\mathbf{r}|_2} \right) \tag{2.3}$$

The second and third component of the horseshoe vortex are semi-infinite vortex filaments, referred to as the trailing horseshoe vortex elements, that extend from e and f to $+\infty$ respectively. Each trailing vortex filament induces a downwash at P according to Equation 2.4 [7], where $\mathbf{r}$ is the minimum distance from the semi-infinite vortex filament and point P.

$$V_{ind}(x, y, z) = \frac{\Gamma}{4\pi \mathbf{r}} \tag{2.4}$$

Willemsen and van der Leer's version of the VLM formulation calculates the total induced velocity in P for a horse vortex as the sum of the downwash by the bounded vortex element and the two trailing vortex filaments in the $z = 0$ plane alone. The two trailing vortex filaments extend to $+\infty$, meaning that the total downwash is equal to the sum of Equation 2.3 with two contributions of Equation 2.4, one of the latter having an opposite sign. In this report, determining the AICs in this manner is referred to as the *farfield* method, since the trailing vortices extend into the farfield of $+\infty$.

2.1.2. Jet Correction

The presence of the propeller slipstream affects the lift experienced by the wing. It turns out that accounting for the slipstream height is important when it comes to modeling the lift of a wing engulfed in a circular jet [35]. Rethorst developed a method to calculate the downwash due to the presence of a circular jet boundary for a wing symmetrically extending through the jet [42, 41]. Prabhu extended the method by Rethorst by removing one of its main limitations, being the constant jet velocity distribution. It is the combination of the method by Prabhu and Rethorst that is called the *jet correction*, which is used to correct the AIC matrix of the wing by means of the jet correction matrix $\mathbf{G}$ as shown by Equation 2.5. Effectively correcting the circulation strength of the wing panels to account for the finite propeller slipstream height.

$$(\mathbf{C}_{ww} + \mathbf{G}_w)\mathbf{\Gamma}_w = \mathbf{V}_{n_w} \tag{2.5}$$

Propellers can be located at a z-position which is different from the wing. As a simplification, the jet correction is determined as if the propeller center line and wing vertical location are both positioned in the same z-plane: $z_p = z_w$ [56]. The Rethorst correction and the extension by Prabhu to account for a non-uniform jet velocity distribution are now discussed respectively.

Rethorst Correction

The downwash as a result of the jet boundary is derived by Rethorst under the condition where the wing symmetrically extends through a circular jet with a constant jet velocity V_j profile. The derivation is performed for a circular jet and a wing with their symmetry axes located along the same line. For the derivation, a potential flow assumption is used, with the fluid being ideal, incompressible and inviscid.

Consider a single horseshoe vortex located either inside or outside the jet. The derivation by Rethorst is based on splitting this system up into an even and odd part, where the sum of both the even and odd systems results in the original system, see Equation 2.6. For both the even and the odd system, the downwash induced by the jet boundary is derived for a horseshoe vortex located inside and outside the jet.

$$\mathbf{G} = \mathbf{G}_{even} + \mathbf{G}_{odd} \tag{2.6}$$

The even part of the correction $\mathbf{G}_{even}$ is purely a function of the left, right corner positions (e and f respectively) and the CP y-positions of the horseshoe vortices ζ, which are normalized with the propeller radius R_p. Equation 2.7 describes the result of the derivation for the even part $\mathbf{G}_{even}$ by Rethorst, where the first subscript index represents a horseshoe vortex CP position and the second index presents the original position of the imaged horseshoe vortex. The index can either be j, meaning inside the jet ($-1 < \zeta < 1$). Or o, meaning outside the jet ($|\zeta| > 1$). When inspecting Equation 2.7, it can be noted that: $\mathbf{G}_{jo_{even}} = \mathbf{G}_{oj_{even}}$ and $\mathbf{G}_{oo_{even}} = -\mathbf{G}_{jj_{even}}$.

$$\begin{aligned}
\mathbf{G}_{jj_{even}}(\zeta) &= \frac{1}{R_p}\frac{1-\mu^2}{1+\mu^2}\left[\frac{1}{(1/f)-\zeta} - \frac{1}{(1/c)-\zeta} + \frac{1}{(1/d)+\zeta} - \frac{1}{(1/c)+\zeta}\right] \\
\mathbf{G}_{oj_{even}}(\zeta) &= -\frac{1}{R_p}\frac{(1-\mu)^2}{1+\mu^2}\left[\frac{1}{\zeta-e} - \frac{1}{\zeta-f} + \frac{1}{\zeta+f} - \frac{1}{\zeta+e}\right] \\
\mathbf{G}_{jo_{even}}(\zeta) &= -\frac{1}{R_p}\frac{(1-\mu)^2}{1+\mu^2}\left[\frac{1}{\zeta-e} - \frac{1}{\zeta-f} + \frac{1}{\zeta+f} - \frac{1}{\zeta+e}\right] \\
\mathbf{G}_{oo_{even}}(\zeta) &= -\frac{1}{R_p}\frac{1-\mu^2}{1+\mu^2}\left[\frac{1}{(1/f)-\zeta} - \frac{1}{(1/c)-\zeta} + \frac{1}{(1/d)+\zeta} - \frac{1}{(1/c)+\zeta}\right] \\
\mathbf{G}_{even}(\zeta) &= \begin{bmatrix} \mathbf{G}_{jj_{even}} & \mathbf{G}_{jo_{even}} \\ \mathbf{G}_{oj_{even}} & \mathbf{G}_{oo_{even}} \end{bmatrix}
\end{aligned} \tag{2.7}$$

The odd part of the correction $\mathbf{G}_{odd}$ follows from determining the perturbation velocities created by the horseshoe vortex and the jet boundary by means of the boundary conditions of the jet boundary. This derivation leads to the introduction of the modified Bessel functions of the first and second kind I, K and their derivatives I' and K'. The complete derivation of the off part is covered by Rethorst. The final form of the odd part is displayed by Equation 2.8 [41, 42].

$$\begin{aligned}
\mathbf{G}_{jj_{odd}}(\xi,\zeta) &= \frac{8}{R_p\pi\zeta}\sum_{p=0}^{\infty}(2p+1)^2\int_0^{\infty}\frac{KK'I(\zeta\lambda)\sin(\xi\lambda)d\lambda}{\left[1/\{(1/\mu^2)-1\}\right]-\lambda IK'}\int_{e\lambda}^{f\lambda}\frac{I(\lambda\beta)}{(\lambda\beta)}d(\lambda\beta) \\
\mathbf{G}_{oj_{odd}}(\xi,\zeta) &= \frac{8}{R_p\pi\zeta}\sum_{p=0}^{\infty}(2p+1)^2\int_0^{\infty}\left[\frac{1}{\mu-\lambda\{(1/\mu)-\mu\}IK'}-1\right]\frac{K(\zeta I)\sin(\xi\lambda)d\lambda}{\lambda}\int_{e\lambda}^{f\lambda}\frac{I(\lambda\beta)}{d}(\lambda\beta) \\
\mathbf{G}_{jo_{odd}}(\xi,\zeta) &= \frac{8}{R_p\pi\zeta}\sum_{p=0}^{\infty}(2p+1)^2\int_0^{\infty}\left[\frac{1}{\mu-\lambda\{(1/\mu)-\mu\}IK'}-1\right]\frac{I(\zeta I)\sin(\xi\lambda)d\lambda}{\lambda}\int_{e\lambda}^{f\lambda}\frac{K(\lambda\beta)}{d}(\lambda\beta) \\
\mathbf{G}_{oo_{odd}}(\xi,\zeta) &= \frac{8}{R_p\pi\zeta}\sum_{p=0}^{\infty}(2p+1)^2\int_0^{\infty}\frac{II'K(\zeta\lambda)\sin(\xi\lambda)d\lambda}{\left[1/\{(1/\mu^2)-1\}\right]-\lambda IK'}\int_{e\lambda}^{f\lambda}\frac{K(\lambda\beta)}{(\lambda\beta)}d(\lambda\beta) \\
\mathbf{G}_{odd}(\xi,\zeta) &= \begin{bmatrix} \mathbf{G}_{jj_{odd}} & \mathbf{G}_{jo_{odd}} \\ \mathbf{G}_{oj_{odd}} & \mathbf{G}_{oo_{odd}} \end{bmatrix}
\end{aligned} \tag{2.8}$$

Non-Uniform Jet Velocity

The correction derived by Rethorst is limited to jets with a constant jet velocity. In reality, a propeller slipstream will have a non-uniform velocity distribution. To apply the Rethorst correction is these circumstances, Prabhu proposes to discretize a smooth velocity distribution into sections of constant jet velocity. The Rethorst correction of a wing is determined for each discretized section and summed to obtain the complete jet correction $\mathbf{G}_w$ due to the propeller slipstream for the isolated wing [40], as expressed by Equation 2.9.

The discretization of the smooth slipstream velocity distribution takes place at the location of every horse-shoe vortex in the jet. So the number of discretized elements of the jet velocity distribution, indicated with the subscript i, is equal to the amount of spanwise panels in the jet m_j, as shown in Figure 2.1. As is explained in detail later in this chapter, the jet correction is only calculated on one side of the jet due to symmetry. The obtained jet correction is copied to the other side of the jet to obtain the correction at every discretized section.

$$\mathbf{G}_w = \sum_{i=1}^{m_j} \mathbf{G_i} \tag{2.9}$$

The wing paneling also consists of chordwise panels, while the jet correction is determined as if there is only one row of chordwise panels. The elements of $\mathbf{G}_w$ that belong to a specific panel at location y are copied to all the chordwise panels at that location y.

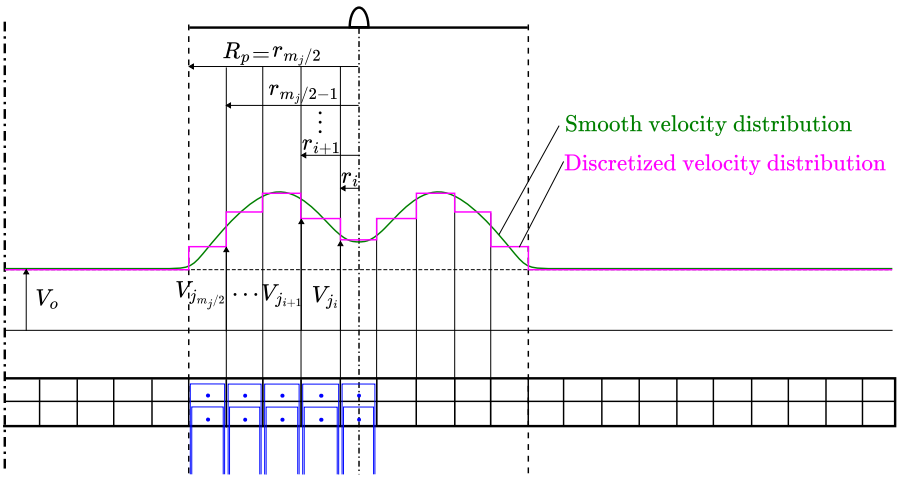

Figure 2.1: A schematic of the velocity discretization as defined for the Rethorst correction adaption by Prabhu [40] for an arbitrary smooth velocity distribution.

2.1.3. Non-Uniform Propeller Inflow Analysis

The performance of a propeller change when a propeller disk experiences a non-uniform inflow velocity profile. An example situation being a non-zero AoA inflow at the propeller disk [59]. To capture this change in propeller performance, the method by van Arnhem [8] is implemented in the BEM formulation. This method adapts the propeller performance as a result of velocity disturbance that result in a local change in advance ratio ΔJ in the propeller load distribution, which is descretized as shown by Figure 2.2 [9]. The non-uniform inflow analysis is given by a quasi-steady model, where a correction can be added to account for unsteady effects. Both the quasi-steady and unsteady models are individually discussed.

Quasi-Steady Model

The effective advance ratio J_{eff} as a result of a ΔJ is the axial (subscript a) and tangential (subscript t) direction is determined with Equation 2.10.

$$\begin{aligned} J_{eff_a} &= \Delta J_a + J = \frac{\Delta V_a(r,\phi)}{nD_p} + \frac{V_\infty}{nD_p} \\ J_{eff_t} &= \Delta J_t + J = \frac{V_\infty}{[n + (\Delta V_t / 2\pi r)]\, D_p} - \frac{V_\infty}{nD_p} \\ \Delta V_t &= -\Delta V_y \cos(\phi) - \Delta V_z \sin(\phi) \end{aligned} \tag{2.10}$$

From the known propeller performance map resulting from the BEM analysis, the change in thrust and torque distribution $T^{'}$ and $Q^{'}$, is obtained at the location J_{eff}, as is expressed by Equation 2.11and 2.12 respectively.

$$\begin{aligned} \Delta T_a^{'}(r,\phi) &= \left[C_T^{'}(J_{eff_a}) \frac{\rho}{\rho_\infty} - C_T^{'}(J_\infty) \right] \rho_\infty n^2 D_p^4 \\ \Delta T_t^{'}(r,\phi) &= \left[C^{'} C_T(J_{eff_a}) \left(n + \frac{\Delta V_t}{2\pi r} \right)^2 \frac{\rho}{\rho_\infty} - C_T^{'}(J_\infty) \right] \rho_\infty D_p^4 \end{aligned} \tag{2.11}$$

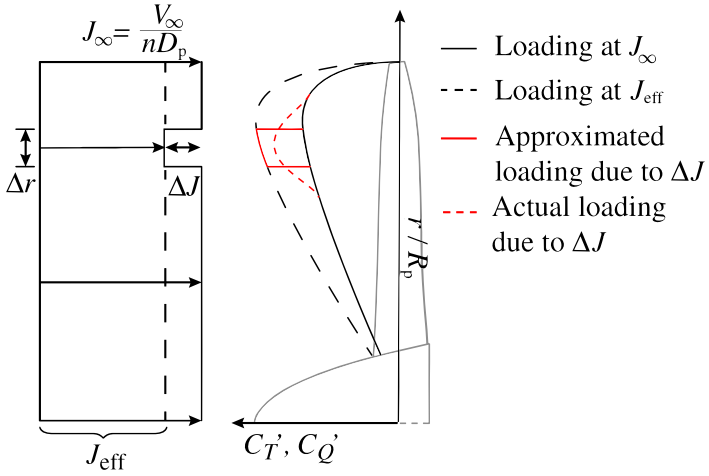

Figure 2.2: A schematic of the propeller load discretization used in the non-uniform inflow analysis method by van Arnhem [8].

$$\begin{aligned}\Delta Q_a'(r,\phi) &= \left[C_Q'(J_{eff_a})\frac{\rho}{\rho_\infty} - C_Q'(J_\infty)\right]\rho_\infty n^2 D_p^5 \\ \Delta Q_t'(r,\phi) &= \left[C_Q'(J_{eff_a})\left(n+\frac{\Delta V_t}{2\pi r}\right)^2\frac{\rho}{\rho_\infty} - C_Q'(J_\infty)\right]\rho_\infty D_p^5\end{aligned} \tag{2.12}$$

The total change in thrust and torque load distribution due to ΔJ, C_T' and C_Q', is the sum of the axial and tangential component, summarized with Equation 2.13.

$$\begin{aligned}\Delta C_T'(r,\phi) &= \frac{\Delta T_a' + \Delta T_t'}{\rho_\infty n^2 D_p^4} \\ \Delta C_Q'(r,\phi) &= \frac{\Delta Q_a' + \Delta Q_t'}{\rho_\infty n^2 D_p^5}\end{aligned} \tag{2.13}$$

The new propeller thrust force, normal and side force contributions are obtained by integrating the newly obtained propeller load distributions over the propeller radius and azimuth angle ϕ as shown by Equation 2.14.

$$\begin{aligned}\Delta C_T &= \frac{1}{2\pi}\int_0^{2\pi}\int_{R_{hub}}^{R_p}\Delta C_T'(r,\phi)\,dr\,d\phi \\ \Delta C_Q &= \frac{1}{2\pi}\int_0^{2\pi}\int_{R_{hub}}^{R_p}\Delta C_Q'(r,\phi)\,dr\,d\phi \\ \Delta C_N &= -\frac{1}{2\pi}\int_0^{2\pi}\int_{R_{hub}}^{R_p}\frac{\Delta C_Q'(r,\phi)}{r}\sin(\phi)\,dr\,d\phi \\ \Delta C_Y &= -\frac{1}{2\pi}\int_0^{2\pi}\int_{R_{hub}}^{R_p}\frac{\Delta C_Q'(r,\phi)}{r}\cos(\phi)\,dr\,d\phi\end{aligned} \tag{2.14}$$

Unsteady Model

Changes to the propeller performance due to a disturbance are not instantaneous. The unsteady motion of the disturbance creates a phase angle between the disturbance itself and its effect [46]. The unsteady effects effects are taken into account by means of multiplying the Sears function $\mathbb{S}$ with the quasi-steady thrust and torque distributions, see Equation 2.15 [9]. Where σ is the reduced frequency.

$$\begin{aligned}T_{us}'(r,\sigma) &= T_{qs}'(r,\sigma)\mathbb{S}(r,\sigma) \\ \frac{Q_{us}'(r,\sigma)}{r} &= \frac{Q_{us}'(r,\sigma)}{r}\mathbb{S}(r,\sigma)\end{aligned} \tag{2.15}$$

2.1.4. Slipstream Model

The slipstream tube model is modified from the standard slipstream tube model to increase its fidelity. The slipstream tube features contraction of its radius in the x-direction, deflection of the center line as a result of the induced velocities and a circulation strength varies with azimuth in order to take into account an non-uniform inflow for the propeller [56]. The standard slipstream model, the contraction and deflection are discussed respectively.

Slipstream Tube

The slipstream tube model consists of tubes of vorticity distributions γ that are shed in the slipstream to be able to calculate the induced velocities by the presence of the slipstream at any arbitrary point in space. The slipstream tube contains circulation on the propeller disk γ_p, in the axial direction γ_a and the tangential direction γ_t. The vorticity distributions are directly derived from the circulation distribution on the propeller blade Γ_p that follows from the non-uniform inflow analysis of the propeller. The vorticity distribution is obtained from the propeller circulation distribution as described by Equation 2.16.

$$\gamma_p = \frac{B}{2\pi R_p}\Gamma_p \qquad \gamma_a = \frac{B}{2\pi R_p}\frac{d\Gamma_p}{dr} \qquad \gamma_t = \frac{nB}{V_\infty}\frac{d\Gamma_p}{dr} \tag{2.16}$$

The induced velocities follow from the vorticity distributions by multiplying the vorticity distributions with the functions f', which are directly derived from the Biot-Savart law, and integrating over each of the slipstream tube's dimensions as shown by Equation 2.17 [30, 54].

$$\begin{aligned}
V_{x_{inds}}(x,\phi,r) &= \int_{R_{hub}}^{R}\int_0^{2\pi}\int_0^{\infty}\gamma_t f'_{t,x}\,dx\,d\phi\,dr + \int_{R_{hub}}^{R}\int_0^{2\pi}\gamma_p f_{p,x}\,d\phi\,dR \\
V_{y_{inds}}(x,\phi,r) &= \int_{R_{hub}}^{R}\int_0^{2\pi}\int_0^{\infty}\left(\gamma_a f'_{a,y}+\gamma_t f'_{t,y}\right)dx\,d\phi\,dr + \int_{R_{hub}}^{R}\int_0^{2\pi}\gamma_p f_{p,x}\,d\phi\,dr \\
V_{y_{inds}}(x,\phi,r) &= \int_{R_{hub}}^{R}\int_0^{2\pi}\int_0^{\infty}\left(\gamma_a f'_{a,z}+\gamma_t f'_{t,z}\right)dx\,d\phi\,dr + \int_{R_{hub}}^{R}\int_0^{2\pi}\gamma_p f_{p,x}\,d\phi\,dr
\end{aligned} \tag{2.17}$$

All integrals are solved by means of the integral solution $\gamma\left[f\right]_x^{x+dx}$ for integrals in the form of $\int \gamma f' dx$ [56], where the functions f for the x, y and z-direction are given by Equation 2.18 to 2.21.

$$f_{t,x} = \frac{r}{4\pi}\frac{b\sin(\phi)-c\cos(\phi))(x-x_p)}{a\sqrt{(x-x_p)^2+a}} \qquad f_{p,x} = \frac{r}{4\pi}\frac{y_p\sin(\phi)+z_p\cos(\phi)}{\left(x_p^2+a\right)^{3/2}} \tag{2.18}$$

$$f_{a,y} = \frac{r}{4\pi}\frac{c(x-x_p)}{a\sqrt{(x-x_p)^2+a}} \qquad f_{t,y} = \frac{r}{4\pi}\frac{-\cos(\phi)}{a\sqrt{(x-x_p)^2+a}} \qquad f_{p,y} = -\frac{r}{4\pi}\frac{x_p\cos(\phi)}{\left(x_p^2+a\right)^{3/2}} \tag{2.19}$$

$$f_{a,z} = -\frac{r}{4\pi}\frac{b(x-x_p)}{a\sqrt{(x-x_p)^2+a}} \qquad f_{t,z} = \frac{r}{4\pi}\frac{-\cos(\phi)}{a\sqrt{(x-x_p)^2+a}} \qquad f_{p,z} = -\frac{r}{4\pi}\frac{x_p\sin(\phi)}{\left(x_p^2+a\right)^{3/2}} \tag{2.20}$$

$$a = b^2+c^2 \qquad b = r\sin(\phi)-y_p \qquad c = -r\cos(\phi)-z_p \tag{2.21}$$

Slipstream Contraction

The radius of the propeller slipstream is determined based on the law of conservation of momentum including the axial velocities inside the slipstream V_{a_s}, as given by Equation 2.22 [56].

$$\frac{r}{R_p|_{x_p=0}} = \sqrt{\frac{V_\infty + V_{a_s}|_{x_p=0}}{V_\infty + V_{a_s}}} \tag{2.22}$$

Evaluating V_{a_s} at every point in the slipstream to determine the slipstream contraction is computationally expensive. The axial velocity distribution in the slipstream is therefore approximated by means of a sum of polynomial functions of the order v as given by Equation 2.23. Where the constant C_v is found by considering the least square of an arbitrary propeller axial velocity distribution [15].

$$V_{a_s} = \sum_{v=1}^{N_v} C_v\left(1-\frac{R_p}{R_p|_{x_p=0}}\right)^v \tag{2.23}$$

Slipstream Deflection

The deflection of the slipstream is determined by the local vertical induced velocity at the center line of the slipstream tube. A local center line deflection angle is obtained by dividing the local vertical induced velocity with the free stream velocity. The local axial slipstream velocity is not taken as the denominator to prevent different radial stations of the slipstream tube to experience a different deflection and make the entire slipstream tube deflect as a whole [56]. With the small angle approximation, the vertical displacement of the slipstream becomes the local axial distance of a slipstream tube element Δx_s times the deflection angle as given by Equation 2.24.

$$\Delta z_s = \Delta x_s \frac{V_{ind_z}}{V_\infty} \tag{2.24}$$

2.1.5. Aerodynamic Forces

With the relevant parts of the VLM and BEM modules covered, now it can be explained how the aerodynamic forces are determined. The aerodynamic forces are determined for every panel individually and then summed to obtain the total aerodynamic force of the wing.

The normal and axial panel forces N and A are calculated using the Kutta-Joukowski theorem [22]. These panel forces are then used to calculate the aerodynamic forces are given by Equation 2.25. The velocity here is the total velocity. The total lift is obtained by summing the lift contribution of each panel. The total velocities are used to calculate the effective velocity V_{eff} and the effective AoA α_{eff} of every panel as given by Equation 2.26.

$$\begin{aligned} A &= -V_z \rho \Gamma \Delta y \\ N &= V_x \rho \Gamma \Delta y \\ L &= N\cos(\alpha) - A\sin(\alpha) \\ M &= N\left[x_{ref} - x_{CP}\right] - A\left[z_{ref} - z_{CP}\right] \end{aligned} \tag{2.25}$$

$$\begin{aligned} V_{eff} &= \sqrt{V_x^2 + V_y^2 + V_z^2} \\ \alpha_{eff} &= \tan^{-1}\left(\frac{V_z}{V_x}\right) \end{aligned} \tag{2.26}$$

The total velocities V_x, V_y and V_z in Equation 2.25 contain three components: the free stream velocity V_∞, the induced velocities by the slipstream V_{ind_s} and the wing panels V_{ind_w} as expressed by Equation 2.27.

$$\begin{aligned} V_x &= V_\infty \cos(\alpha) + V_{x_{ind_s}} \\ V_y &= V_{y_{ind_s}} \\ V_z &= V_\infty \sin(\alpha) + V_{z_{ind_s}} + V_{z_{ind_w}} \end{aligned} \tag{2.27}$$

2.2. Implementations

To be able to evaluate the longitudinal moment coefficient of an aircraft using the described tool, the horizontal stabilizer needs to be modeled. Implementing the horizontal stabilizer requires various other implementations. First, the horizontal stabilizer required implementation to the VLM formulation. Limitations set on the position of these additional stabilizer VLM panels are controlled using mesh matching between the main wing and stabilizer. The moment and moment coefficient contributions of the wing and stabilizer need to be evaluated. Secondly, the jet correction needs to be implemented for the horizontal stabilizer. The second set of implementations concerns the reference aircraft, the Fokker F-27, in an effort to increase the fidelity F-27 model. Where the wing model is expanded with the ability to model multiple airfoils, wing twist and an incidence angle. Lastly, the forces determined by the VLM and BEM module separately are combined to determine the total aircraft forces and moment. With these implementations in place, the tool is now referred to as ALIME.

The wing modeling implementation are covered in subsection 2.2.1. The implementations on the stabilizer in the VLM formulation are discussed in subsection 2.2.2. The jet correction implementation for the horizontal stabilizer is discussed in subsection 2.2.3. The total aerodynamic forces including the stabilizer are covered in subsection 2.2.4.

2.2.1. Wing Airfoil Slope, Twist and Incidence Angle

To increase the fidelity of the F-27 reference aircraft model in ALIME, the ability to model multiple airfoils, wing twist ε and incidence angle i are implemented. It is chosen to simplify these implementations by only

considering the effect of the multiple airfoils, wing twist and incidence angle on the normal velocities in the VLM system. The VLM panels of the wing will remain in the $z = 0$ plane, resulting in the AICs being unaffected by the airfoil, twist and incidence angle implementation. This leads to a small error in terms of the panel circulation. However, this error is expected to be negligible since the position of the panels would barely change when the wing twist and incidence angle would determine the VLM panel positions. The definition of the normal velocities V_n on the right hand side of the VLM system changes from Equation 2.2 to Equation 2.28, which already contain the mentioned implementations that are discussed individually.

$$V_n = V_\infty \left(\frac{\partial g}{\partial x}(y) - \alpha - \varepsilon(y) \right) + V_x \frac{\partial g}{\partial x} - V_z \tag{2.28}$$

Multiple Airfoils

The normal velocity of each of the VLM panels is a function of the camber line slope. Considering multiple airfoils means that the camber line slope changes with y. The F-27 features a different wing root and tip airfoil. The airfoils are implemented in ALIME to be specified by the user at the wing root and tip section. The change in camber line slope from root to tip is modeled as a linear change in root and tip airfoil camber line function (g_r and g_t) slope, as expressed by Equation 2.29. The local airfoil slope $\frac{\partial g}{\partial x}$ therefore becomes a function of the spanwise coordinate y.

$$\frac{\partial g}{\partial x}(y) = \left(\frac{\frac{\partial g_t}{\partial x} - \frac{\partial g_r}{\partial x}}{b/2} \right) y + \frac{\partial g_r}{\partial x} = \frac{\partial g_t}{\partial x} \frac{y}{b/2} + \left(1 - \frac{y}{b/2} \right) \frac{\partial g_r}{\partial x} \tag{2.29}$$

Wing Twist

The wing twist angle will tilt the airfoil camber line with respect to the incoming flow, affecting the normal velocities experienced by the VLM panel as a result of the twist. The wing twist is defined as zero at the wing root and equal to ε_t at the tip. The wing twist is therefore a function of y. The local wing twist $\varepsilon(y)$ is implemented as a linear change from the wing root to the tip, as given by Equation 2.30.

$$\varepsilon(y) = \varepsilon_t \frac{y}{b/2} \tag{2.30}$$

Incidence Angle

The incidence angle i_w of a wing affects the normal velocities of the VLM panel system in the same way as the wing twist. The incidence angle of a wing is the angle between the aircraft longitudinal body axis and the wing root chord line [44]. The AoA is the angle between the wing root chord line and the free stream velocity vector. The AoA of a wing is thus the sum of the incidence angle and the angle between the free stream velocity and the aircraft longitudinal axis. This aircraft longitudinal axis is taken to be the middle line of the aircraft fuselage, meaning that the latter of the mentioned angles effectively becomes the AoA of the fuselage α_f. For a wing, the AoA α can thus be expressed as a function of its incidence angle by means of Equation 2.31.

$$\alpha = \alpha_f + i_w \tag{2.31}$$

2.2.2. VLM Formulation for the Stabilizer

The addition of the horizontal stabilizer surface expands the old VLM system from Equation 2.1 to Equation 2.32.

$$\begin{bmatrix} \mathbf{C}_{ww} & \mathbf{C}_{wh} \\ \mathbf{C}_{hw} & \mathbf{C}_{hh} \end{bmatrix} \begin{bmatrix} \mathbf{\Gamma}_w \\ \mathbf{\Gamma}_h \end{bmatrix} = \begin{bmatrix} \mathbf{V}_{n_w} \\ \mathbf{V}_{n_h} \end{bmatrix} \tag{2.32}$$

Where the addition of the horizontal stabilizer panels results in three extra interactions that are captured with the AICs: the horizontal tail-on-horizontal tail interaction AICs $\mathbf{C}_{hh}$, the horizontal tail-on-wing interaction AICs $\mathbf{C}_{hw}$ and vise versa $\mathbf{C}_{wh}$.

One of the main goals of the horizontal stabilizer implementations is to not restrict the horizontal stabilizer to the $z = 0$ plane, requiring a change to the AIC computation formulation. In addition, restriction of the mesh on the horizontal stabilizer are imposed by means of mesh matching to keep ALIME more user friendly. The AIC formulation and mesh matching implementation for the stabilizer are discussed respectively.

AIC Formulation

The VLM formulation used for the horizontal stabilizer takes each element of the horseshoe vortex to be a bounded vortex, since its AIC calculation procedure (Equation 2.3) takes into account the z-position of the vortex filaments compared to the *farfield* method described in subsection 2.1.1. This is the most time efficient means of taking into account the z-position of the horizontal stabilizer because the procedure for determining Equation 2.3 numerically (described in section 10.4.5 by Katz and Plotkin [22]) is already present in PyVLM[1] by default. This decision to work with bounded horseshoe vortex elements has some consequences for the convergence behaviour of the VLM as is discussed later in subsection 3.2.1. The vortex filament at the horseshoe vortex LE is a bounded vortex located between e and f, just like in the *farfield* method. The two trailing vortex filaments now no longer extend to $+\infty$, but extend from e and f to $y = 1000c$. The total downwash by a horseshoe vortex again consists of the sum of three contributions of the bounded horseshoe vortex elements. The z-coordinate of each horseshoe vortex is now taken into account towards the computation of the AIC. This method of determining the AICs is referred to as the *3D* method in this thesis, because of the extension of the AIC computation outside of the $z = 0$ plane.

Mesh Matching

The induced velocity of a vortex filament increases asymptotically as a function of the distance to the filament core. When the distance to a vortex filament core goes to zero, the induced velocity created by that vortex filament will go to infinity. Even with an implemented viscous core, that sets the induced velocity to zero when the distance to the filament becomes smaller than $1e{-}12$, the induced velocity can become very large when approaching this threshold distance of $1e{-}12$.

A potential numerical problem arises when the mesh of the horizontal stabilizer and the wing is not controlled. If the trailing vortex filaments of the wing and stabilizer get positioned very close together (close to, but still larger than the threshold distance of $1e{-}12$), the resulting AIC will become very large. Resulting in a large increase in the Γ.

To prevent this problem, the mesh of the horizontal stabilizer and the part of the wing directly in front of the stabilizer is aligned. This leads to the situation depicted in Figure 2.3. Flexibility of mesh usage between the wing and stabilizer is traded off against a more user friendly experience in ALIME.

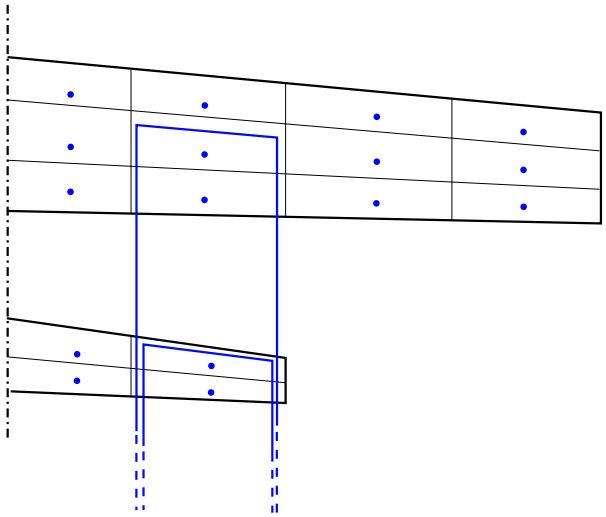

Figure 2.3: A visualization of the mesh matching implementation for the wing and horizontal stabilizer [58].

2.2.3. Jet Correction for the Stabilizer

With the addition of the horizontal stabilizer, the jet correction matrix is applied to the wing and stabilizer panels as shown by Equation 2.33.

$$\left(\begin{bmatrix} \mathbf{C}_{ww} & \mathbf{C}_{wh} \\ \mathbf{C}_{hw} & \mathbf{C}_{hh} \end{bmatrix} + \begin{bmatrix} \mathbf{G}_w & \mathbf{0} \\ \mathbf{0} & \mathbf{G}_h \end{bmatrix}\right) \begin{bmatrix} \mathbf{\Gamma}_w \\ \mathbf{\Gamma}_h \end{bmatrix} = \begin{bmatrix} \mathbf{V}_{n_w} \\ \mathbf{V}_{n_h} \end{bmatrix}, \tag{2.33}$$

Where $\mathbf{G}_w$ and $\mathbf{G}_h$ are the jet correction matrices for the wing and stabilizer respectively. Despite the wing and horizontal stabilizer having the same y-positions for the horseshoe vortex CPs due to the the mesh align-

ment implementation described in subsection 2.2.2. The jet correction is calculated separately for the horizontal stabilizer, since the odd part of the jet correction is not only dependent on the horseshoe vortex CP y-positions, but also on the lifting surface chord length. However, the even part of the jet correction will be the same for the wing and stabilizer $\mathbf{G}_{even_w} = \mathbf{G}_{even_h}$.

The main assumption for this implementation is that the radius of the propeller slipstream at the horizontal stabilizer is the same uncontracted radius of the slipstream at the propeller disk. The jet center line is also taken to lie at the same vertical position as the horizontal stabilizer for the purpose of the calculation of the jet correction at the stabilizer, $z_p = z_h$, regardless of the determined vertical slipstream center line position by the slipstream deflection.

The complete implementation of the jet correction for the stabilizer conists of the implementation of co-rotating propellers and the jet correction itself for counter and co-rotating propellers. All three of which are discussed respectively.

Co-rotating Propellers

The F-27 features two IB co-rotating propellers that rotate CCW when looking from the front which slipstream will interact with both the wing and the stabilizer and thus requires ALIME to have the ability to model co-rotating propeller.

ALIME performs calculations for the right wing propeller performance map and slipstream tube with a user specified rotation direction. The results of the right side propeller disk and slipstream tube are copied to the left wing and given the opposite rotation direction when dealing with IB Up (IU) and IB Down (ID) rotating propeller configurations. It is assumed that the right and left wing propellers do not affect each other [27]. To allow for the co-rotating propellers, the initial rotation direction is not switched sign when copying the right wing propeller performance and slipstream tube to the left wing, allowing ALIME to handle CW or CCW rotating propellers.

IU and ID Jet Correction

The jet correction for IB propellers (implemented by van der Leer) is calculated between the wing tip an propeller center line on the wing. The jet correction coefficients are then mirrored and copied to the wing section between the propeller center line and the wing root because of symmetry around the propeller center line position. The jet correction coefficients that go beyond the wing root are ignored, see Figure 2.4. Determining the jet correction in this fashion is possible because the induced downwash coefficients magnitudes $\mathbf{G}$ decrease quickly away from the propeller jet boundary and the symmetry of the correction around the propeller jet center line [41, 35]. With the assumption that the panels of each wing half do not interact with each other, the jet correction of one wing half is mirrored to the other wing half to complete $\mathbf{G}_w$, see Figure 2.5. The mirroring of segments of the jet correction can be done since the correction is mostly prominent near the jet and the jet boundary [27].

A problem arises for a horizontal stabilizer since the section between the stabilizer tip and propeller center line is shorter than the section between the stabilizer root and propeller center line. There is not enough length available to calculate the jet correction beyond the propeller center line and then mirror it to the stabilizer section between the root and jet center line. To solve this issue, the jet correction calculation is performed between the stabilizer root and propeller center line and then mirrored to the shorter stabilizer section beyond the propeller center line. This new implementation does not just apply to a horizontal stabilizer, but to any lifting surface where the section between the stabilizer tip and propeller center line is shorter than the section between the root and propeller center line.

To determine whether the jet correction needs to be calculated in between the root and propeller center line or beyond the propeller center line for a particular lifting surface, ALIME first determines if the propeller center position is located at $y_p \leq b/4$ like for an IB propeller, or $y_p > b/4$ for an OB propeller. In the case of an IB propeller, the jet correction is calculated between the lifting surface root and propeller center line, then mirrored to the section beyond the propeller center and ignoring all the correction coefficient beyond the span of the lifting surface. This process is also depicted in Figure 2.4 for the horizontal stabilizer. The opposite is also true. Lastly, the jet correction coefficients are mirrored to the other wing half, as shown in Figure 2.5.

The jet correction procedure introduces limitations for the mesh that can be selected. The mesh within the propeller jet has to have an uneven number of spanwise panels to ensure that the middle panel CP intersects with the propeller center line. The number of spanwise panels on the wing must therefor be uneven. To allow the mirroring during the first step shown in Figure 2.4 of the jet correction to function, the mesh in the

wing sections on both sides of the propeller jet must has the same amount and distribution of spanwise and chordwise panels [27].

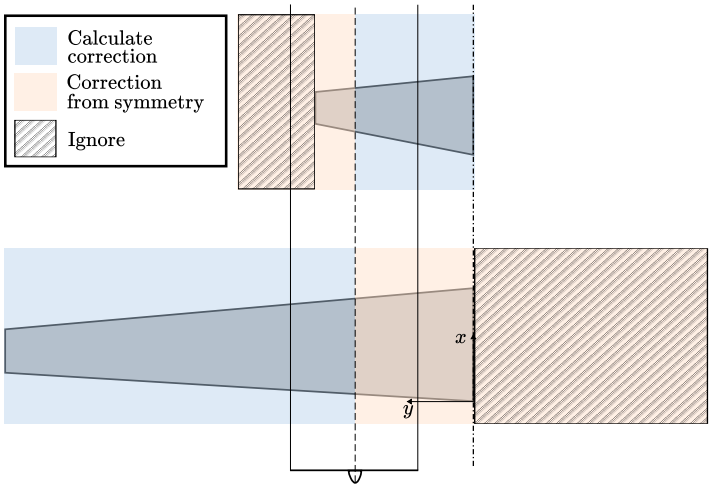

Figure 2.4: A schematic showing the first step of the jet correction calculation procedure for the wing by van der Leer and the newly implemented variant for the horizontal stabilizer (imaged inspired by and adapted from [27]).

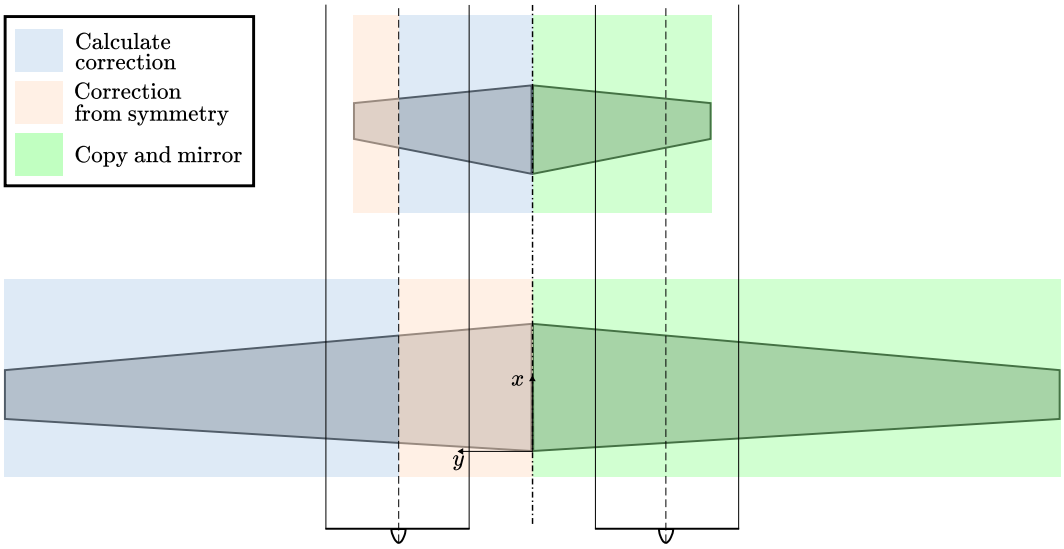

Figure 2.5: A schematic showing the second step of the jet correction calculation procedure for the wing and horizontal stabilizer (imaged inspired by and adapted from [27]).

Co-Rotating Propeller Jet Correction

In the case of co-rotating propellers, the velocity ratio distribution μ created by the propeller slipstream becomes asymmetric between both wing halves. Meaning that the jet correction calculated on the right wing would be different from the one calculated on the left wing, since the jet correction is a function of μ. The jet correction is no longer only calculated on the right wing and copied to the left wing when the right and left wing have an asymmetrical μ-distribution. The procedure for the jet correction calculation on the right wing for counter rotating propellers is performed on both the left and right wing for the co-rotating propellers. The Figure 2.6 illustrates the procedure of the jet correction calculation in the case of co-rotating propellers. This implementation doubles the computational time for the jet correction since it is calculated twice. The computational time of the jet correction is discussed in subsection 3.2.2. For the horizontal stabilizer, the procedure of determining the jet correction is again exactly opposite compared to the wing.

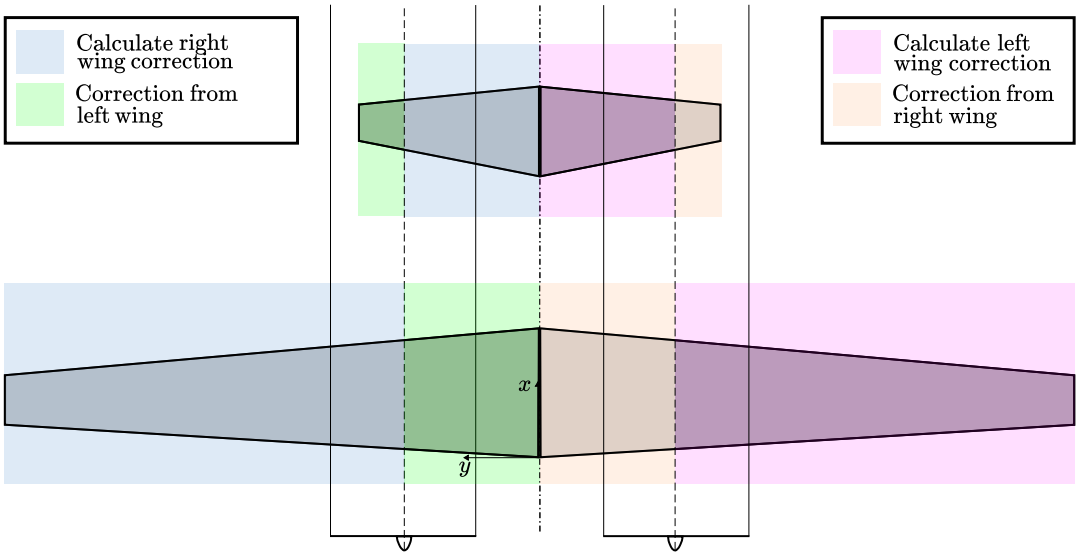

Figure 2.6: A schematic showing the jey correction calculation procedure for the wing and horizontal stabilizer in the case of co-rotating (CW or CCW) propellers.

2.2.4. Total Lift and Moment Coefficient

With the implementation of the horizontal stabilizer in ALIME, the total lift and moment of the wing-horizontal stabilizer-propeller system can be evaluated. This section discusses how VLM and BEM module results are combined to obtain the total lift and moment coefficients in ALIME. The total lift and moment coefficient are discussed separately.

Total Lift Coefficient

The lift coefficient of the wing and stabilizer surfaces are calculated in the VLM module in ALIME. The propeller force contributions, determined by the non-uniform inflow analysis of the propeller in the BEM module, are added to the lift to obtain the total lift coefficient. This is done according to Equation 2.34, which uses the aerodynamic reference system aligned with the free stream velocity. The thrust and normal force of the propeller disk are taken from the non-uniform inflow quasi-steady model. The unsteady correction in the non-uniform inflow analysis does not affect these quantities [9].

$$L_{tot} = L_w + L_h + \Delta T_p \sin(\alpha_p) + \Delta N_p \cos(\alpha_p), \qquad C_L = \frac{L_{tot}}{q_\infty S_w} \tag{2.34}$$

The propeller can also be mounted with a specific incidence angle i_p relative to the aircraft body axis. The total AoA of the propeller disk α_p is then expressed as Equation 2.35, which is very similar to the AoA definition of a wing.

$$\alpha_p = \alpha_f + i_p \tag{2.35}$$

Total Moment Coefficient

The distances that define the moment arms to the reference point are determined in the body-axis of the aircraft, which lies parallel to the $z = 0$ plane in ALIME. The normal and axial forces of the wing and stabilizer VLM panels, N and A, as well as the propeller thrust and normal forces resulting from the non-uniform inflow analysis, ΔT_p and ΔN_p all contribute to the moment of the modeled aircraft. Note that ΔT_p and ΔN_p are the total thrust and normal force contributions of all present propellers. The complete aircraft moment coefficient is implemented in ALIME according to Equation 2.36

$$\begin{aligned} M_{tot} = &\sum_{n_w m_w} \left[N_w \left(x_{ref} - x_{CP_w} \right) - A_w \left(z_{ref} - z_{CP_w} \right) \right] - \sum_{n_h m_h} \left[N_h \left(x_{ref} - x_{CP_h} \right) - A_h \left(z_{ref} - z_{CP_w} \right) \right] \\ &+ \Delta T_p \sin(i_p) \left(x_{ref} - x_p \right) + \Delta T_p \cos(i_p) \left(z_{ref} - z_p \right) + \Delta N_p \cos(\alpha) \left(x_{ref} - x_p \right) - \Delta N_p \sin(\alpha) \left(z_{ref} - z_p \right) \\ C_M = &\frac{M_{tot}}{q_\infty S_w \bar{c}_w} \end{aligned} \tag{2.36}$$

The contributions of each wing and stabilizer panel normal and axial force are counted towards to moment individually. The moment arm distance for the normal and axial force of a single panel is equal to the distance between the panel CP and the reference point. The sum of all the panel contributions to the moment cover the contribution of the wing and stabilizer. For the wing and stabilizer, the total number of panels is equal to the product of the number of chordwise and spanwise panels respectively: $n_w m_w$ and $n_h m_h$. The panel moment contributions would represent the entire aircraft moment in the case where no propellers are present. In the presence of a propeller, the slipstream induced velocities will affect the panel forces and therefore their contribution to the aircraft moment. For the propeller force contributions, the i_p is used to align the propeller force contributions with the aircraft body axis.

3

Verification, Validation and Sensitivity Analysis

This chapter is about the testing of the abilities and limitations of ALIME. The implementations made to ALIME, described in section 2.2, are verified in section 3.1. A sensitivity analysis of ALIME is presented in section 3.2. Lastly, the validation discussed in section 3.3 compares predictions of ALIME to wind tunnel data. Some of the assumptions/simplifications mentioned in chapter 1 are tested in this chapter.

3.1. Verification

The implementations to ALIME are verified in this section. First the implementations to the VLM module, namely the implementations to the wing and the horizontal stabilizer, are covered in subsection 3.1.1 and 3.1.2 respectively. A comparison is performed between ALIME and the open source VLM XFLR5 [58]. The implementation verification for the jet correction for the horizontal stabilizer is discussed in subsection 3.1.3.

3.1.1. Wing Implementations

This section focuses on the verification of the implementations to the wing model in ALIME, namely the multiple airfoils and wing twist as described in subsection 2.2.1. The F-27 reference aircraft geometry for the TU Delft model, as described in Appendix A, is utilized for the verification. The multiple airfoil implementation and wing twist implementation verification are discussed respectively.

Multiple Airfoils

Figure 3.1 shows a comparison of the lift distribution of the TU Delft F-27 model in ALIME and XFLR5 at $\alpha = 3.46^{\circ}$. The wing twist is set to zero to isolate the effect adding the extra airfoil. To see the effect of the airfoil implementation, the F-27 wing lift distribution with the root airfoil at both the root and wing tip and the root and tip airfoil at their respective wing section is computed for both ALIME and XFLR5.

Good agreement is observed between ALIME and XFLR5. Especially for the case where the F-27 wing is fitted with just the root airfoil. In the case of different root and tip airfoil, the sectional lift coefficient C_{l_w} increases in the mid-wig region for both ALIME and XFLR5. A possible explanation for the slightly higher C_{l_w} by XFLR5 for the root and tip airfoil wing is a different implementation for the interpolation of the airfoil camber line between the wing root and tip section. However, this cannot be confirmed when inspecting the XFLR5 user manual [58].

Twist

To verify the wing twist implementation, a comparison is set up between ALIME and XFLR5 for the same F-27 isolated wing geometry that is used for the multiple airfoil implementation. The root and tip section of the wing feature their respective airfoil sections as mentioned in Appendix A. Note that the incidence angle of the wing is set to $i_w = 3.27^{\circ}$, to allow for a more fair comparison with the F-27 lift distribution by Veldhuis. Although similar, the geometry of Veldhuis' F-27 model is slightly different compared to the F-27 geometry of the TU Delft model [54]. The main differences are a slightly larger wing span of $30m$ and the wing incidence angle. First the wing lift distribution of the F-27 wing is computed by ALIME and XFLR5 without any twist

$\varepsilon = 0°$. Next, the lift distribution is determined with a linear wing twist of $\varepsilon = -2°$ for both ALIME and XFLR5. Figure 3.2 shows the comparison of these two cases.

The lift distribution of both ALIME and XFLR5 agree well for the case where $\varepsilon = 0°$, but a clear difference in sectional lift is observed when the $\varepsilon = -2°$ is introduced. The difference in wing lift can be explained by the different implementation of wing twist in ALIME and XFLR5. In ALIME, the wing twist is implemented as a linear change in VLM panel normal velocities only, leaving the panel orientations and thus the AIC matrix unaffected as described in subsection 2.2.1. In XFLR5 wing twist is implemented in both the VLM panel orientation and the normal velocities, affecting the AIC matrix and the normal velocity vector, resulting in a different circulation vector solution [58].

The lift distribution by ALIME is closer to the one by the VLM model by Veldhuis compared to the one by XFLR5. The implementation for the linear wing twist in ALIME is therefore deemed to be more acceptable for this thesis project compared to the one in XFLR5 in the case of the F-27. Veldhuis' implemented the wing twist to start at the propeller center line position, as is te case for the real F-27. The consequence of the linear implementation of the wing twist from root to tip in ALIME is a slightly lower C_{l_w} in the mid-wing regions, resulting in a slightly lower wing lift coefficient C_{L_w} compared to Veldhuis for the same wing incidence angle.

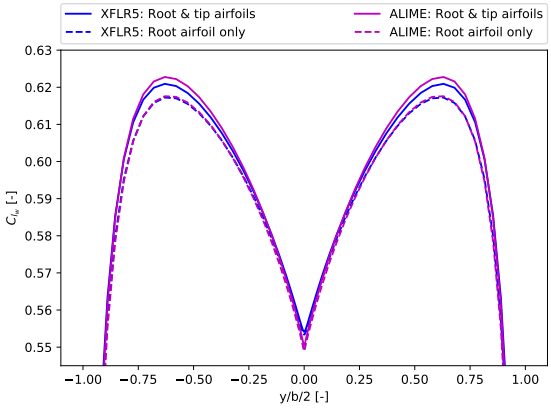

Figure 3.1: A comparison between the TU Delft F-27 model isolated wing lift distribution with root and tip airfoil and root airfoil only of ALIME and XFLR5, at $\alpha = 3.46°$, zero twist $\varepsilon = 0°$ and $i_w = 3.46°$.

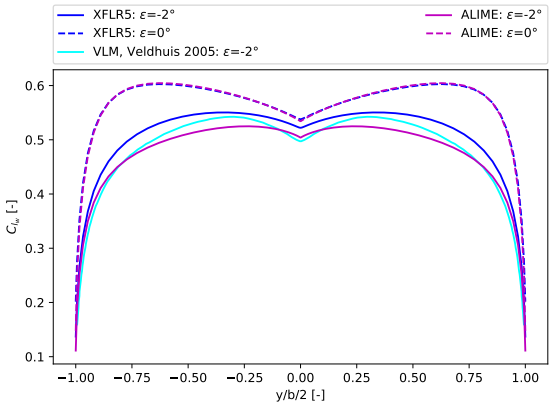

Figure 3.2: A comparison between the TU Delft F-27 model isolated wing lift distribution of ALIME, XFLR5 and the VLM by Veldhuis [54], at $\alpha = 3.27°$, $i_w = 3.27°$ for $\varepsilon = -2°$ and 0°.

3.1.2. Horizontal Stabilizer Implementation

To verify the VLM formulation and mesh matching implementation of the horizontal stabilizer as described in subsection 2.2.2, and the lift and moment coefficient as described in subsection 2.2.4 without the propellers. the TU Delft F-27 model with stabilizer is analyzed on the AoA range of -1.54° to 8.46° using ALIME and XFLR5 for the root and tip airfoil, $i_w = 3.46°$ and $\varepsilon = -2°$. The initial assumption of the axial panel force contribution to C_M is also tested in this section.

VLM Formulation and Mesh Matching

Figure 3.3 shows the lift distribution of the wing and stabilizer of the F-27 at an AoA of $\alpha = 3.46°$. Good agreement is observed for the lift distribution of ALIME and XFLR5, although XFLR5 yields a slightly higher C_{l_w} on the OB side of the wing. A kink in the XFLR5 C_{l_w} distribution is also observed at $y = \pm b_h/b_w$. This kink is a result of the process to ensure an identical mesh for both ALIME and XFLR5 in this analysis, which requires a wing section to be manually specified in XFLR5 at $y = \pm b_h/b_w$. The interpolated airfoil and wing twist angle therefore have to be specified at $y = \pm b_h/b_w$ in XFLR5, while ALIME determines the wing twist and airfoil camber line slope according to the linear change, as described in subsection 2.2.1. When inspecting the stabilizer C_{l_h}, very good agreement between XFLR5 and ALIME is observed.

Total Lift and Moment Coefficient Without Propellers

The comparison in lift and moment coefficient for ALIME and XFLR5 of the F-27 model without propellers is presented in Figure 3.4 and 3.5 respectively.

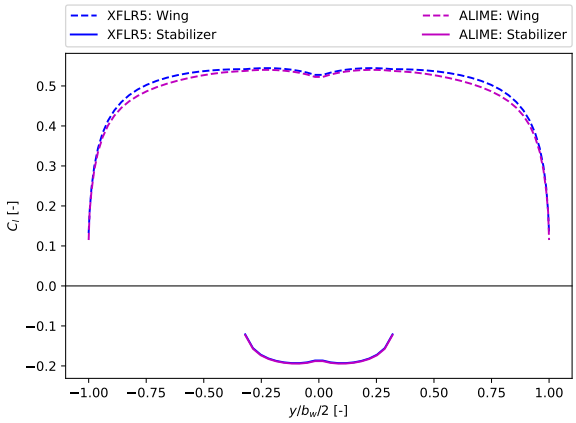

Figure 3.3: The lift distribution of the TU Delft F-27 model for the wing and stabilizer as predicted by ALIME and XFLR5 at $\alpha = 3.46^\circ$ and $\varepsilon = -2^\circ$

The lift coefficient curve by XFLR5 is slightly higher compared to ALIME. This is a direct result of the slightly higher C_{l_w} of XFLR5 compared to ALIME shown in Figure 3.3.

The moment curves of ALIME and XFLR5 have a slightly different slope. This different is not a result of the wrong panel force application point. A test is performed where the panel forces are applied at $c/2$ in each panel instead of at the CP at $\frac{3}{4}c$, the resulting moment coefficient magnitude and slope is completely different. The difference between the C_{M_α} of ALIME and XFLR5 is therefore thought to originate from the small errors in panel normal and axial force predictions adding up because of the sum terms in Equation 2.36 used to determine C_M.

The effect of not taken into account the axial force contributions to C_M is also checked to verify the initial assumption on the axial force contribution to C_M. The C_{M_α} is barely affected, resulting in only a small change in C_M at high AoA. Not taking into account the contribution of the axial panel forces to C_M is concluded to be acceptable simplification for the F-27, especially for low AoA.

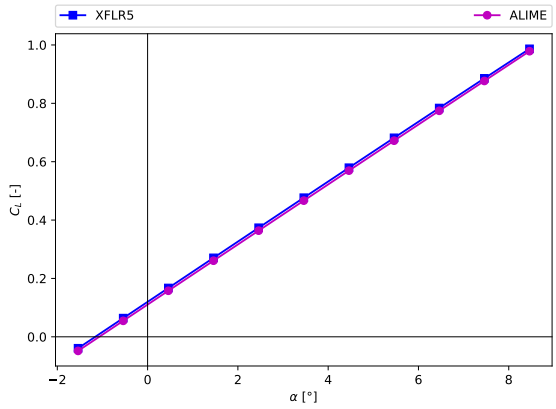

Figure 3.4: A comparison between the lift coefficient curve of the TU Delft F-27 wing and stabilizer combination as predicted by ALIME and XFLR5.

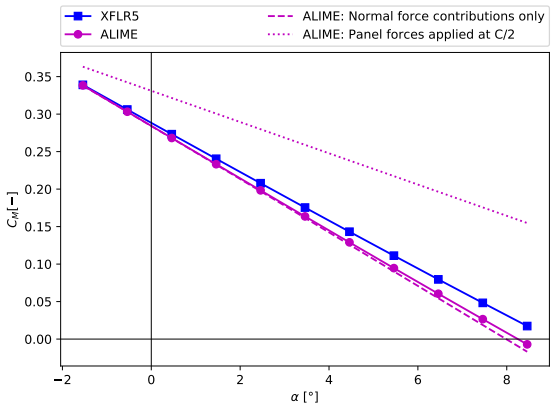

Figure 3.5: A comparison between the moment coefficient curve of the TU Delft F-27 wing and stabilizer combination as predicted by ALIME and XFLR5.

3.1.3. IB vs OB Propeller Jet Correction

This section aims to verify the implementation of the jet correction for an OB propeller, where the propeller center line is located on the OB section of a wing $b_w/2 < y_p \leq b_w$. The implementation of which is discussed in subsection 2.2.3. It is mentioned that the jet correction can be determined on the IB or OB section of a wing depending on the position of the propeller center line position. The jet correction should yield the same result, regardless of the jet correction being determined on the IB or OB because of symmetry in horseshoe

vortex lay-out around the propeller center line when considering one wing half.

A verification case is therefore set-up to confirm that the implementation results in the same jet correction solution for an OB and IB located propeller. Two $b_w = 100m$ and $c = 1m$ wings, featuring a symmetric airfoil section, with ID rotating propellers located a distance $dy = \pm 0.001m$ from the halfway point $y_p = b_w/4$ of a wing half respectively are considered. Making the propeller located at $y_p = b_w/4 - dy$ an IB propeller and the propeller at $y_p = b_w/4 + dy$ an OB propeller. Figure 3.6 shows the described situation situation. The PROWIM propeller model, which is introduced in section 3.3, is used for this verification case. The propeller is set to operate at $J = 0.85$ with $\beta = 25°$ at 75% R_p. The jet correction is meant to correct the AIC matric in the VLM system and will thus have a direct effect of the circulation solution and therefore on the lift and the lift distribution. If the jet correction is implemented correctly for both the IB and OB propeller situation, their lift distributions are exactly the same, but displaced by a y-distance equal to $2dy = 0.002m$. Figure 3.7 shows the lift distribution for both the IB and OB propeller. To show that that the jet correction works as intended, the lift distributions is shown for the case where the jet correction is and is not applied.

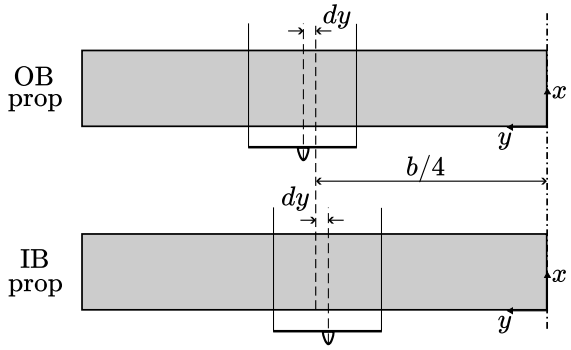

Figure 3.6: A schematic of the case used to verify the OB propeller jet correction implementation where $b_w = 100m$ and $dy = 0.001m$.

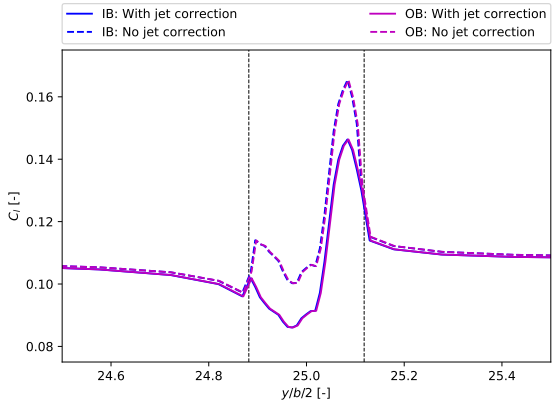

Figure 3.7: A comparison of the lift distribution for the IB and OB propeller case at $\alpha = 1°$ with $J = 0.85$ with $\beta = 25°$ at 75%R_p.

3.2. Sensitivity Study

Willemsen performed an extensive sensitivity study of his version of ALIME in the context of WTMPs [56]. With the implementation to ALIME necessary for this thesis project, it is expected that some of the properties of the tool might have changed. Some of the sensitivity studies performed by Willemsen are therefore revisited. A sensitivity study on the mesh resolution in the ALIME VLM module is discussed in subsection 3.2.1. The integration variables for the jet correction in the VLM module are covered in subsection 3.2.2.

3.2.1. Mesh Resolution

A mesh resolution sensitivity study is especially of interest because of the many changes made to the VLM module of ALIME. An extra lifting surface, the horizontal stabilizer, is added to the VLM formulation, the wing model is extended with multiple airfoils, twist and an incidence angle. Furhtermore, the computational method for the AIC matrix is changed with respect to Willemsen's version of ALIME.

To see how these implementation possibly might have affected the convergence behaviour of the ALIME VLM, a sensitivity study is performed. This section further serves to select the mesh to be used for the analysis of the F-27 isolated wing and wing-horizontal stabilizer combination without propellers. The mesh resolution sensitivity study for the isolated wing is first discussed, followed by the wing-stabilizer combination.

Isolated Wing

As is explained in subsection 2.1.1, the VLM formulation before the implementations for this thesis project used the *farfield* method to determine the AICs. For the purpose of considering the z-position of the horizontal stabilizer in the AIC calculation process, the VLM formulation is changed to the *3D* method as stated in subsection 2.2.2. The first goal of this section is to discover the differences in the convergence behaviour of the *farfield* and *3D* methods for the AIC determination. Furthermore, a mesh is selected for the analysis of the isolated wing of the F-27.

The mesh sensitivity analysis is performed by running ALIME with the isolated wing of the F-27 TU Delft model for 1, 5, 10, 20, 30, 40, 50 and 60 n chordwise and m spanwise panels with an uniform spanwise and cosine chordwise mesh distribution, at an AoA of 5.46°. The C_{L_w} and C_{M_w} are determined both using the *farfield* and *3D* method to determine the AICs. To obtain C_{L_w} and C_{M_w} at every integer value combination of n and m, a cubicly interpolation is applied prevent running ALIME for every possible integer combination of n and m. This creates a Two-Dimensional (2D) convergence space.

The difference between the convergence behaviour of the C_{L_w} and C_{M_w}, determined using the *farfield* and *3D* AIC calculation, is presented in Figure 3.8 and 3.9, where the convergence along the lines $n = 60$, $m = 60$ and $n = m$ are shown. The *farfield* and *3D* methods both converge similarly for C_{L_w} until about $n = 20$ and $m = 31$, from where the *3D* method starts to converge to a different C_{L_w} at $n = m = 60$ compared to the *farfield* method. A similar observation is made for C_{M_w}, although the difference between the *farfield* and *3D* method convergence becomes apparent at higher n and m compared to the lift coefficient and the *farfield* and *3D* methods both converge to only sightly different C_{M_w} values. Remember that the main difference between the *farfield* and *3D* method is the formulation of the trailing horseshoe vortex elements. The *farfield* trailing vortex elements extend to $+\infty$ compared to $1000c$ for the *3D* method, which are determined using slightly different formulations of the Biot-Savart law. The only difference between the two methods being the 3D dimension being taken into account for the *3D* method, while the *farfield* method works in a 2D plane only. This difference between the method only becomes apparent for C_{L_w} and C_{M_w} at higher mesh resolutions. Willemsen has performed an extensive validation of the lift coefficient prediction by his version of ALIME, which used the *farfield* method, and showed good agreement with wind tunnel data [56]. The *farfield* method results are thus considered to be correct for all panel resolutions, while the *3D* method results at high panel resolutions are distrusted.

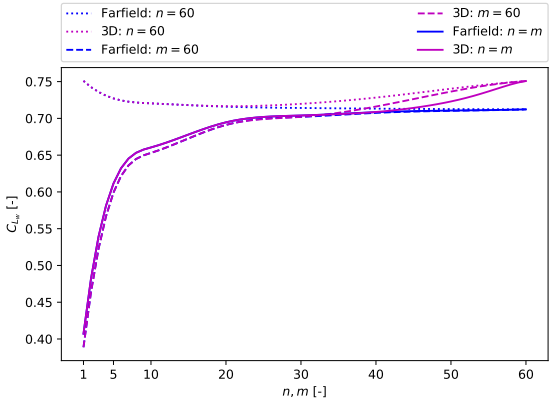

Figure 3.8: The convergence space of the F-27 TU Delft model C_{L_w} as determined with the *farfield* and *3D* method along the lines $n = 60$, $m = 60$ and $n = m$ at $\alpha = 5.46°$.

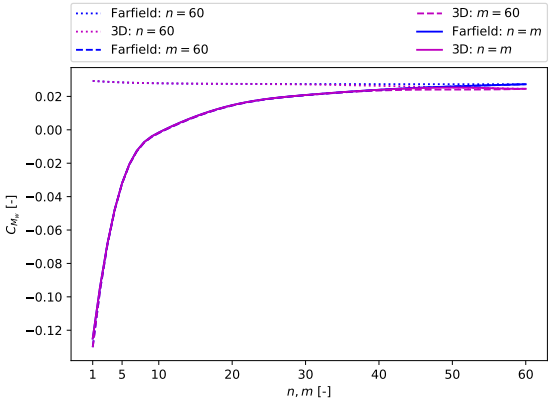

Figure 3.9: The convergence space of the F-27 TU Delft model C_{M_w} as determined with the *farfield* and *3D* method along the lines $n = 60$, $m = 60$ and $n = m$ at $\alpha = 5.46°$.

The investigation between the convergence of the *farfield* and *3D* method AIC formulations leads to the conclusion that the *3D* method results can only be trusted until a certain mesh resolution. This is problematic since the current ALIME VLM formulation uses the *3D* method. An upper mesh resolution boundary is determined until what mesh resolutions the results determined with the *farfield* and *3D* method can be considered the same. The upper boundary indicates where the *farfield* and *3D* method lift and moment coefficient start to differ more then a particular threshold: $\Delta C^*_{L_w} = |C^{far}_{L_w} - C^{3D}_{L_w}|$ and $\Delta C^*_{M_w} = |C^{far}_{M_w} - C^{3D}_{M_w}|$, as shown in Figure 3.10 and 3.11. For the purpose of this thesis, this threshold is set to $\Delta C^*_{L_w} = 1e{-}3$. This upper boundary needs to be considered during the mesh selection procedure for the F-27 wing. For any mesh resolution above this boundary one now knows that C_{L_w} and C_{M_w} determined using the *3D* method are different compared to the *farfield* method based on the observed convergence behaviour for both AIC formulations.

Lower boundaries for the convergence in the n and m-direction specifically are also determined. Convergence in the n and m-direction (superscript n and m) is determined by observing at what panel resolution the change in C_{L_w} and C_{M_w} is less or equal then a particular threshold: $\Delta C^n_{L_w} = \left|C^{far}_{L_w}|_n - C^{far}_{L_w}|_{n-1}\right|$, $\Delta C^n_{M_w} = \left|C^{far}_{M_w}|_n - C^{far}_{M_w}|_{n-1}\right|$. This threshold is set to $1e-4$ in the m-direction and $1e-3$ in the n-direction for both the lift and moment coefficient, because the rate of convergence differs in each direction. The con-

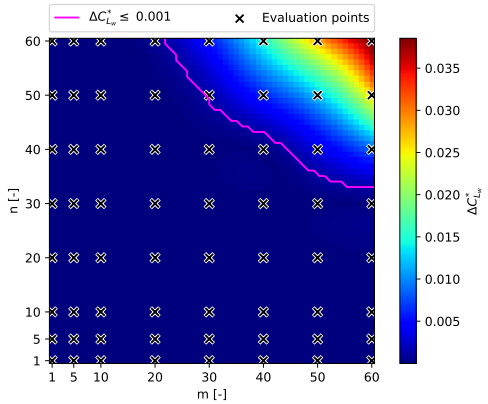

Figure 3.10: The difference field of the F-27 TU Delft model C_{L_w}, as determined with the *farfield* and *3D* method at $\alpha = 5.46°$, with the difference threshold boundary contour $\Delta C^*_{L_w}$ of $1e-3$.

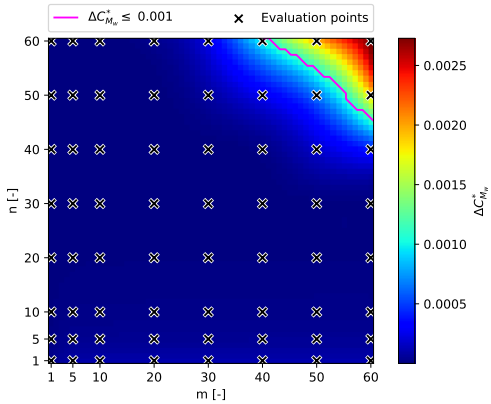

Figure 3.11: The difference field of the F-27 TU Delft model C_{M_w}, as determined with the *farfield* and *3D* method at $\alpha = 5.46°$, with the difference threshold boundary contour $\Delta C^*_{M_w}$ of $1e-3$.

vergence threshold of $1e-4$ for the n-direction is not even reached within the evaluated space of panel resolutions. Reaching this convergence threshold of $1e-4$ in the n-direction would have required an increase in the considered panel resolution space beyond $n = 60$, which is deemed not to be useful for this project due to very slight increase in solution accuracy and a very large increase in computational time which is experienced above the mesh resolutions of $n, m > 60$. Figure 3.12 and 3.13 show the convergence space of the lift and moment coefficients respectively. The lower convergence boundaries are given by:

$$\Delta C_{L_w} = \frac{\left|C^{3D}_{L_w} - C^{ref}_{L_w}\right|}{\max\left(\left|C^{3D}_{L_w} - C^{ref}_{L_w}\right|\right)}, \quad \Delta C_{M_w} = \frac{\left|C^{3D}_{M_w} - C^{ref}_{M_w}\right|}{\max\left(\left|C^{3D}_{M_w} - C^{ref}_{M_w}\right|\right)},$$

where the reference values are $C^{ref}_{L_w} = C^{far}_{L_w}|_{n,m=60}$ and $C^{ref}_{M_w} = C^{far}_{M_w}|_{n,m=60}$. Figure 3.12 and 3.13 indicate that $m = 28$ and $n = 23$ would be the lowest satisfactory mesh resolution for the isolated wing of the F-27.

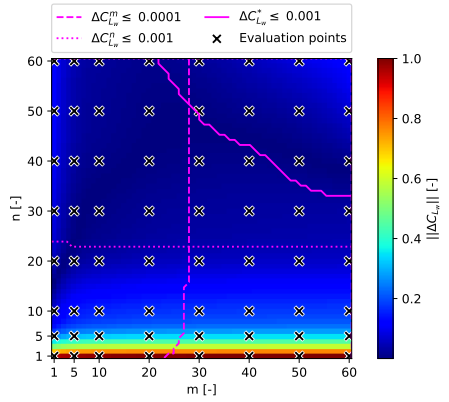

Figure 3.12: The convergence space of the F-27 TU Delft model isolated wing C_{L_w} as determined with the *3D* method at $\alpha = 5.46°$, with the lower and upper n and m-direction convergence boundaries.

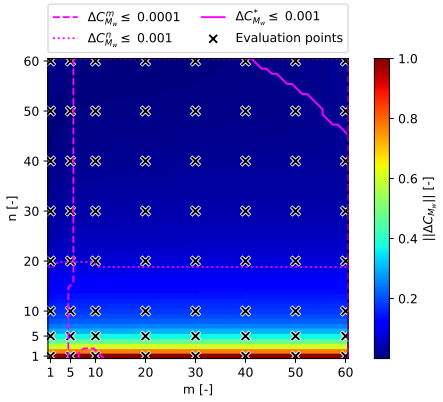

Figure 3.13: The convergence space of the F-27 TU Delft model isolated wing C_{M_w} as determined with the *3D* method at $\alpha = 5.46°$, with the lower and upper n and m-direction convergence boundaries.

Wing and Stabilizer

A suitable mesh for the analysis of the F-27 wing-stabilizer combination is sought in this section. The same conditions apply as for the isolated wing mesh sensitivity analysis, but the evaluated mesh resolutions are compared differently to the isolated wing. The mesh matching implementation of the horizontal stabilizer limits the mesh that can be selected for the wing-stabilizer combination as explained in subsection 2.2.2. The

main wing is split into two sections at the location of the stabilizer span y-coordinate, an IB and OB section. The ratio of the span of the IB and OB wing sections relative to the wing span is about $\frac{1}{3}$ for the wing IB section that is directly in front of the stabilizer and $\frac{2}{3}$ for the OB wing section. In an effort to keep the AR of the mesh panels about the same between this IB and OB sections of the wing, one third of the total spanwise panels ($\frac{1}{3}m$) is positioned in the IB section, while the other two-thirds of the spanwise panels ($\frac{2}{3}m$) is positioned on the OB wing section. The evaluated mesh resolution combinations are therefore all taken as factors of three: 3, 9, 18, 27, 36, 45 and 54.

Compared to the isolated wing analysis, the lift and moment coefficient can only be determined using the *3D* method as described because of the presence of the horizontal stabilizer located at a different z-coordinate compared to the wing. The convergence field is determined by:

$$\Delta C_L = \frac{\left|C_L^{3D} - C_L^{ref}\right|}{\max\left(\left|C_L^{3D} - C_L^{ref}\right|\right)}, \quad \Delta C_M = \frac{\left|C_M^{3D} - C_M^{ref}\right|}{\max\left(\left|C_M^{3D} - C_M^{ref}\right|\right)}.$$

The reference values for the convergence fields are taken to be the lift and moment coefficient at the highest evaluated mesh resolution: $C_L^{ref} = C_{L_w}^{3D}|_{n,m=54}$ and $C_M^{ref} = C_{M_w}^{3D}|_{n,m=54}$. Even though it is known that the lift and moment coefficient converge to a different value for high mesh resolutions as compared to the *farfield* method. The n and m-direction convergence criteria identify the mesh resolutions from which the change in lift and moment coefficient will again exceed the set threshold, automatically creating an upper boundary for the mesh resolutions in addition to the lower boundary as shown in Figure 3.14 and 3.15.

The cubic interpolation between the evaluation mesh resolution points does not result in a constant decreasing rate of the function in both the n and m-direction. The cubic interpolation creates a 2D surface through all evaluated points using a third degree polynomial basis functions. The cubicly sometimes switches its slope quickly in a short distance to fit through all data points, locally triggering the lower boundary criteria to detect changes that exceed the threshold. For both the C_L and C_M this occurs multiple times in both the n and m-direction. For example, a circle shaped boundary is created for C_L at around $m, n = 31,38$ for the convergence boundary in the m-direction. This circle shapes convergence boundary is ignored, because it is purely a result of the cubic interpolation. Multiple vertically positioned convergence boundaries are created for C_M at the lower m values. In this case, the right most vertical convergence boundary at around $m = 18$ is accepted as the lower convergence boundary for C_M. The circle shaped convergence boundary for C_M in the top right corner is also ignored. Keeping the consequences of the cubic interpolation in mind, the mesh $m = 30$ and $n = 25$ is observed to be the lowest satisfactory mesh resolution for the analysis of the F-27 wing-stabilizer combination.

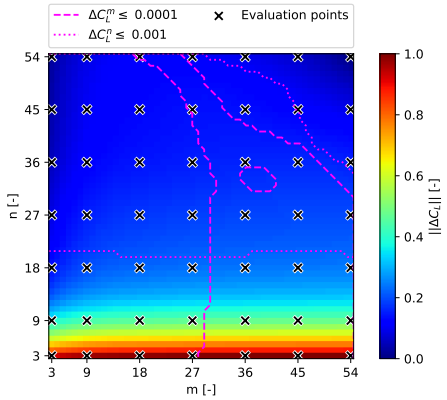

Figure 3.14: The convergence field of the F-27 TU Delft model wing-stabilizer combination $C_L = C_{L_w} + C_{L_h}$ as determined with the *3D* method at $\alpha = 5.46°$, with the n and m-direction convergence boundaries.

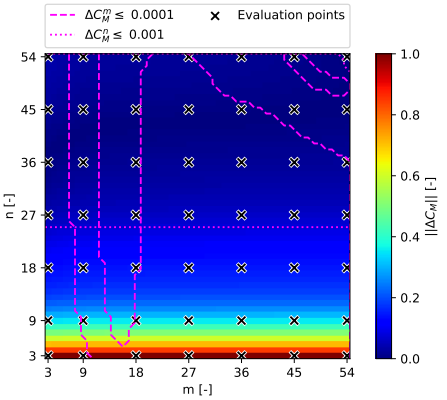

Figure 3.15: The convergence field of the F-27 TU Delft model wing-stabilizer combination $C_M = C_{M_w} + C_{M_h}$ as determined with the *3D* method at $\alpha = 5.46°$, with the n and m-direction convergence boundaries.

3.2.2. Intergration Variables

The odd part of the Rethorst correction contains integral terms, which are solved numerically using the integration variables p, λ and $(\lambda\beta)$. Choosing the appropriate values for these integration variables is a trade-off

between computational accuracy and computational time. Each integration variables has an associated step size and maximum value, both of which influence the computational accuracy. The computational accuracy and computational time is investigated as a function of $d\lambda$, λ_{max}, $d(\lambda\beta)$ and $(\lambda\beta)_{max}$ by considering the wing in jet geometry experimental case (without swirl) by Stüper [50], which is used by Rethorst for the verification of the Rethorst correction procedure [41]. The system used, is a Lenovo Y50-100 UHD, with 16 Gigabites of RAM and an Intel I7-4710HQ 2.5GHz processor. Willemsen also performed a sensitivity study on the integration variables for $\mathbf{G}_{odd}$. The sensitivity study is performed again but more elaborately to investigate if the new implementations to the ALIME lead to unexpected changes and to optimize the $\mathbf{G}_{odd}$ evaluation for the specific system used for this thesis project, since the jet correction implementation for co-rotating propellers requires the jet correction to be computed on both the left and right wing. Doubling the required jet correction determination computational time.

Nederlof has investigated the sensitivity of the order of the Bessel functions p for the relative error of the Rethorst correction [35]. The relative error is observed to quickly converge below 0.5% at the Bessel function order of $p = 3$. The relative error can also be observed to converge with an increase in the upper limit of Bessel function integration p_{max}. At $p_{max} = 10$, the relative error becomes less than 0.5%. The p_{max} is therefore set to 10 for this analysis.

The odd part of the Rethorst correction, or the odd part of the induced downwash as a result of the jet boundary $\mathbf{G}_{odd}$, is computed for various values of the integration variables $d\lambda$ and $d(\lambda\beta)$. The considered range of the integration variables $d\lambda$ and $d(\lambda\beta) = 0.5, 0.1, 0.05, 0.01, 0.005, 0.001$. The $\mathbf{G}_{odd}$ and computational time are obtained for each of the mentioned evaluation point. The maximum error ε_{max} is defined as the maximum absolute difference between the computed $\mathbf{G}_{odd}$ at a particular $d\lambda$, $d(\lambda\beta)$, normalized with the maximum value in $\mathbf{G}_{odd}$ computed at the lowest tested step size $d\lambda, d(\lambda\beta) = 0.001$.

Figure 3.16 and 3.17 show ε_{max} as function of $d\lambda$ and $d(\lambda\beta)$ and the associated computational time t in seconds as a function of $d\lambda$ and $d(\lambda\beta)$ respectively. Note the exponential scale of the computational time in Figure 3.17. It is observed that ε_{max} decreases more quickly when refining $d\lambda$ compared to $d(\lambda\beta)$, while the computational time increases about the same amount for both $d\lambda$ and $d(\lambda\beta)$.

The chosen settings to get below an error of 0.5% by Willemsen for $d\lambda$ and $d(\lambda\beta)$ were 0.1 and 0.005 respectively [56]. In the case of this analysis, these settings result in an $\varepsilon_{max} = 0.0141$ with an approximate computation time of 4.3 seconds. The jet correction in ALIME is evaluated multiple times in a single iteration of the VLM module. In the interest of ALIME, the computational time is required to stay low. The convergence space is inspected to see if the integration variable settings by Willemsen can be further optimized. In the area where $d\lambda$ and $d(\lambda\beta)$ is the most refined ($d\lambda, d(\lambda\beta) \leq 5e-2$), the computational time lies between about 500 to 2900 seconds. This computational time is considered not to be worth the very slight increase in computational accuracy compared to Willemsen's settings. Instead, a $d\lambda$, $d(\lambda\beta)$ combination is sought with the same order computation time as Willemsen. For the combination of $d\lambda = 0.05$ and $d(\lambda\beta) = 0.01$, ε_{max} decreases by about a 33% compared to the error at Willemsen's settings and the computational time goes down to about 3.6 seconds. No other $d\lambda$ and $d(\lambda\beta)$ combination in the evaluated convergence space yields the same or better decrease in both the maximum error and computation time. The point $d\lambda = 0.05$ and $d(\lambda\beta) = 0.01$ is selected for the jet correction integration variables settings in this thesis.

The maximum error and computation time is evaluated for λ_{max} and $(\lambda\beta)_{max}$. It is discovered that the $\mathbf{G}_{odd}$ diverges for any $(\lambda\beta)_{max} > 1$, $(\lambda\beta)_{max}$ is therefore always kept at 1. The ε_{max} and computational time is computed for every integer value between $1 \leq \lambda_{max} \leq 25$. Figure 3.18 and 3.19 present the ε_{max} and computational time respectively, at $(\lambda\beta)_{max} = 1$. The ε_{max} converges almost completely at $\lambda_{max} = 15$. The computation time increases roughly linearly with λ_{max}. The λ_{max} is set to 15 for this thesis.

3.3. Validation

This section focuses on comparing the ALIME predictions of the lift distribution, lift coefficient and propulsion effects with data from wind tunnel experiments. This is done using wind tunnel data PROWIM wing-propeller geometry and flight test data for the Fokker 50 [12].

The PROWIM wing-propeller combination is used as the reference case in this section. PROWIM is used for various studies on wing-propeller interaction effects. Veldhuis used PROWIM to validate the VLM model used in his Doctoral thesis [54]. Sinnige conducted wind tunnel experiments to investigate and compare the conventional IBpropeller and WTMP configuration of PROWIM [47]. Veldhuis and Sinige used different wing geometries and different PROWIM propeller operation settings, but both studies are used for the validation of ALIME in this section.

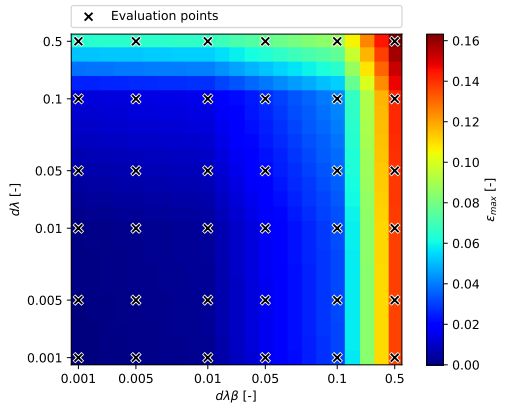

Figure 3.16: The maximum error ε_{max} in the odd part of the Rethorst correction $\mathbf{G}_{odd}$ as a function of the integration variables step sizes $d\lambda$ and $d(\lambda\beta)$, for $\lambda_{max} = 5$ and $(\lambda\beta)_{max} = 1$.

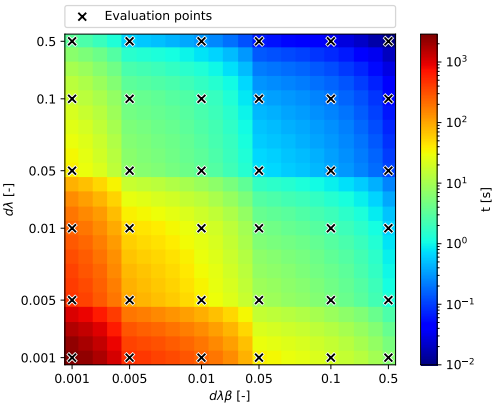

Figure 3.17: The computation time t of the Rethorst correction $\mathbf{G}$ as a function of the integration variables step sizes $d\lambda$ and $d(\lambda\beta)$, for $\lambda_{max} = 5$ and $(\lambda\beta)_{max} = 1$.

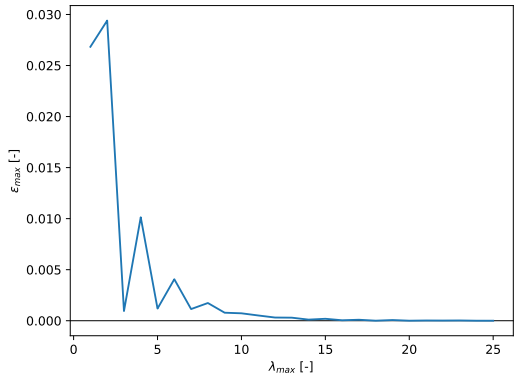

Figure 3.18: The maximum error ε_{max} in the odd part of the Rethorst correction $\mathbf{G}_{odd}$ as a function of the maximum integration variables values $d\lambda_{max}$, for $(\lambda\beta)_{max} = 1$, $d\lambda = 0.05$ and $d(\lambda\beta) = 0.01$.

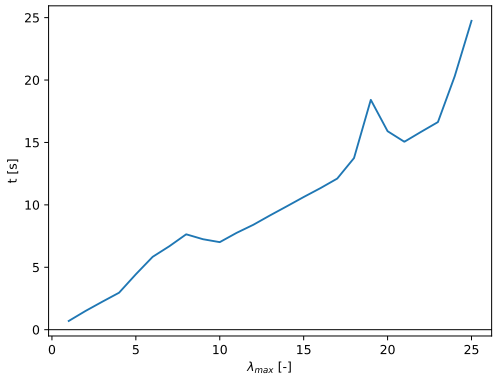

Figure 3.19: The computation time t of the Rethorst correction $\mathbf{G}$ as a function of the maximum integration variables values $d\lambda_{max}$, for $(\lambda\beta)_{max} = 1$, $d\lambda = 0.05$ and $d(\lambda\beta) = 0.01$.

Section 3.3.1 deals with the validation of the PROWIM propeller model in ALIME. The wing lift distribution of the PROWIM wing-propeller combination is discussed in subsection 3.3.3, followed by the lift curve in subsection 3.3.4. Lastly, the F-27 lift distributions are covered in subsection 3.3.5.

3.3.1. PROWIM Isolated Propeller

This section aims to verify the PROWIM isolated propeller performance, the geometry of which is completely described by Sinnige [47]. Experimental data from both Velduis and Sinnige is used in this validation section, therefore both propeller operating points used by Veldhuis and Sinnige are validation for the isolated propeller.

Veldhuis operates the PROWIM propeller between $0.8 < J < 1.2$, with a propeller pitch setting of $\beta_p = 25°$ at 75% R_p and with an IU rotation direction. Only thrust coefficient data, defined as:

$$T_c = \frac{T}{\rho V_\infty^2 D_p^2},$$

is available for the validation of the propeller operating point by Veldhuis. The thrust coefficients T_c are presented in Figure 3.20. The T_c agrees quite well with the validation data, but ALIME slightly underestimates the thrust coefficients around $0.8 < J < 1.0$. Veldhuis does not provide data on the torque coefficients and propeller efficiency.

Sinnige considers the PROWIM propeller at the operating point $0.6 < J < 1.1$, with a propeller pitch setting

of $\beta_p = 23.9°$ at 75% R_p and an IU rotation direction. Willemsen also used this data to validate the isolated propeller calculations for his version of the ALIME. Willemsen's PROWIM propeller model is unfortunately not passed down with ALIME, so a new PROWIM propeller model is to be created for this thesis. The current PROWIM propeller model performance is validated against the PROWIM propeller performance curves by Willemsen and the experimental data by Sinnige. Figure 3.21 shows the thrust coefficients C_T, defined as:

$$C_T = \frac{T}{\rho_\infty n^2 D_p^4},$$

of the PROWIM propeller. Just like for Willemsen's PROWIM model, the ALIME BEM model overestimates the C_T and C_P at $\beta_p = 23.9°$. Willemsen adapted the propeller pitch to obtain a model performance closer to the experimental data. The same thing is done for the ALIME BEM PROWIM model. The overall agreement of the ALIME PROWIM C_T is not bad, but Willemsen's model for PROWIM obtains slightly closer results for C_T relative to the experimental data. In terms of the power coefficients C_P, defined as:

$$C_P = \frac{P}{\rho_\infty n^3 D_p^5},$$

shown in Figure 3.22, ALIME obtains more accurate results compared to Willemsen. The propeller efficiency, displayed in Figure 3.23 η is predicted better by Willemsen's model. The propeller efficiency η is a function of C_T and C_P, prediction for C_T and C_P that more closely match experimentation data will thus result in η results that more closely match experimental data. For the validation cases which considered the propeller operating point by Sinnige, the advance ratio of $J = 0.7$ is used. The PROWIM propeller model by ALIME predicts the propeller model accurately at $J = 0.7$. In conclusion, Willemsen's PROWIM model is more suitable for the higher tested advance ratio range, while the ALIME BEM model is more suitable for the lower tested range of advance ratios.

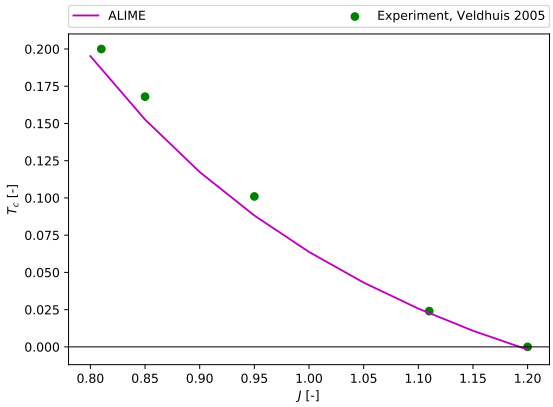

Figure 3.20: The PROWIM propeller thrust coefficient T_c performance as predicted by ALIME compared to the experimental data by Veldhuis [54] at $\alpha_p = 0°$ and $\beta_p = 25°$.

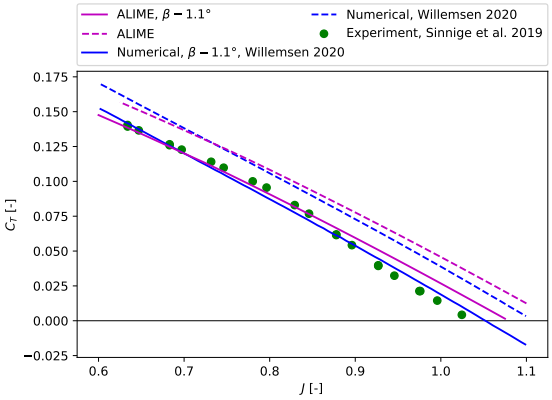

Figure 3.21: The PROWIM propeller thrust coefficient C_T performance as predicted by ALIME compared to the model by Willemsen [56] and the experimental data by Sinnige [47, 48] at $\alpha_p = -0.2°$ and $\beta_p = 23.9°$

3.3.2. Isolated Propeller at an AoA

A non-uniform inflow to the propeller disk changes the propeller's performance. The propeller disk experiencing a non-zero AoA is a form of non-uniform inflow [59]. ALIME models this change in propeller performance by means of the non-uniform propeller inflow developed by van Arnhem as discussed in subsection 2.1.3. This sections aims to compare the performance of the ALIME PROWIM propeller model to the model by Willemsen at a non-zero AoA in an effort to discover how the changes observed in PROWIM propeller model performance in subsection 3.3.1 affected the propeller performance at a non-zero propeller disk AoA α_p.

The isolated PROWIM propeller is tested in the wind tunnel by Sinnige for the propeller AoA range of $-0.2° < \alpha_p < 19.8°$ at various J operating points [47, 48]. Willemsen considered the operating points at $J = 0.7$ and 1.0 for the validation analysis. The same operating points are obtained for the pitch correction ($\beta - 1.1°$)

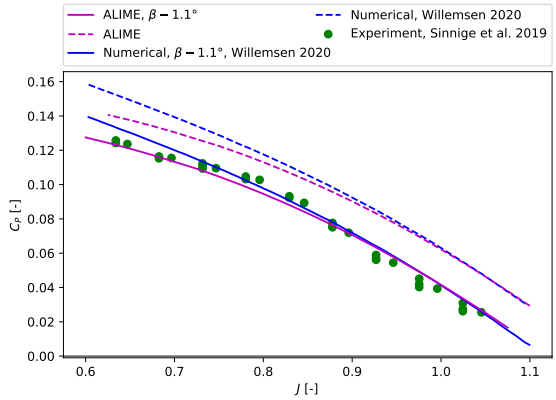

Figure 3.22: The PROWIM propeller power coefficient C_P performance as predicted by ALIME compared to the model by Willemsen [56] and the experimental data by Sinnige [47, 48] at $\alpha_p = -0.2°$ and $\beta_p = 23.9°$

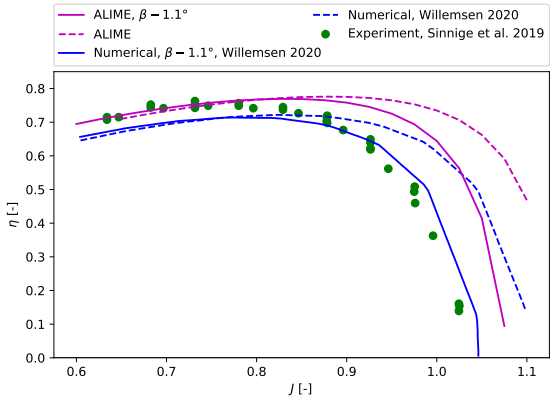

Figure 3.23: The PROWIM propeller thrust coefficient C_T performance as predicted by ALIME compared to the model by Willemsen [56] and the experimental data by Sinnige [47, 48] at $\alpha_p = -0.2°$ and $\beta_p = 23.9°$.

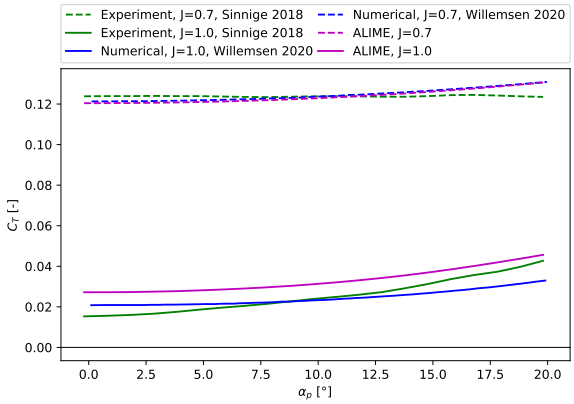

Figure 3.24: A comparison on the effect of AoA on the isolated PROWIM propeller thrust coefficient C_T for between ALIME, Willemsen and experimental data by Sinnige [47].

PROWIM propeller model in ALIME, with the settings described in subsection 3.3.1. The thrust coefficient, obtained from the quasi-steady model, are plotted for the mentioned α_p range in Figure 3.24. Both the quasi-steady and unsteady non-uniform inflow analysis result in the same thrust and torque coefficient results [9]. For the operating point of $J = 0.7$, the C_T result by ALIME agree well with the results by Willemsen. Indicating that the non-uniform inflow propeller analysis still works as intended. At the operating point of $J = 1.0$, the thrust coefficient curve by ALIME is vertically shifted from the results by Willemsen. This veritical shift is present as a result of the difference in PROWIM propeller model C_T that is observed in Figure 3.21 at $\alpha_p = -0.2°$.

3.3.3. PROWIM Lift Distribution

The PROWIM wing-propeller combination is modeled with ALIME and the lift distribution with and without the jet correction applied is determined at an AoA of $\alpha = 0°, 4°$ and $8°$. The results of ALIME are compared with wind tunnel measuremnts by Veldhuis, where the propeller operates under the same experimental conditions as described in subsection 3.3.1. The PROWIM wing-propeller model by van Wonderen is also included for comparison since data by van Wonderen is used later to validate the F-27 model lift distribution. The goal is to investigate the effect of the jet correction on the wing lift distribution of a wing-propeller system at various AoAs. The lift distribution at each of the mentioned three AoAs is first discussed. Afterwards, explanations to the results are given. Figure 3.25 shows the lift distribution of the PROWIM wing-propeller at $\alpha = 0°$. The ALIME overestimates the magnitude of the sectional lift coefficients C_l of the wind tunnel experiment. The jet correction can also be observed to barely affect the C_l at $\alpha = 0°$. To verify that the jet correction is functioning

correctly, the same PROWIM wing-propeller configuration is ran with the latest version of the tool by van der Leer, with and without applying the jet correction. The results of van der Leer's version of the tool and ALIME are identical. The jet correction barely affects the lift distribution at $\alpha = 0°$. Figure 3.26 presents the C_l distribution of the PROWIM wing-propeller system at $\alpha = 4°$. The IB part of the C_l distribution of ALIME and the VLM by Veldhuis agree well with the wind tunnel data, while the model of van Wonderen underestimates the C_l. The peaks in lift distribution as a result of the up and down going propeller blades are again overestimated by ALIME when applying the jet correction. This was again confirmed by checking the lift distribution as predicted with the version of the tool by van der Leer. The results for van der Leer's version and ALIME are again identical. Van Wonderen and Veldhuis predict the lift distribution more closely to the wind tunnel data within the confines of the propeller diameter with respect to ALIME with the jet correction. Both van Wonderen and ALIME underestimate the lift on the OB section of the wing, while Veldhuis' VLM predictions are close to the wind tunnel data. For the lift distribution at $\alpha = 8°$ in Figure 3.27, the observations are very similar compared to the other considered AoAs.

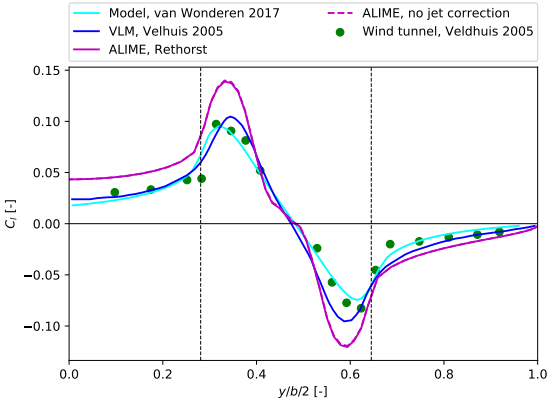

Figure 3.25: Validation of the PROWIM wing-propeller combination configuration with and without the application of the jet correction as compared to the model by van Wonderen [57], the VLM model and wind tunnel data by Veldhuis [54] at $\alpha = 0°$, $J = 0.85$, $\beta_p = 25°$ and $i_p = 0°$.

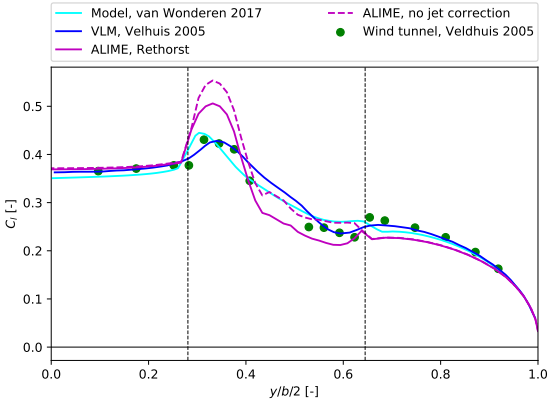

Figure 3.26: Validation of the PROWIM wing-propeller combination configuration with and without the application of the jet correction as compared to the model by van Wonderen [57], the VLM model and wind tunnel data by Veldhuis [54] at $\alpha = 4°$, $J = 0.85$, $\beta_p = 25°$ and $i_p = 0°$.

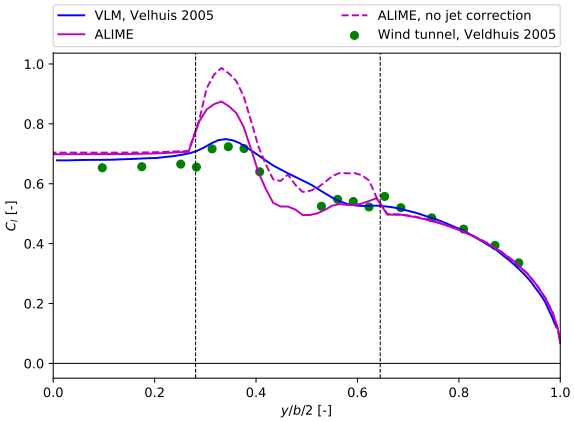

Figure 3.27: Validation of the PROWIM wing-propeller combination configuration with and without the application of the jet correction as compared to the model by van Wonderen [57], the VLM model and wind tunnel data by Veldhuis [54] at $\alpha = 8°$, $J = 0.85$, $\beta_p = 25°$ and $i_p = 0°$.

The overestimation of the lift distribution peaks due to the propellers has two explanations. The first and main explanation is the jet correction not correcting for the swirl component in the flow of the propeller slipstream and no SRF is used in ALIME. Nederlof found that not taking into account this swirl flow component in the jet correction results in an overestimation of the sectional lift coefficient peaks as a result of the up and

down going propeller blades [35]. The lift distributions peaks due to the propellers are thus always overestimated as long as a swirl component is present in the jet, the jet correction by Rethorst and Prabhu is applied and no SRF is included. The possible second explanation for the overestimation of the lift distribution peaks are the torque coefficient of the propeller. The torque coefficients in the propeller directly influence the local AoA which the propeller slipstream swirl component induces onto the wing, which influences the peaks in the lift distribution [39]. The PROWIM propeller operates in the operating point of Veldhuis, for which no validation of the troque or power coefficient of the propeller could be performed because of the absence of validation data. Uncertainty in the correct modeling of the propeller torque coefficient at $J = 0.85$ this results in uncertainly in the modeling of the lift distribution component due to the propeller swirl.

The average percentile difference between the section lift coefficient by ALIME with and without the jet correction applied is determined. At $\alpha = 0°$, the percentile change in lift distribution as a result of the jet correction is about half a percent, while at $\alpha = 4°$ and 8° it is about 6%. The jet correction affects the sectional lift coefficient as a function of AoA.

3.3.4. PROWIM Lift Curve

The contribution of the jet correction to the lift coefficient C_L and its slope C_{L_α} is quantified in this section. The PROWIM wing-propeller system is analyzed by ALIME over the AoA range of $-4° \leq \alpha \leq 6°$ and the propeller operates at $J = 0.7$.

Figure 3.28 presents the lift curve of the PROWIM wing-propeller combination as predicted by ALIME, including the propeller forces contributions, and the wind tunnel test results of the wing-propeller-nacelle PROWIM model by Sinnige. The lift curves for propellers off and propellers on with and without the application of the jet correction are presented. To ease the comparison, the lift curve slopes C_{L_α} of each lift curve are determined and presented in Table 3.1. The C_{L_α} for ALIME are taken as the slope of the linear line between the C_L at and AoA of -4° and 6°. The wind tunnel lift curve slopes are obtained by fitting a first degree polynomial through the data. The error ε is determined by subtracting the ALIME C_{L_α} from the wind tunnel results and dividing by the wind tunnel result.

The propellers off C_{L_α} is predicted with an error in the order of a few percent, although the C_L is overestimated by a constant ΔC_L, which shifts all the ALIME results up vertically compared to the wind tunnel data. The ΔC_L is thought to originate from the absense of the modeling of the propeller nacelle in ALIME. Willemsen performed a validation for the WTMP variant of the PROWIM wing-propeller combination, where the effect of the nacelle on the props off lift is modeled by means of slightly expending the wing span, which is not possible for the IB propeller case in this section.

The propellers on lift curve by ALIME is shifted up vertically with respect to the propellers off curve, because of the extra dynamics pressure of the propeller blowing over the wing. With the propellers on and without the jet correction, ALIME predicts the C_{L_α} to increase, but still underestimates it with about 4%. In the case where the jet correction is applied, the lift curve slope is about 8% lower compared to the jet correction not being applied. This makes sense, since the jet correction is found to increasingly lower the C_L magnitude with AoA when investigating the lift distribution in subsection 3.3.3.

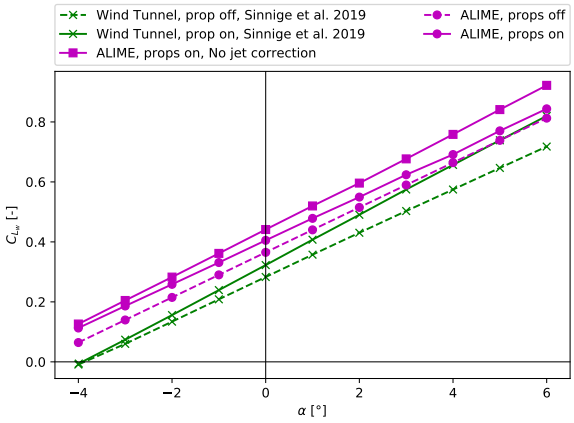

Figure 3.28: The lift curve of the PROWIM wing-propeller system as predicted by ALIME at $J = 0.7$, compared to wind tunnel data by Sinnige *et al.* [48]

Table 3.1: The C_{L_α} and ε of the PROWIM wing-propeller model as predicted by ALIME with and without the propeller jet correction at $J = 0.7$, compared to wind tunnel data by Sinnige *et al.* [48].

	Wind tunnel	With propeller jet correction		Without propeller jet correction	
	C_{L_α} [1/°]	C_{L_α} [1/°]	ε [%]	C_{L_α} [1/°]	ε [%]
Props off	0.07308	0.07482	2.4	0.07482	2.4
Props on	0.08303	0.07309	-12.0	0.07958	-4.2

3.3.5. F-27 Lift Distribution

This section deals with the validation of the lift distributions of the F-27 NLL model, the geometry of which is described in Appendix A. The aim is to investigate the consequences of not modeling the fuselage and nacelle carry over effect on the wing lift. This is done by means of a comparison to other F-27 models that do model this carry over effect for the F-27. In addition, the implementation for the co-rotating propellers is verified in this section, by considering the wing lift distribution of the F-27 with propellers. The propeller model used for the F-27 in this thesis is described in Appendix B.

The lift distributions for the F-27 by ALIME are compared to flight test data in this section. The flight test by van den Borne and van Hengst is obtained by measurement taken in two flight conditions, a LTC and HTC. Table 3.2 contains the details on the two conditions. The thrust coefficient used by van den Borne and van Hengst T_c' uses the propeller disk area S_p to normalize the thrust:

$$T_c' = \frac{T}{q_\infty S_p} = \frac{T}{q_\infty \frac{\pi}{4} D_p^2}.$$

The pitch β_p of the propeller model described in Appendix B is adapted to 36.560° and 32.186° to match the T_c' of the LTC and HTC conditions respectively.

Table 3.2: The details of the LTC and HTC test cases for the F-27 NLL model lift distribution validation.

Condition	α [°]	T_c' [-]	J [-]
LTC	-0.2	0.11	1.63
HTC	6.1	0.63	1.0

First, the lift distribution without propellers is discussed. Then, the propeller is introduced and the resulting lift distributions are covered.

Propellers Off

The wing lift distribution C_{l_w} of the F-27 NLL model by ALIME for the LTC and HTC without the propellers are presented in Figure 3.29 and 3.30, together with the flight test data by van den Borne and van Hengst [12] and the two other VLM models. These are the VLM models by Veldhuis [54] and van Wonderen [57]. Both Veldhuis and van Wonderen model the fuselage and nacelle carry over effect, while ALIME does not as explained in chapter 1.

The carry over effect does affect the lift distribution. The flight test data does agrees more with the lift distributions of the models that include the carry over effect of the fuselage and nacelles. The downwash of the horizontal stabilizer in ALIME should therefore be different compared to the other two VLM models. The effect of not modeling the carry over effect on the wing lift coefficient cannot be investigated in this section. The analysis on the F-27 without propellers is presented in Chapter 4 will point out how much this effects the lift coefficient. Do note that the main goals of this thesis is not to obtain close predictions for the lift and moment coefficient of the main wing, but the information in this section is an important building block for the discussion on the downwash experienced by the horizontal stabilizer.

Propellers On

To verify the implementation of the co-rotating propellers, the C_{l_w} distribution with propellers for the LTC and HTC are considered. Figure 3.31 and 3.32 show C_{l_w} for LTC and HTC respectively.

The lift peaks directions predicted by ALIME corresponding to the up and down going blades of the F-27's CCW rotating propellers (as seen from the front) agree with the propeller lift peaks of Veldhuis' VLM model,

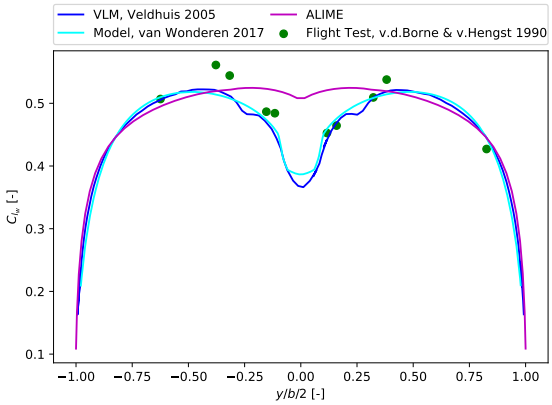

Figure 3.29: The F-27 NLL lift distribution as predicted by the ALIME at the LTC without propellers, compared to van Wonderen [57], Veldhuis [54] and flight test data [12].

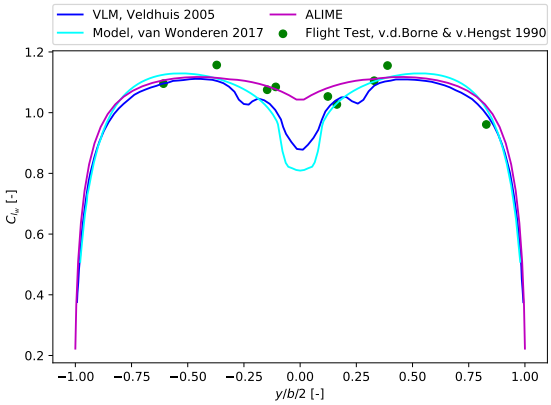

Figure 3.30: The F-27 NLL lift distribution as predicted by the ALIME at the HTC without propellers, compared to van Wonderen [57], Veldhuis [54] and flight test data [12].

showing that the propeller CCW rotation direction is implemented correctly. Just like for the PROWIM lift distributions, the propeller lift peaks overestimate the local sectional lift. This is because no SRF is implemented. Similarly for the PROWIM case, uncertainty in the torque performance of the F-27 BEM model, as mentioned as well in Appendix B, might too contribute to the overestimation of the sectional propeller lift peaks for the F-27. However, this overestimation should not affect the wing lift coefficient and average downwash at the stabilizer much, since the overestimated lift peaks of the up and down going propeller blade cancel each other out.

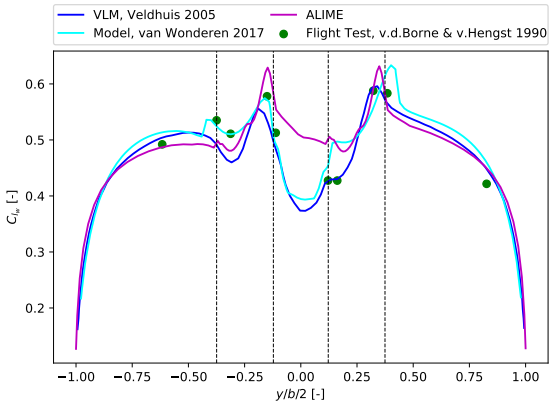

Figure 3.31: The F-27 NLL lift distribution C_{l_w} as predicted by the ALIME with the application of the jet correction at the LTC with propellers, compared to van Wonderen [57], Veldhuis [54] and flight test data [12].

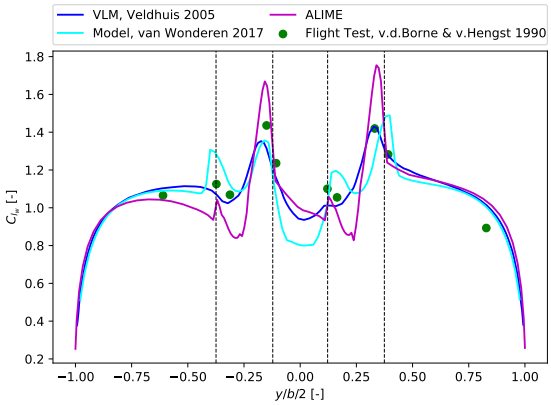

Figure 3.32: The F-27 NLL lift distribution C_{l_w} as predicted by the ALIME with the application of the jet correction at the HTC with propellers, compared to van Wonderen [57], Veldhuis [54] and flight test data [12].

4

Fokker F-27 Case Study

This chapter describes the case study performed on the Fokker F-27 using ALIME, with the ultimate goal of answering the research questions. The analysis is split up in a propellers off and on analysis. With the propellers off analysis serving as the foundation for the propellers on analysis. Both the F-27 models by TU Delft and NLL are considered for these analyses, which are described in Appendix A. It is specified in every section what F-27 model is utilized. The propeller model used during the propellers on analysis is described in Appendix B.

Before the propellers off and on analyses are covered, the fuselage and nacelle correction for the F-27 is described in section 4.1. The propeller off analysis is covered in section 4.2 and the propellers on analysis is presented in section 4.3.

4.1. Fuselage and Nacelle Correction

As the name of the model in this thesis project suggests, ALIME, the fuselage and nacelle are not modeled. However, the fuselage and nacelles do affect the moment coefficient and thus the LSS of an aircraft [44, 32, 21]. The fuselage and nacelle contributions are added as a correction to the results by ALIME, to be able to take these into account of the moment coefficient without actually modeling them. This section explains how this is done.

The method for determining the fuselage and nacelles contribution to the aircraft moment coefficient is based on the work by Munk [33] and Multhopp [32] and is fully described by sources such as Roskam and Nelson [43, 36]. The method involves a semi-empirical calculation including geometry sections of the fuselage and nacelle bodies. The method has been applied many times in literature and successfully represents the contributions of the fuselage and nacelles [36]. Van der Vaart and Muhammad performed simple handbook method calculations on the F-27 to predict the moment coefficient of the WFN combination, isolated horizontal stabilizer and complete airplane, which agree well with wind tunnel data [53].

For the purpose of this thesis, the fuselage and nacelle correction for the F-27 by van der Vaart and Muhammad is directly applied to the ALIME results of the isolated wing and wing-stabilizer combination without propellers, to obtain predictions for the WFN combination configuration and complete aircraft. It is assumed that the fuselage and nacelles do not influence the moment contribution of the horizontal stabilizer and that the fuselage and nacelle lift is negligible compared to the wing lift: $C_{L_{wfn}} \approx C_{L_w}$ [53].

A derivation shows how the fuselage and nacelle correction by van der Vaart and Muhammad is applied to the F-27 results by ALIME for the isolated wing and wing-stabilizer configurations. The moment coefficient contribution for a WFN combination of an aircraft without propellers can be expressed as [53, 39]:

$$C_{M_{wfn}} = C_{M_{a.c._{wfn}}} + C_{L_w} \frac{x_{ref} - x_{a.c._{wfn}}}{\bar{c}}.$$

The fuselage and nacelle correction used by van der Vaart and Muhammad states that the fuselage and nacelle contribute to the a.c. moment of the aircraft and the overall a.c. position of the aircraft. The WFN a.c. moment contribution can be taken to be a sum of the isolated wing and fuselage-nacelle components: $C_{M_{a.c._{wfn}}} = C_{M_{a.c._w}} + \Delta C_{M_{a.c._{fn}}}$. The same is true for the a.c. position: $x_{a.c._{wfn}} = x_{a.c._w} + \Delta x_{a.c._{fn}}$ [53]. This $\Delta C_{M_{a.c._{fn}}}$

and $\Delta x_{a.c._{fn}}$ are calculated using the semi-empirical calculation [53]. Substituting these expressions in to the WFN moment contribution yields:

$$C_{M_{wfn}} = \left(C_{M_{a.c._w}} + \Delta C_{M_{a.c._{fn}}}\right) + C_{L_w} \frac{x_{ref} - \left(x_{a.c._w} + \Delta x_{a.c._{fn}}\right)}{\bar{c}}.$$

When rearranging the terms:

$$C_{M_{wfn}} = \Delta C_{M_{a.c._{fn}}} + C_{M_{a.c._w}} + C_{L_w} \frac{x_{ref} - x_{a.c._w}}{\bar{c}} - C_{L_w} \frac{\Delta x_{a.c._{fn}}}{\bar{c}}.$$

The terms that contain the Δ are part of the fuselage and nacelle correction by van der Vaart and Muhammad. To indicate what entries are calculated using semi-empirical method, they are given the superscript $calc$. The left over terms are what the ALIME numerically calculates when analyzing an isolated wing using Equation 2.36. These terms are therefore combined into $C^{num}_{M_w}$, where the superscript num indicates that this quantify is determined with ALIME. Equation 4.1 shows that fuselage and nacelle contributions in $C_{M_{wfn}}$ can be added to the isolated wing results by ALIME by means of adding two terms, one representing the contribution of the Fuselage-Nacelle (FN) to a.c. moment and the a.c. position.

$$C_{M_{wfn}} = \Delta C^{calc}_{M_{a.c._{fn}}} + C^{num}_{M_w} - C^{calc}_{L_w} \frac{\Delta x^{calc}_{a.c._{fn}}}{\bar{c}} \tag{4.1}$$

A similar analysis can be done for the complete aircraft without propellers, which moment contribution can be expressed as [53, 39]:

$$C_{M_{wfnh}} = C_{M_{a.c._{wfn}}} + C_{L_w} \frac{x_{ref} - x_{a.c._{wfn}}}{\bar{c}} + C_{L_{h_\alpha}} (\alpha - \varepsilon + i_h) \frac{q_h S_h}{q_w S_w} \frac{l_h}{\bar{c}}.$$

Where $l_h = x_{ref} - x_{a.c._h}$. When substituting $C_{M_{a.c._{wfn}}} = C_{M_{a.c._w}} + \Delta C_{M_{a.c._{fn}}}$ and $x_{a.c._{wfn}} = x_{a.c._w} + \Delta x_{a.c._{fn}}$, rearranging the terms and realizing that all terms apart from the Δ terms are determined numerically by ALIME, one finds Equation 4.2 for the fuselage and nacelle moment correction for the complete airplane, which is very similar to the FN correction for the WFN configuration.

$$C_{M_{wfnh}} = \Delta C^{calc}_{M_{a.c._{fn}}} + C^{num}_{M_{wh}} - C^{calc}_{L_w} \frac{\Delta x^{calc}_{a.c._{fn}}}{\bar{c}} \tag{4.2}$$

The lift of the wing as calculated by van der Vaart and Muhammad, $C^{calc}_{L_w}$, is calculated using:

$$C^{calc}_{L_w} = C^{calc}_{L_{w\alpha}} \left(\alpha - \alpha^{calc}_{C_{L_w}=0}\right),$$

where $C^{calc}_{L_{w\alpha}}$ and $\alpha^{calc}_{C_{L_w}=0}$ are calculated to be 0.1001 1/° and -2° for the F-27 TU Delft model respectively. The $\Delta C^{calc}_{M_{a.c._{fn}}}$ and $\Delta x^{calc}_{a.c._{fn}}$ are calculated to be equal to -0.079 and -0.139 respectively [53].

4.2. Propeller Off Analysis

This section has four goals. Firstly, to verify the geometry of the F-27 models as well as their moment reference point. Secondly, to verify the fuselage and nacelle correction, which is described in section 4.1, applied to the F-27 results by ALIME. Thirdly, to compare the F-27 results of the F-27 TU Delft model results to the calculations by van der Vaart and Muhammad. Lastly, to compare the ALIME results to wind tunnel data and assess ALIME's ability to model the F-27 moment coefficient and LSS without propellers and see the influence of neglecting the fuselage and nacelle carry over effect on the lift and moment coefficients. These results are used as a basis for when the propellers are added later in this chapter. The results for the F-27 TU Delft model and the NLL model are covered in subsection 4.2.1 and 4.2.2 respectively.

4.2.1. F-27 TU Delft Model

The F-27 TU Delft model is ran for the AoA range of $-1.54° \leq \alpha \leq 8.46°$, in intervals of 1°. The moment reference point is set at $x_{ref} = 0.346\bar{c}$. Van der Vaart and Muhammad provide a schematic showing the exact

location of the reference point with respect to the wing LE, allowing for an exact determination of the moment reference point position [53]. Note that for the calculation of the moment coefficient, the axial panel forces are not taken into account. These contributions are neglected as a result of the discussion in subsection 3.1.2. This means that the z_{ref} does not have to be considered. The geometry of the F-27 model by TU Delft is described in Appendix A. The aircraft moment coefficient is split into two contributions, the WFN combination and horizontal stabilizer. These contributions are covered in their respective section before the complete aircraft lift and moment are covered. For each considered configuration of the model, the lift and moment coefficient curves are presented.

WFN Contribution

The F-27 isolated wing lift coefficient C_{L_w} is shown in Figure 4.1. The lift curve by ALIME lies in between the calculated lift curve by van der Vaart and Muhammad and the wind tunnel data by Spigt and de Gelder. The lift curve by ALIME agrees very well with the wind tunnel data in the upper range of the considered AoAs. The overall slope of the ALIME lift curve appears to be lower when compared to the calculated and the wind tunnel data.

Figure 4.2 contains the moment coefficient C_{L_w} curve of the isolated F-27 TU Delft model wing. The slope of the moment coefficient curve is higher compared to the calculated and wind tunnel data. The underestimated lift coefficient slope is to blame for this, since the moment coefficient slope is a function of the lift coefficient slope.

Now the WFN combination is considered, Figure 4.3 contains the WFN moment coefficient $C_{L_{wfn}}$ curve. The $C_{L_{wfn}}$ contain the fuselage and nacelle correction on to of the isolated wing results by ALIME. Now, the calculated moment coefficient curve underestimated the slope of the wind tunnel data, while the fuselage and nacelle corrected ALIME result slightly overestimate it. Overall, the calculated data seems to predict the isolated wing and WFN moment slightly better compared to ALIME.

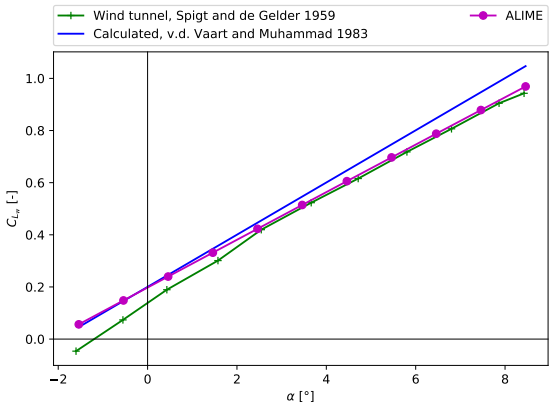

Figure 4.1: The isolated wing lift coefficient C_{L_w} curve of the F-27 TU Delft model by ALIME, compared to the calculated data by van der Vaart and Muhammad [53] and the wind tunnel data by Spigt and de Gelder [49].

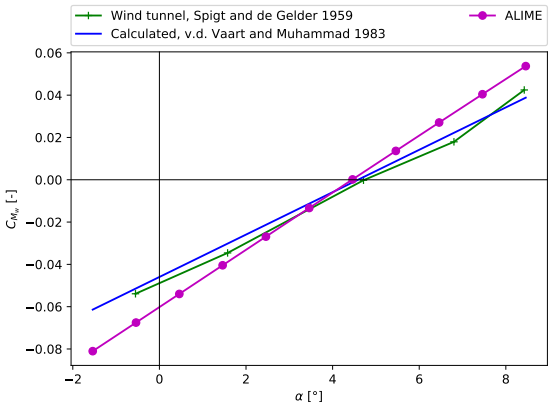

Figure 4.2: The isolated wing moment coefficient C_{M_w} curve of the F-27 TU Delft model by ALIME, compared to the calculated data by van der Vaart and Muhammad [53] and the wind tunnel data by Spigt and de Gelder [49].

Stabilizer Contribution

The lift contribution of the horizontal stabilizer C_{L_h} is presented in Figure 4.4. Wind tunnel data is obtained for the horizontal stabilizer lift contribution by taking the lift coefficient data of the complete aircraft and subtracting the lift coefficient data of the aircraft without the stabilizing surfaces by Binkhorst and Spoon [11]. This yields the moment coefficient contribution of the horizontal and vertical stabilizer, where the longitudinal moment contribution of the vertical stabilizer is assumed to be negligible compared to the horizontal stabilizer contribution. The interactions between the fuselage and the stabilizing surfaces is neglected. ALIME predicts the lift of the horizontal stabilizer well, meaning that the downwash angle experienced by the horizontal stabilizer is captured well. The calculated data underestimates the lift generated by the horizontal stabilizer.

The moment coefficient curve of the horizontal stabilizer C_{M_h} is presented in Figure 4.5. ALIME seems to slightly overestimate the stabilizing moment curve slope contribution of the horizontal stabilizer. The

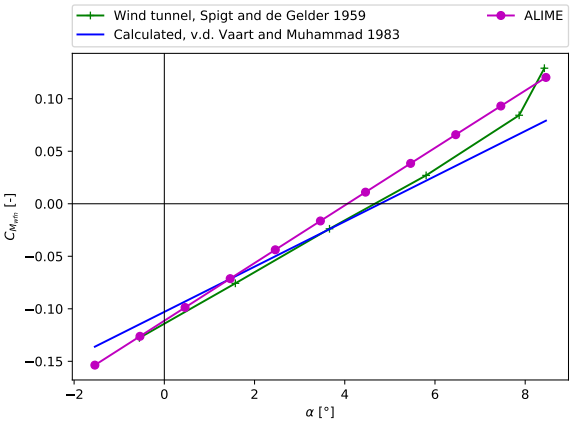

Figure 4.3: The WFN moment coefficient $C_{M_{wfn}}$ curve of the F-27 TU Delft model, including the fuselage and nacelle correction, compared to the calculated data by van der Vaart and Muhammad [53] and the wind tunnel data by Spigt and de Gelder [49].

calculated moment curve appears to have a very similar slope compared to the wind tunnel data, but its curve is vertically shifted. Indicating that the calculated method underdetermined the $C_{M_{a.c.h}}$.

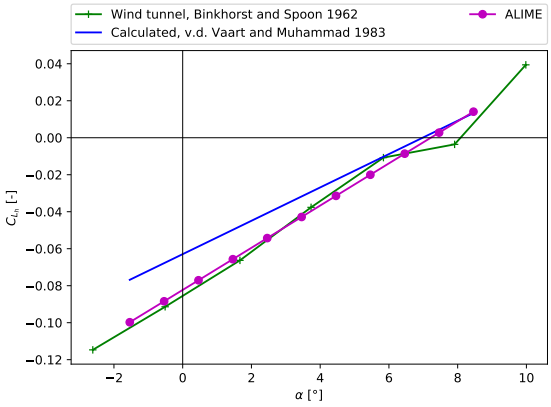

Figure 4.4: The lift coefficient of the F-27 TU Delft model stabilizer C_{L_h}, compared to the calculated data by van der Vaart and Muhammad [53] and the wind tunnel data by Binkhorst and Spoon [11].

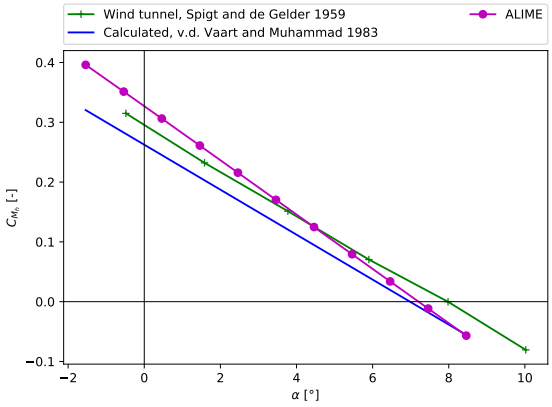

Figure 4.5: The moment coefficient contribution of the F-27 TU Delft model stabilizer C_{M_h}, compared to the calculated data by van der Vaart and Muhammad [53] and the wind tunnel data by Spigt and de Gelder [49].

Complete Aircraft

Figure 4.6 shows the lift coefficient C_L curve of the complete aircraft. The ALIME lift results are essentially the sum of the isolated wing and stabilizer contributions $C_{L_{wh}}$, since the fuselage and nacelles are not assumed to contribute to the lift coefficient as stated before [53]. Just like for the isolated wing, ALIME's lift curve prediction lies in between the calculated and the wind tunnel curve and features a lower lift coefficient slope.

The moment coefficient C_M curve of the entire aircraft in presented in Figure 4.7. For ALIME, the wing-stabilizer moment without the fuselage and nacelle correction $C_{M_{wh}}$ as well as the corrected moment $C_{M_{wfnh}}$ are presented to show the effect of the fuselage and nacelle correction on the entire moment curve. The under and overestimation of the moment curve slope of the isolated wing and horizontal stabilizer respectively seems to have evened out, as the slope of the moment curve (or the LSS) seems to be very close to the wind tunnel data. The $C_{M_{wh}}$ slope is nowhere near close to the wind tunnel data, showing the importance of taking into account the fuselage and nacelle moment coefficient contributions. The calculated LSS also appears to be close to the wind tunnel data. Both ALIME and the calculated results show a vertical shift in terms of the moment curve compared to the wind tunnel curve. ALIME overestimates the aircraft $C_{M_{a.c.}}$, while the calculations underestimate it.

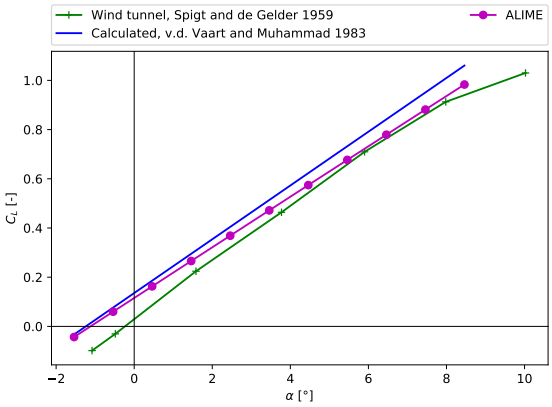

Figure 4.6: The complete lift of the F-27 TU Delft model as compared to the calculated data by van der Vaart and Muhammad [53] and the wind tunnel data by Spigt and de Gelder [49].

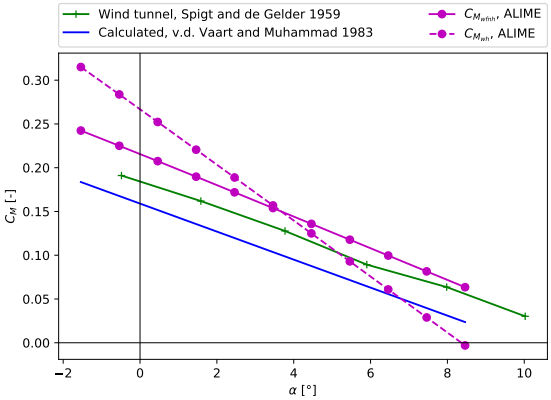

Figure 4.7: The complete moment contribution of the F-27 TU Delft model, with and without the fuselage and nacelle correction, as compared to the calculated data by van der Vaart and Muhammad [53] and the wind tunnel data by Spigt and de Gelder [49].

4.2.2. F-27 NLL Model

The unfortunate thing about the F-27 TU Delft model is the absence of wind tunnel data including propellers on results. The F-27 TU Delft thus merely served as a case to investigate ALIME's ability to predict the lift and moment of a wing-stabilizer combination when a fuselage and nacelle correction is included. However, the main goal of this thesis is to investigate the propulsion effects on the aircraft moment coefficient, this where a second model, the F-27 NLL model, comes in. Various tests are performed in the wind tunnel by NLL with and without the propellers. The F-27 NLL model has a different scale with respect to the TU Delft model and it has some differences in geometry that are important to take note of. These differences in geometry between the TU Delft and NLL F-27 model are highlighted in Appendix A. The propellers off version of the F-27 NLL model is validated against the wind tunnel data by NLL [55] in this subsection in order to confirm the correct implementation of its geometry and moment reference points, before introducing the propellers to the ALIME model later in this chapter.

The NLL uses two locations as the moment reference point, the 30% and 40% chord line on the main wing. The 40% chord line is orthogonal to the aircraft longitudinal axis, the x_{ref} point does therefore not vary with y. The 30% chord line does vary with y due to the taper of the wing. The 30% chord line reference point is used the most to determine the moment by NLL, so the 30% MAC position is taken to be the reference point for the F-27 NLL model. The 30% MAC position is calculated to be located at $x_{ref} = 0.07522m$ from the wing root chord LE. The calculation of x_{ref} consisted of adding 30% of the MAC length to the LE position at the MAC y-coordinate. Just like for the TU Delft model analysis, only the panel normal force contributions are taken into account to determine the moment coefficients.

Visually comparing the slopes of the lift and moment curves is hard when the differences are small. So the lift and moment curve slopes for the F-27 NLL model without propellers are calculated and presented in Table 4.1 to ease the comparison between the ALIME and wind tunnel results. The lift and moment curves by ALIME are linear as a result of the assumed inviscid and potential flow assumption. Making it acceptable to determine the lift and moment slope by subtracting the lift and moment at the highest considered AoA, subtracting the lift and moment at the lowest considered AoA and dividing by the total AoA range. The slopes of the wind tunnel data are obtained by fitting a first degree polynomial through the data and taking the slope of that fitted linear line.

The fuselage and nacelle correction is dependent on the geometry of the fuselage and nacelles of the aircraft. The F-27 NLL model features a slightly longer rear fuselage compared to the TU Delft model, also affecting the position of the horizontal stabilizer. The fuselage and nacelle correction by van der Vaart and Muhammad is performed for the fuselage of the NLL model to investigate effect of the extra fuselage rear length on the calculated values used in the correction. The extra fuselage rear length barely affects the values used in the correction. The $\Delta x_{a.c._{fn}}^{calc}$ changes from 0.139 for the TU Delft model to 0.140 for the NLL model. The latter is used for the NLL fuselage and nacelle correction.

The WFNcontribution, stabilizer contribution and complete aircraft results are again discussed respec-

tively.

WFN Contribution

The lift coefficient $C_{L_{wfn}}$ curve of the F-27 NLL model is presented in Figure 4.8. The lift coefficient and the slope $C_{L_{wfn_\alpha}}$ are both underestimated, the slope by about 9%. The wing lift is overestimated for the F-27 TU Delft model as shown in subsection 4.2.1. The underestimation in lift by ALIME in this case can perhaps be explained by the difference in fuselage geometry between the TU Delft and the NLL F-27 models. The longer fuselage of the F-27 NLL model possibly generated more lift compared to the F-27 TU Delft. Meaning that the assumption of $C_{L_w} \approx C_{L_{wfn}}$ by van der Vaart and Muhammad [53] might not be applicable to the NLL model. In addition, the underestimation of the lift is interesting in the sense that one would expect and overestimation of the lift when not modeling the fuselage and nacelle carry over effect. This can mean that the carry over effect is not a large for F-27 NLL wind tunnel model as the VLM models by Veldhuis and van Wonderen predict in Table 3.3.5. However, the question of the impact on the stabilizer downwash still remains. The stabilizer lift and moment contribution are therefore referred to.

The moment coefficient of the wing and the WFN combination is presented in Figure 4.9. Just like for the F-27 TU Delft model, the $C_{M_{wfn_\alpha}}$ is overestimated, in this case by about 20%.

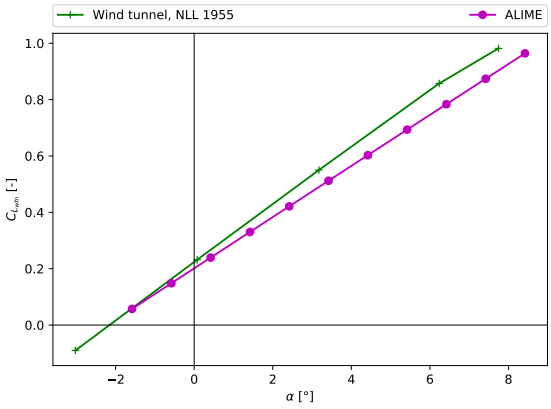

Figure 4.8: The WFN combination lift coefficient $C_{L_{wfn}}$ curve of the F-27 NLL model compared to the wind tunnel data by the NLL [55].

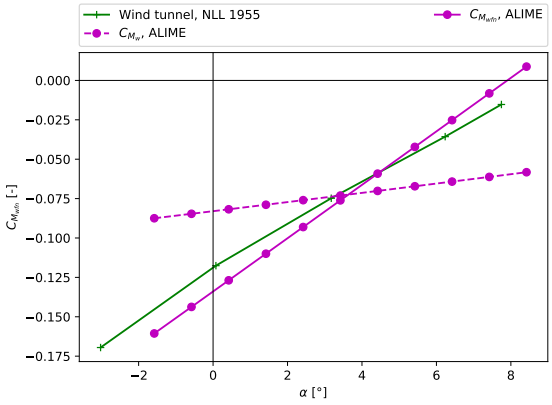

Figure 4.9: The WFN combination moment coefficient $C_{M_{wfn}}$ curve of the F-27 NLL model compared to the wind tunnel data by the NLL [55].

Stabilizer Contribution

The stabilizer lift coefficient C_{L_h} curve is shown in Figure 4.10, which shows that the magnitude of the lift is underestimated. The slope $C_{L_{h_\alpha}}$ is estimated well by ALIME, with an error of less than a percent.

The stabilizer moment coefficient C_{M_h} curve is presented in Figure 4.11. The magnitude of the moment coefficient is also closely estimated by ALIME. The $C_{L_{h_\alpha}}$ is overestimated by about 7% according to Table 4.1. The $C_{L_{h_\alpha}}$ is also overestimated by ALIME for the F-27 TU Delft model.

An overestimation of the stabilizer lift contribution magnitude can point to an underestimation of the downwash at the stabilizer, while the negligence of the carry over effect should result in a lower stabilizer lift magnitude as a results of a higher experienced downwash angle at the stabilizer. Again pointing to the carry over effect possibly not being as large in the wind tunnel conditions. The stabilizer lift slope contribution $C_{L_{\alpha_h}}$ is predicted within 1% as shown in Table 4.1. Regardless, the moment contribution of the stabilizer is closely predicted. Not excluding partial coincidence as a possible explanation for overestimated stabilizer lift prediction, since the stabilizer lift contribution prediction matched well for the F-27 TU Delft model.

Complete Aircraft

The complete aircraft lift C_L curve of the F-27 NLL model predicted by ALIME is compared to wind tunnel data is presented in Figure 4.12. It is no surprise that the lift is underestimated, since the lift of the WFN is underestimated.

The moment coefficient C_M curve of the F-27 NLL model is shown in Figure 4.13. The moment coefficients C_M are well estimated for the NLL model. The slope C_{M_α} is estimated within a few percent of the wind tunnel result.

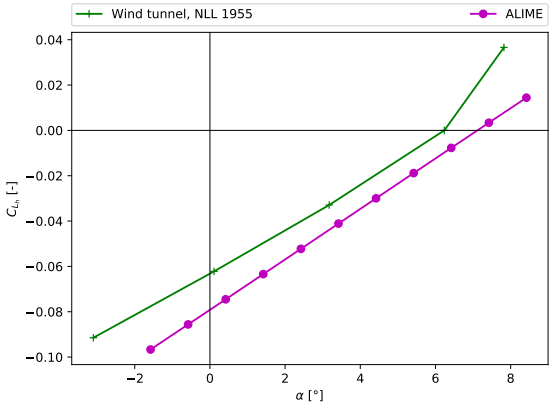

Figure 4.10: The stabilizer lift coefficient C_{L_h} curve of the F-27 NLL model compared to the wind tunnel data by the NLL [55].

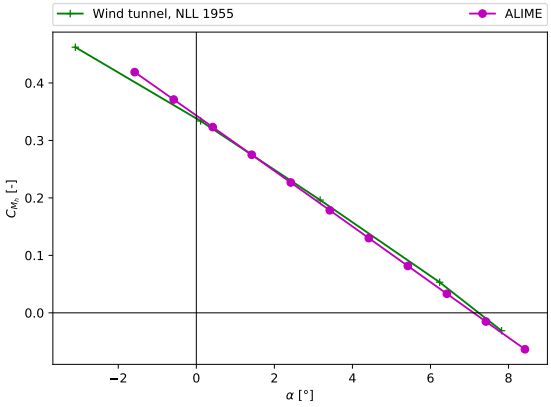

Figure 4.11: The stabilizer moment coefficient C_{M_h} curve of the F-27 NLL model compared to the wind tunnel data by the NLL [55].

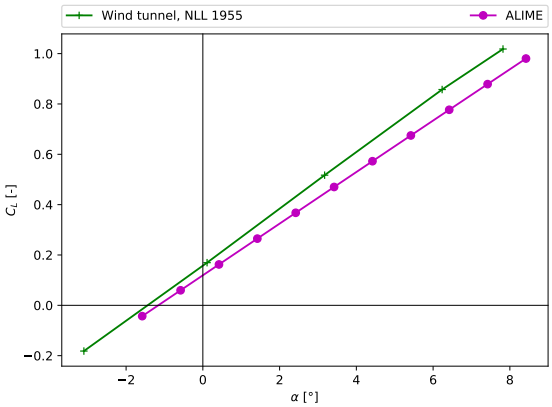

Figure 4.12: The lift coefficient C_L curve of the F-27 NLL model compared to the wind tunnel data by the NLL [55].

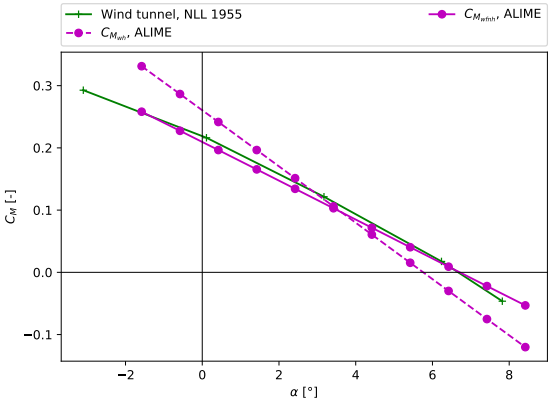

Figure 4.13: The moment coefficient C_M curve of the F-27 NLL model compared to the wind tunnel data by the NLL [55].

Table 4.1: A comparison between the lift and moment slope contributions of the F-27 NLL model by ALIME and the wind tunnel tests by NLL without propellers, where the error is with respect to the wind tunnel values.

	Wind tunnel [1/°]	ALIME [1/°]	Error ε [%]
$C_{L_{w_\alpha}}$	0.10030	0.09123	-9.05
$C_{L_{h_\alpha}}$	0.01118	0.01111	-0.66
C_{L_α}	0.11054	0.10234	-7.42
$C_{M_{wfn\alpha}}$	0.014135	0.017096	20.95
$C_{M_{h_\alpha}}$	-0.045133	-0.048273	6.85
$C_{M_{wfnh_\alpha}}$	-0.031127	-0.029935	-3.83

4.3. F-27 Propellers On Analysis

This section brings all individual building blocks described in this thesis together to analyze the F-27 NLL including the propeller to attempt to answer the research question. The F-27 NLL model is analyzed by ALIME with the propeller model, described in Appendix B, at the propeller setting of $J = 0.67$ with $T_c = 0.4$. The considered AoA range is again taken to be $-1.54° \leq \alpha \leq 8.46°$, but evaluated for only five values of α because of the longer running time of ALIME with the introduction of the propeller. Evaluating one AoA with the jet correction applied takes roughly 1.5 hours until convergence. Convergence occurs in 2 or 3 iterations in these cases.

The available wind tunnel data only allows for a comparison with ALIME for the aircraft lift and moment coefficient. Contrarily to the propellers off case in section 4.2, no individual contribution comparisons are

therefore possible with wind tunnel data of the propellers on analysis. However, the analysis of the F-27 without propellers already serves as a good basis. Note that the fuselage correction is also applied to the moment coefficient in this section.

Section 4.3.1 evaluates the lift, moment and LSS performance of the F-27 NLL model with the propeller. The flow field at the stabilizer, more specifically, the average downwash and dynamic pressure at the stabilizer is discussed are subsection 4.3.3 and 4.3.2 respectively.

4.3.1. Total Lift, Moment Coefficient and LSS

The aircraft lift coefficient C_L and aircraft moment coefficient C_M for the F-27 NLL model are presented in Figure 4.14 and 4.15 respectively. Where the aircraft lift can be seen to be underestimated with the application of the jet correction on both the wing and stabilizer. The lift slope C_{L_α} is also observed to be underestimated. However, this is not surprising as similar results were obtained in the propellers off analysis. With the application of the jet correction, an underestimation of 4.2% is found for the C_{L_α}.

The moment coefficient and the moment coefficient slope predicted by ALIME are different compared to the wind tunnel data. According to the wind tunnel, the LSS or C_{M_α} should decrease by about 50% relative to the propeller off case from about 0.03 to about 0.02. ALIME determines almost exactly the opposite trend. The C_{M_α} increases by about 50% relative to the propeller off case, from about 0.03 to about 0.04. The difference in LSS prediction is thus caused by the introduction of the propeller, since the F-27 C_{M_α} is predicted within an accuracy of 4% relative to the wind tunnel data in the propellers off analysis.

The lift and moment coefficient without the application of the jet correction are obtained to determine if the jet correction is the reason for the difference in results. This is hypothesized since the jet correction is known to change the lift coefficient as a function of AoA [41, 35]. Results from subsection 3.3.3 and 3.3.4 of the validation phase of the thesis confirm that the jet correction obtained lift coefficient magnitude and slope change with AoA. The C_L and C_M curve of the F-27 NLL model without the jet correction are also presented in Figure 4.14 and 4.15 respectively. Without the application of the jet correction, the lift is overestimation, but only slightly. The C_{L_α} can also be seen to have increased. Without the jet correction C_{L_α} is overestimated by 4.0% with respect to the wind tunnel data. The vertical shift in C_L when no jet correction is applied caused a vertical shift of the F-27 moment coefficients. The C_{L_α} increase also causes C_{M_α} to decrease to -0.044 when not applying the jet correction. Moving the predicted LSS even further away in magnitude from the wind tunnel results without the jet correction.

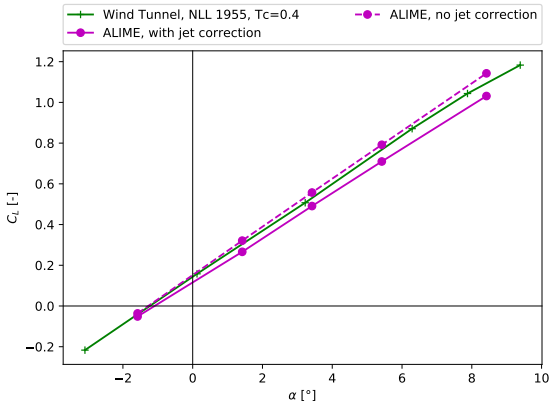

Figure 4.14: The lift coefficient C_L curve of the propeller equipped F-27 NLL model, with and without the jet correction compared to the wind tunnel data by the NLL [55] for the propeller operating point of $J = 0.67$ with $T_c = 0.4$.

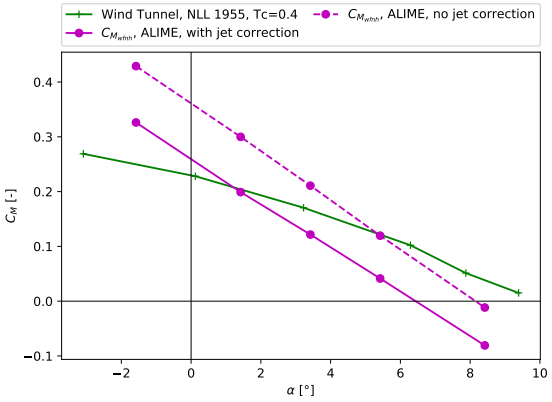

Figure 4.15: The moment coefficient C_M curve of the propeller equipped F-27 NLL model, with and without the jet correction compared to the wind tunnel data by the NLL [55] for the propeller operating point of $J = 0.67$ with $T_c = 0.4$.

The change in lift and moment coefficient slopes of the WFN and stabilizer contributions relative to the propellers off analysis are considered to identify the culprit for the opposite predicted trend in LSS by ALIME. The lift and moment coefficient slopes are determined by fitting a first degree polynomial through the lift and moment coefficient data predicted by ALIME. The difference of the lift and moment coefficient slopes of the WFN and stabilizer for the propellers on with respect to the propeller off analysis are computed and expressed in a percentage by dividing this difference with the propellers off value. The results are presented in Table 4.2. Revealing the WFN lift and moment to have only slightly increased with the introduction of the pro-

peller, while the stabilizer contribution has experienced a larger relative chance. It is thus safe to say that the reason for the LSS overestimation with the propellers is a result of the stabilizer lift contribution increasing, increasing its contribution to the LSS. To explain why the lift contribution of the stabilizer increases, requires an investigation of the flow field at the stabilizer.

Table 4.2: A comparison between the propellers on and off lift and moment slope contributions of the F-27 NLL model by ALIME.

	ALIME, props on, with jet correction [1/°]	Difference, relative to props off [%]
$C_{L_{w_\alpha}}$	0.092387	1.26
$C_{L_{h_\alpha}}$	0.013297	19.7
$C_{M_{wfn_\alpha}}$	0.017250	0.90
$C_{M_{h_\alpha}}$	-0.059183	97.7

4.3.2. Stabilizer Average Dynamic Pressure

The average dynamic pressure at the stabilizer $\bar{q}_h$ is investigated in this section. The $\bar{q}_h$ is calculated using the effective velocity V_{eff} calculated at each panel of the horizontal stabilizer ($n_h m_h$ panels in total). The average effective velocity for all stabilizer panels of $\bar{V}_{eff}$ is calculated, squared and divided by the square of the free stream velocity V_∞ to obtain the average dynamic pressure ratio at the stabilizer $\bar{q}_h/q_\infty$, as given by:

$$\frac{\bar{q}_h}{q_\infty} = \frac{\bar{V}_{eff}^2}{V_\infty^2}, \qquad \bar{V}_{eff} = \frac{1}{n_h m_h} \sum_{i=1}^{n_h m_h} V_{eff_{h_i}}.$$

Figure 4.16 displayed the $\bar{q}_h/q_\infty$ for the F-27 NLL model as calculated using ALIME. For extra reference the $\bar{q}_h/q_\infty$ in the situation without propellers is presented. The $\bar{q}_h/q_\infty$ with propellers when applying the jet correction is about a factor two larger compared to the propellers off case. Without the application of the jet correction, the $\bar{q}_h/q_\infty$ is even higher compared to when the jet correction is applied.

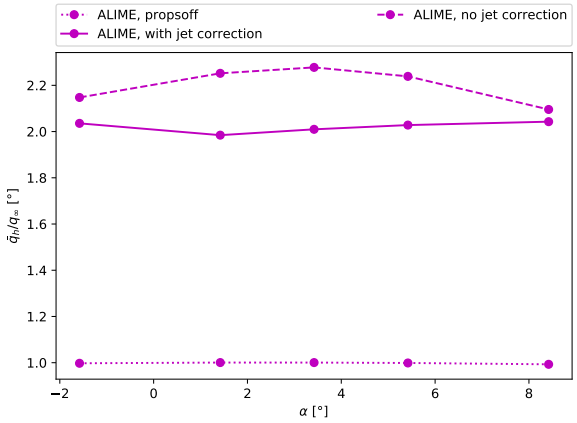

Figure 4.16: The average dynamic pressure ratio at the horizontal stabilizer $\bar{q}_h/q_\infty$ of the F-27 NLL model for propellers off and on at $J = 0.67$ with $T_c = 0.4$ as calculated using ALIME, including results with and without the jet correction applied.

The $\bar{V}_{eff}$ is a function of the $\bar{V}_\infty$ and the average induced velocities of the propeller slipstream $\bar{V}_{z_{ind_s}}$ and the lifting surfaces panels $\bar{V}_{z_{ind_{wh}}}$ as explained in subsection 2.1.5. No slipstream induced velocities are present for the propellers off situation, resulting in a $\bar{q}_h/q_\infty$ of 1 as shown in Figure 4.16. In reality, the wake of the main wing will create a dip in effective velocity at the stabilizer, resulting in a dip in $\bar{q}_h/q_\infty$ below 1. However, this effect is not captures in ALIME. With the introduction of the propeller, the slipstream induces a velocity on every lifting surface panel. For the slipstream to affect the stabilizer, the slipstream needs to be located close to the stabilizer. So a look is taken at the location of the slipstream relative to the stabilizer.

Slipstream Deflection

The induced velocity field by the wing mainly causes the slipstream tube to deflect, as explained in subsection 2.1.4. The slipstream deflection therefore changes with AoA. To evaluate how close the slipstream is to the stabilizer, the total range of slipstream center line deflection of the slipstream is therefore visualized for the considered AoA range. In addition, the slipstream tube contracts depending on the velocities present in the slipstream tube (see subsection 2.1.4). The range of the upper and lower boundary of the slipstream is therefore also important to investigate how the contraction affects the relative distance of the slipstream boundaries to the stabilizer. The ranges are computed by obtaining the center line, upper and lower boundary slipstream position coordinates for each evaluated AoA and finding the maximum and minimum of each data set. With these ranges computed, the total range of slipstream vertical positions relative to the stabilizer can be visualized. This is done in Figure 4.17 and 4.18 for the situation with and without the jet correction applied respectively.

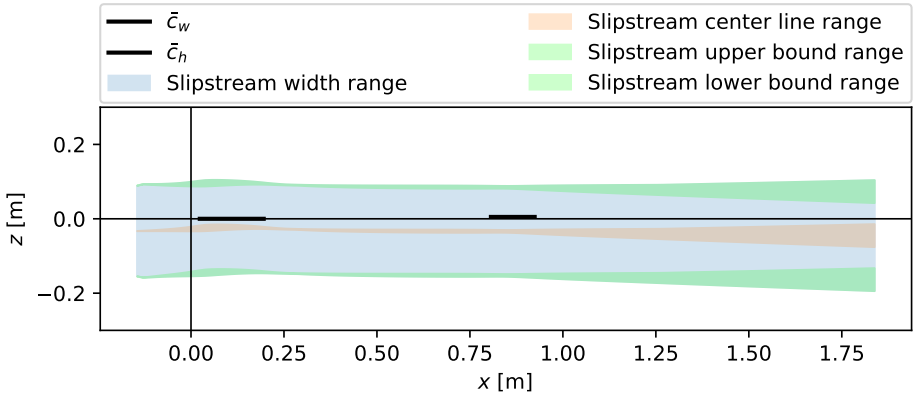

Figure 4.17: A visualization of the slipstream tube position range relative to the wing and horizontal stabilizer over the considered AoA range with the jet correction applied at the propeller operating point $J = 0.67$ with $T_c = 0.4$.

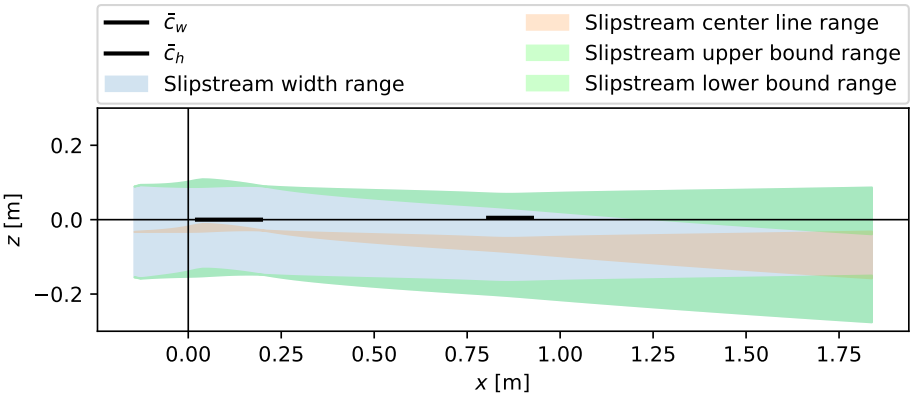

Figure 4.18: A visualization of the slipstream tube position range relative to the wing and horizontal stabilizer over the considered AoA range without the jet correction applied at the propeller operating point $J = 0.67$ with $T_c = 0.4$.

First and foremost, the slipstream engulfs the stabilizer with and without the application of the jet correction. Although, the slipstream tube can be observed to deflect more in the case without the application of the jet correction as a result of the higher induced velocities from the higher wing lift. The center line, upper and lower boundary ranges of the slipstream also become larger because of this.

Each of these slipstream visualization is used to explain the obtained results for the $\bar{q}_h/q_\infty$. First, the situation with the jet correction. The $\bar{q}_h/q_\infty$ is pretty much doubled with respect to the propellers off case.

Also, the $\bar{q}_h/q_\infty$ remains pretty much constant with AoA and Figure 4.17 shows why. The slipstream deflects very little over the AoA range as indicated by the small ranges of the center line, upper and lower boundary. Leaving the stabilizer to interact with about the same radial station of the slipstream over the entire AoA range. The stabilizer therefore encounters about the same slipstream induced velocity over the AoA range. When the jet correction is not applied and the slipstream deflects more, the stabilizer therefore encounters a larger range of the slipstream induced velocities inside the slipstream tube. From Figure 4.16, the $\bar{q}_h/q_\infty$ can be seen to increase and decrease over the AoA range. To see why, a look is taken at the induced velocity distribution near the outer edge of the slipstream. The induced slipstream distribution is a directly related to the propeller blade circulation distribution Γ_p as explained in subsection 2.1.4. Figure 4.19 shows the Γ_p distribution on the F-27 propeller blade for $J = 0.67$ with $T_c = 0.4$. The highest circulation is present near the tip of the propeller blade, resulting in the highest induced velocities near the outer edges of the slipstream . This is what the stabilizer encounters when the jet correction is not applied as Figure 4.18 shows. The slipstream moves over the stabilizer and makes it experience induced velocities corresponding to the propeller circulation at $r/R_p < 0.834$ at the lower AoA range, through the peak circulation at $r/R_p \approx 0.834$ in the middle AoA range and through the decreasing circulation at $r/R_p > 0.834$ at the higher AoA range. Explaining the increase and subsequent decrease in $\bar{q}_h/q_\infty$ experienced with AoA.

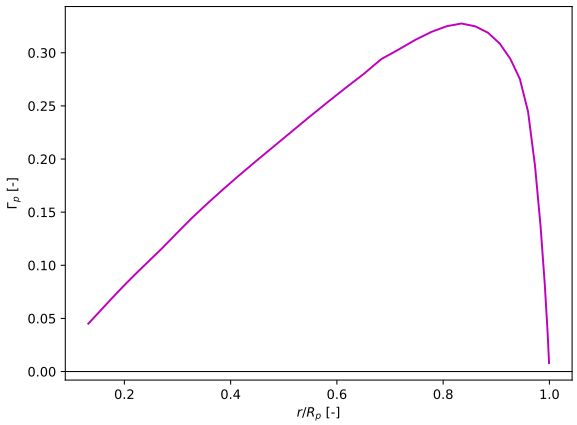

Figure 4.19: The F-27 NLL ALIME BEM propeller model blade circulation distribution Γ_p at $J = 0.67$ with $T_c = 0.4$.

Magnitude of the Average Dynamic Pressure Ratio

Even though the shape of the $\bar{q}_h/q_\infty$ curves over the AoA range can be explained, the magnitude of $\bar{q}_h/q_\infty$ is quite high. Although, $\bar{q}_h/q_\infty$ cannot be directly compared to wind tunnel data at the same power settings, sources such as the flight test by van den Borne and van Hengst indicate that the $\bar{q}_h/q_\infty$ does not exceed 1.3 for the Fokker 50 [12]. The $\bar{q}_h/q_\infty$ is between 1.1 and 1.3 for the same AoA range considered here, but that is for the maximum power settings. Note that the Fokker 50 has a different propeller compared to the F-27. It features a six-bladed propeller that has a very different geometry compared to the F-27 propeller used in this thesis and will thus result in a different circulation distribution and induced velocity distribution in the slipstream. Also note that the Fokker 50 used for the flight test probably has a slightly longer fuselage compared to the F-27 NLL model for the same scale ($25.25m$ instead of $24.1m$), meaning a more rearwards positioned stabilizer. In reality, the slipstream momentum will thus have diffused slightly more before reaching the horizontal stabilizer for the Fokker 50 compared to the F-27 NLL model, although this effect will be quite small and is not captured in ALIME. However, these facts logically still cannot explain the predicted $\bar{q}_h/q_\infty$ of about 2 by ALIME at a lower power setting.

The slipstream induced velocities determined by the slipstream tube model in ALIME can therefore be said to be overestimated. The largest contribution of V_{eff} is the slipstream induced velocity component in the x-direction $V_{x_{inds}}$, pointing to this slipstream contribution being overestimated as a result of the described analysis of the $\bar{q}_h/q_\infty$. The F-27 NLL model propeller circulation fundamentally determines the slipstream induced velocities as stated before. However, the propeller model is known to match the propeller thrust of the wind tunnel test well as shown in Appendix B. A problem with the propeller model in this thesis though, is the fact that it is created by combining information on F-27 propellers from literature, but with no proof that it is close to the actual propeller used during the wind tunnel tests by the NLL. The propeller geometry

used by NLL on their F-27 model is not available in literature. The first step to obtain a better estimate for the slipstream induced velocities requires a more accurate propeller model using the exact propeller geometry and performance as in the wind tunnel experiments.

Vertical Slipstream-Stabilizer Separation

The vertical distance or separation between the slipstream center line and the horizontal stabilizer Δz_h is discussed, because it is one of the main points of interest for this thesis. When inspecting Figure 4.17, the vertical position of the slipstream center line ranges between $-0.030m$ and $-0.038m$ when the jet correction is applied. The stabilizer is vertically located at $z_h = 0.00667m$, see Appendix A. The $\frac{\Delta z_h}{R_p}$ for the distance between the slipstream center line lower and upper range to the stabilizer MAC LE ranges from 0.30 to 0.37, compared to a ratio of $\frac{\Delta z_w}{R_p} = \frac{\Delta z_p}{R_p} = 0.27$ for the wing relative to the location of the propeller disk center. In the case where the jet correction is not applied, it is already pointed out in the previous discussion that the slipstream deflects away further from the stabilizer. At the MAC LE of the stabilizer, the slipstream center line range is between about $-0.0487m \leq z \leq -0.0841m$, resulting in distance ratio from the stabilizer of 0.44 and 0.73. This is much larger compared to the case when the jet correction is being applied.

Despite the quantification of the vertical distance ratios between the stabilizer and the slipstream center line, no knowledge is available in literature on what vertical distance ratio is acceptable in terms of applying the jet correction to any lifting surface when this vertical distance ratio is not equal to zero.

4.3.3. Stabilizer Average Downwash

To determine the average downwash, a look it taken at the definition of the effective AoA of the stabilizer. The effective AoA at the stabilizer α_{eff_h} at the stabilizer is given by [39]:

$$\alpha_{eff_h} = \alpha - \varepsilon_h + i_h.$$

After rearranging the expression, one can see that the downwash at the stabilizer is obtained by subtracting the effective AoA from the AoA. Note that the incidence angle of the stabilizer i_h on the F-27 is zero, see Appendix A. In ALIME, the average downwash $\bar{\varepsilon}_h$ is determined by averaging the α_{eff} of all the panels on the stabilizer (equal to an amount of $n_h m_h$) and subtracting this average from the AoA:

$$\bar{\varepsilon}_h = \alpha - \bar{\alpha}_{eff_h} = \alpha - \frac{1}{n_h m_h} \sum_{i=1}^{n_h m_h} \alpha_{eff_{h_i}},$$

where i is the counter index.

The calculated $\bar{\varepsilon}_h$ is presented in Figure 4.20. What becomes apparent immediately is the decrease in downwash with the introduction of the propeller. The downwash should in fact increase with an increase the thrust, as also observed by Obert [38]. The higher wing lift as a result of the propeller slipstream-wing interaction should increase the circulation of the wing, increasing the downward induced velocities at the stabilizer, increasing the downwash. This explains the opposite trend observed for the predicted LSS change with the introduction of the propeller.

The predicted decrease in $\bar{\varepsilon}_h$ occurs for both the propeller on case with and without the jet correction. The $\bar{\varepsilon}_h$ should be higher for the propeller on situation without the jet correction applied compared to with the application of the jet correction, since the extra lift on the main wing without the jet correction applied induces more downwash at the stabilizer compared to the lower wing lift with the jet correction applied. Figure 4.20 does indeed show the average downwash to be higher without the application of the jet correction, compared to the jet correction being applied.

The α_{eff_h} is calculated in ALIME as the angle between the vertical and horizontal total velocity components present at the stabilizer, V_z and V_x as defined in subsection 2.1.5. The introduction of the propeller is to blame for the wrong trend in vertical shift of $\bar{\varepsilon}_h$, hinting that a change in induced velocity components in the total velocities as a result of the propeller slipstream is to blame for this wrong trend in average downwash.

The average induced velocity components in x and z at the stabilizer are therefore computed. The induced velocity in the x-direction is solely made up from the slipstream induced velocities as expressed by Equation 2.27. Figure 4.21 show the $\bar{V}_{x_{ind_h}}$ normalized with the free stream velocity V_∞ for the considered AoA range with propellers off and on and with the jet correction applied and not applied. Without propellers, the $\bar{V}_{x_{ind_s}}$ are zero at the stabilizer, as expected. When the propeller is introduced, the $\bar{V}_{x_{ind_{s_h}}}$ looks very similar to the results for the average dynamic pressure with propellers on. In addition, with the propeller on, the

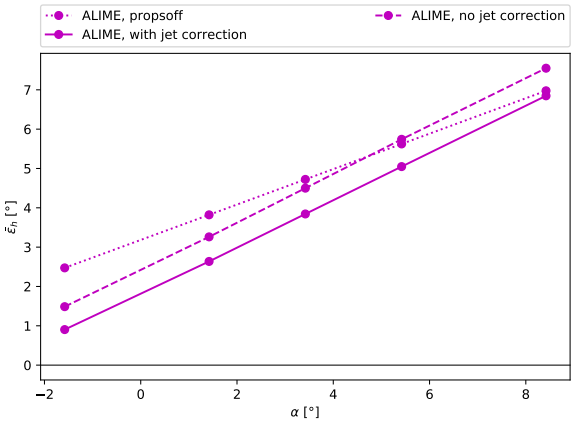

Figure 4.20: The average downwash at the horizontal stabilizer of the F-27 NLL model for propellers off and on at $J = 0.67$ with $T_c = 0.4$ as calculated using ALIME, including results with and without the jet correction applied.

induced velocity increases by about 50% with the propeller being introduced, explaining why the $\bar{q}_h / q_\infty$ results were doubled when introducing the propeller. These $\bar{V}_{x_{ind_w}}$ results thus align with the discussion result on $\bar{q}_h / q_\infty$. Where $\bar{V}_{x_{ind}}$ is identified as its largest contribution.

The z-direction induced velocities consists of two components, the slipstream induced velocities and the induced velocities because of the wing and stabilizer circulation. Each component is individually investigated. The average vertical induced velocity component by the slipstream on the stabilizer is predicted to equal to zero over the entire AoA range with and without the jet correction applied, the positive and negative induced velocities created by the up and down going blade cancel each other out. The average induced z-direction velocities by the wing and stabilizer panels circulation on the stabilizer $\bar{V}_{z_{ind_{wh}}} / V_\infty$ are displayed in Figure 4.22. These results show the origin of the problem where the average downwash decreases with the introduction of the propeller. The $\bar{V}_{z_{ind_{wh}}}$ magnitude should be lower when the propeller is present, regardless of the jet correction being applied. Extra research is required to investigate why exactly this occurs. This might come down to a modeling error in ALIME. The $\bar{V}_{z_{ind_{wh}}}$ without the application of the jet correction is lower compared to the jet correction being applied, which is as expected.

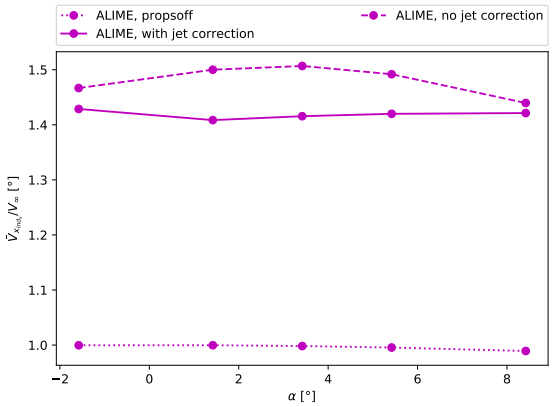

Figure 4.21: The average slipstream x-direction induced velocity at the horizontal stabilizer $\bar{V}_{x_{ind_h}}$ of the F-27 NLL model for propellers off and on at $J = 0.67$ with $T_c = 0.4$ as calculated using ALIME, including results with and without the jet correction applied.

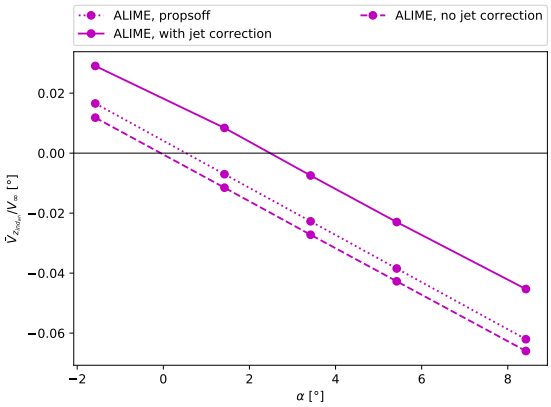

Figure 4.22: The average wing and stabilizer z-direction induced velocity $\bar{V}_{z_{ind_{wh}}}$ at the horizontal stabilizer of the F-27 NLL model for propellers off and on at $J = 0.67$ with $T_c = 0.4$ as calculated using ALIME, including results with and without the jet correction applied.

5

Conclusions

The aim of this thesis project is to investigate the applicability of the correction by Rethorst at the horizontal stabilizer in VLM methods for a conventional high wing, low stabilizer configuration aircraft featuring dual IB propellers, like the Fokker F-27, in the cruise configuration and condition. The application of the Rethorst correction at the stabilizer requires the assumptions used for the derivations to apply and the predicted lift using the correction to match wind tunnel data or CFD simulations. The work performed in this thesis is not enough to answer the main research question on the applicability of the Rethorst correction to the horizontal stabilizer within the mentioned aircraft configuration scope, because none of the stated requirements are not met. However, the necessary work and research left to do before being able to successfully draw a conclusion is identified in this thesis.

The Rethorst correction assumption stating that the vertical distance between the stabilizer and the propeller center line should be zero is most questionable in the case of the horizontal stabilizer. The vertical distance between the slipstream center line and the stabilizer found in this thesis is larger compared to the distance between the wing and propeller center line for the entire considered AoA range of 1.54° to 8.46°. The Rethorst correction is therefore less applicable to the stabilizer compared to the wing for the considered AoA range. The vertical slipstream center line to horizontal stabilizer distance is highly dependent on the slipstream deflection. Applying the Rethorst correction to the wing increases the applicability of the Rethorst correction to the stabilizer by limiting the slipstream deflection at the stabilizer, as a result of the lower wing lift.

The average dynamic pressure at the horizontal stabilizer being over estimated is one of the reasons why no accurate stabilizer lift prediction is obtained. Within the condition of the slipstream engulfing the stabilizer, the slipstream induced velocities dictate the average dynamic pressure at the stabilizer. The predicted slipstream induced velocity magnitudes in this thesis are high compared to flight test data. The slipstream induced velocities in the used slipstream tube model are dictated entirely by the propeller circulation distribution. Uncertainty in the F-27 propeller geometry and its BEM model performance therefore possibly contributes to the overestimation of the slipstream induced velocities.

The average downwash at the stabilizer is predicted to decrease with the introduction of the propeller in this thesis, which is the opposite observed trend when referencing wind tunnel data. This thesis identifies the vertical induced velocities at the horizontal stabilizer by the wing and stabilizer VLM panels to be the culprit, which predict a decrease in vertical induced velocity with the additional wing and stabilizer lift introduced by the propeller slipstream. This indicates the possibility of a modeling error. The time frame of the thesis project does not allow for an investigation to find this possible modeling error.

6

Recommendations

To be able to draw a conclusion on the applicability of the Rethorst correction at the horizontal stabilizer for conventional configuration high wing, low stabilizer and dual IB propellers aircraft, the three practices described in this chapter need to be considered.

A study concerning the effectiveness and accuracy of the Rethorst correction outside the scope of its assumption and or restriction is necessary, with an emphasis on the assumption on the vertical distance between the slipstream center line and the lifting surface that the correction is applied to. Knowledge on this subject could possible widen the application scope of the Rethorst correction or indicate what assumptions the Rethorst correction is especially sensitive to. Knowledge that is necessary before being able to consider the Rethorst correction for the horizontal stabilizer, since that requires most of the assumptions to be more flexible compared to the application of the Rethorst correction on the main wing.

The first step to better represent the induced velocities in the propeller slipstream requires a more representative F-27 propeller geometry and operation settings information needs to be obtained. Since literature does not contain this information, it needs to be requested at the original source. Ones a more representative propeller model is obtained, the average dynamic pressure ratio is likely still not going to match flight or wind tunnel test data because of the slipstream model not capturing all aspects of a realistic propeller slipstream. An examples being the propeller nacelle wake in the slipstream and the interaction of the slipstream with the wing wake, which are important for the representation of the average dynamic pressure at the stabilizer. A deeper analysis should be performed on the potential of the slipstream tube model to predict the slipstream induced velocities at the stabilizer in ALIME without the capture of the mentioned wake interactions effects.

Lastly, more research needs to be done with regards to the level of modeling fidelity in ALIME, which is the airframe VLM, propeller BEM and slipstream tube combination model used in this thesis. Emphasis needs to be put on the slipstream induced velocities and their effects on the wing and horizontal stabilizer, since capturing this interaction is one of the main goals with which ALIME is created in this thesis. Capturing the increase in vertical induced velocities by the wing and stabilizer VLM panels as a result of the propeller at the location of the horizontal stabilizer is of main importance for the progress in investigating the applicability of the Rethorst correction to the horizontal stabilizer.

Bibliography

[1] *Aanvullende metingen aan het F-27 model 1:15 met verlengde romp, in hoofdzaak betreffence het stoorgiermoment bij a-symmetrische trekkracht.* Rapport A.1416. Nationaal Luchtvaart Laboratorium, 1956.

[2] European Aviation Safety Agency. *Certification Specifications and Acceptable Means of Compliance for Large Aeroplanes (CS-25).* Report. European Aviation Safety Agency, 2021.

[3] European Aviation Safety Agency. *Type-Certification Data Sheet for Fokker F27.* No. EASA.A.036. European Aviation Safety Agency, 2016.

[4] C. Alba. "A Surrogate-Based Multi-Disciplinary Design Optimization Framework Exploiting Wing-Propeller Interaction". Master Thesis. Delft University of Technology, 2017.

[5] J.D. Anderson. *Aircraft Performance and Design.* McGraw-Hill, 1999. ISBN: 0-07-001971-1.

[6] J.D. Anderson. *Computational Fluid Dynamics: The Basics with Applications.* McGraw-Hill, 1995. ISBN: 0-07-001685-2.

[7] J.D. Anderson. *Fundamentals of Aerodynamics.* 2016. ISBN: 9781259251344 1259251349.

[8] N. van Arnhem. "Design and Analysis of an Installed Pusher Propeller with Boundary Layer Inflow". Master Thesis. Delft University of Technology, 2015.

[9] N. van Arnhem et al. "Engineering Method to Estimate the Blade Loading of Propellers in Nonuniform Flow". In: *AIAA Journal* 58.12 (2020), pp. 5332–5346. ISSN: 0001-1452. DOI: 10.2514/1.J059485.

[10] H. Binkhorst. *Windtunnelmetingen aan de romp met staartvlakken van een model van de Fokker F-27 "Friendship" in de lage-snelheidstunnel van de onderafdeling der Vliegtuigbouwkunde.* Memorandum M-59. Technische Hogeschool Delft, 1962.

[11] H. Binkhorst and C. Spoon. *Samenvatting van de windtunnelmetingen aan een model van de Fokker F-27 "Friendship" in de lage-snelheidstunnel van de onderafdeling der Vliegtuigbouwkunde.* Memorandum M-60. Technische Hogeschool Delft, 1962.

[12] P.C.M. van den Borne and J. van Hengst. "Investigation of Propeller Slipstream Effects on the Fokker 50 Through In-Flight Pressure Measurements". In: *AIAA 8th Applied Aerodynamics Conference* (1990).

[13] T. Bouquet. "Modelling the Propeller Slipstream Effect on the Longitudinal Stability and Control". Master Thesis. Delft University of Technology, 2016.

[14] European Commission. *Flightpath 2050: Europe's Vision for Aviation: Report of the High-Level Group on Aviation Research.* Report. 2011. DOI: 10.2777/50266.

[15] J.T. Conway. "Analytical solutions for the actuator disk with variable radial distribution of load". In: *Journal of Fluid Mechanics* 297 (1995), pp. 327–355. ISSN: 0022-1120. DOI: 10.1017/S0022112095003120.

[16] H.K. Epema. "Wing Optimisation for Tractor Propeller Configurations: Validation and Application of Low-Order Numerical Models Adapted to Include Propeller-Induced Velocities". Master thesis. Delft University of Technology, 2017.

[17] M.E. Eshelby. *The Influence of Running Propellers on Low Speed Longitudinal Static Stability Trim Curves.* Canfield Report Aero No. 34. Cranfield Institute of Technology, 1977.

[18] J.T. Goates. "Development of an Improved Low-Order Model for Propeller-Wing Interactions". Master Thesis. Utah State University, 2018.

[19] E.W. Graham et al. *A Preliminary Theoretical Investigation of the Effects of Propeller Slipstream on Wing Lift.* Report SM-14991. Douglas Aircraft Co., 1953.

[20] J.R. Hooker et al. "Overview of low speed wind tunnel testing conducted on a wingtip mounted propeller for the workshop for integrated propeller prediction". In: *AIAA Aviation 2020 Forum*, pp. 1–19. DOI: 10.2514/6.2020-2673.

[21] E.N. Jacobs and K.E. Ward. *Interference of Wing and Fuselage from Tests of 209 Combinations in the N.A.C.A Variable-Density Tunnel*. Report No. 540. National Advisory Committee for Aeronautics, 1935.

[22] J. Katz and A. Plotkin. *Low-Speed Aerodynamics*. 2nd ed. Cambridge Aerospace Series. Cambridge: Cambridge University Press, 2001. ISBN: 9780521665520. DOI: DOI:10.1017/CBO9780511810329.

[23] K. Katzoff. *Longitudinal Stability and Control with Special Reference to Slipstream Effects*. Report No. 690. National Advisory Committee for Aeronautics, 1939.

[24] C. Koning. *Influence of the Propeller on Other Parts of the Aircraft Structure*. Ed. by W.F. Durand. Vol. IV. Aerodynamics Theory. Berlin: Springer, 1935.

[25] D. Lednicer. *A VSAERO Analysis of Several Canard Configured Aircraft*. Technical Paper 881485. SAE International, 1988. DOI: 10.4271/881485.

[26] D. Lednicer. *A VSAERO Analysis of Several Canard Configured Aircraft - Part 2*. Technical Paper 892287. SAE International, 1989. DOI: 10.4271/892287.

[27] Q. van der Leer. "An Assessment of a Regional Turboprop Featuring Wingtip-Mounted Propellers". Master Thesis. Delft University of Technology, 2021.

[28] J. Manée. "LR NLL Rapport A-1508 B, Windtunnel investigation of the influence of the aircraft configuration on the yawing- and rolling moments of a twin-engined, propeller-driven aircraft with one engine Inoperative". In: *Congress Aeronautico Europeo* (1962).

[29] J. Mariens. "Wing Shape Multidisciplinary Design Optimization". Master Thesis. Delft University of Technology, 2012.

[30] L. Miranda and J. Brennan. "Aerodynamic effects of wingtip-mounted propellers and turbines". In: *4th Applied Aerodynamics Conference*. Fluid Dynamics and Co-located Conferences. American Institute of Aeronautics and Astronautics, 1986. DOI: 10.2514/6.1986-1802.

[31] M.D. Moore et al. "High-Speed Mobility through On-Demand Aviation". In: *AIAA Journal* 2013 Aviation Technology, Integration, and Operations Conference (2013). DOI: 10.2514/6.2013-4373.

[32] H. Multhopp. *Aerodynamics of the Fuselage*. Technical Memorandum No. 1036. National Advisory Committee for Aeronautics, 1942.

[33] M.M. Munk. *The Aerodynamic Forces on Airship Hulls*. Report No. 184. National Advisory Committee for Aeronautics, 1925.

[34] B. Munniksma. *N-250 Propeller Shop Test*. Report. 1990.

[35] R. Nederlof. "Improved modeling of propeller-wing interactions with a lifting-line approach: Investigation of a suitable correction method to account for the finite slipstream height". Master thesis. Delft University of Technology, 2020.

[36] C.N. Nelson. *Flight Stability and Automatic Control*. University of Notre Dame: McGraw-Hill, 1998. ISBN: 0-07-046273-9.

[37] F.T.M. Nieuwstadt, B.J. Boersma, and J. Westerweel. *Turbulence: Introduction to Theory and Applications of Turbulent Flows*. Springer, 2016. ISBN: 978-3-319-31597-3. DOI: 10.1007/978-3-319-31599-7.

[38] E. Obert. *A method of the determination of the effect of propeller slipstream on static longitudinal stability and control of multi-engined aircraft*. Report LR-761. Delft University of Technology, 1994.

[39] E. Obert. *Aerodynamic design of transport aircraft*. Amsterdam: IOS press, 2009. ISBN: 978-1-58603-970-7.

[40] R.K. Prabhu. "Studies on the Interference of Wings and Propeller Slipstreams". Doctoral Thesis. Old Dominion University, 1984. DOI: 10.25777/ezag-d204.

[41] S.C. Rethorst. "Aerodynamic of Nonuniform Flows as Related to an Airfoil Extending Through a Circular Jet". In: *Journal of the Aerospace Sciences* 25.1 (1958), pp. 11–28. DOI: 10.2514/8.7479.

[42] S.C. Rethorst. "Characteristics of an Airfoil Extending Through a Circular Jet". Doctoral Thesis. California Institute of Technology, 1956.

[43] J. Roskam. *Airplane Design Part IV: Preliminry Calculation of Aerodynamic, Thrust and Power Characteristics*. Lawrence, Kansas: Roskam Aviation and Engineering Corporation, 1987.

[44] H. Schlichting and E. Truckenbrodt. *Aerodynamics of the Airplane*. McGraw-Hill, 1979. ISBN: 0-07-055341-6.

[45] M.J.T. Schroijen and R. Slingerland. "Propeller installation effects on Multi-engine Propeller Aircraft Directional Stability and Control". In: *25th International Congress of the Aeronautical Scienes (ICAS)*. 2006.

[46] W.R. Sears. "Some Aspects of Non-Stationary Airfoil Theory and Its Practical Application". In: *Journal of the Aeronautical Sciences* 8.3 (1941), pp. 104–108. DOI: 10.2514/8.10655.

[47] T. Sinnige. "Aerodynamic and Aeroacoustic Interaction Effects for Tip-Mounted Propellers: An Experimental Study". Doctoral thesis. Delft University of Technology, 2018. DOI: 10.4233/uuid:214e1e9a-c53e-47c7-a12c-b1eb3ec8293b.

[48] T. Sinnige et al. "Wingtip-mounted propellers: Aerodynamic analysis of interaction effects and comparison with conventional layout". In: *Journal of Aircraft* 56.1 (2019), pp. 295–312. DOI: 10.2514/1.C034978.

[49] C.L. Spigt and A. de Gelder. *Windtunnelmetingen aan een model van de F27 "Friendship" uitgevoerd in de lage-snelheids tunnel van de Onderafdeling der Vliegtuigbouwkunde*. VTH Memorandum M-42. Technische Hogeschool Delft, 1959.

[50] J. Stüper. *Effect of Propeller Slipstream on Wing and Tail*. Technical Memorandum No. 874. National Advisory Committee for Aeronautics, 1938.

[51] E. Torenbeek. *Optimum Cruise Performance of Subsonic Transport Aircraft*. Delft: Delft University Press, 1998. ISBN: 90-407-1579-3.

[52] E. Torenbeek. *Synthesis of subsonic airplane design : an introduction to the preliminary design, of subsonic general aviation and transport aircraft, with emphasis on layout, aerodynamic design, propulsion, and performance*. Delft: Delft University Press, 1982. ISBN: 90-247-2724-3.

[53] J.C. van der Vaart. and H. Muhammad. *Static Longitudinal Stability and Control Characteristics of the Fokker F-27 'Friendship' Calculated by Simple Handbook Methods*. Report LR-394. Delft University of Technology, 1983.

[54] L.L.M. Veldhuis. "Propeller Wing Aerodynamic Interference". Doctoral Thesis. Delft University of Technology, 2005.

[55] C.B. van der Voort. *Onderzoek aan het F27: 6 componenten model (1:15) met verlengde romp. Figuren*. Rapport A.1403. 1955.

[56] R. Willemsen. "A sensitivity study on the aerodynamic performance of a wingtip-mounted tractor propeller-wing system". Master thesis. Delft University of Technology, 2020.

[57] N.J. van Wonderen. "Analysis of propeller slipstream effects on the directional stability using a potential flow model". Master Thesis. Delft University of Technology, 2017.

[58] *XFLR5 Analysis of foils and wings operating at low Reynolds numbers: Guidelines*. Tech. rep. 2013.

[59] J. de. Young. "Propellers at High Incidence". In: *AIAA General Aviation Aircraft Design and Operations Meeting* (1965). DOI: 10.2514/3.43646.

A

Fokker F-27 Model Geometries

This chapter highlights the geometry differences between the F-27 models used for wind tunnel experiments by TU Delft and NLL.

When referencing literature, it becomes apparent that the Fokker F-27 aircraft series features various variants. The F-27 started off with the first version, the Mark 100. Fokker started to adapt the F-27 Mark 100 with en-lengthened fuselages and more powerful engines. This lead to the creation of many more F-27 Marks including specific version for the military and other intermediate versions. From the Mark 700 onward, the Mark 050 is introduced. From the F-27 Mark 050 onward, the aircraft is also known as the Fokker 50. The Fokker 50 is also built in a few different versions [3]. All these variants of the F-27 and Fokker 50 featured differences in geometry, such as fuselage length[1].

One has to be aware of the variants of F-27 that exist. Wind tunnel models of the F-27 can be based on any of the versions of the F-27 and can therefore have different geometries. The same is true for the F-27 models used by TU Delft and NLL for wind tunnel experiments, which are considered in this thesis. The NLL and TU Delft both provide detailed sketches of the models to describe the geometry. From both sketches side by side, one is hardly able to see the differences in geometry. When overlaying the sketches on top of each other, disregarding the different model scales, the differences in geometry become apparent. The wing and stabilizer geometry appears identical. The NLL and TU Delft model feature the same fuselage length in front of the main wing, but the NLL has a longer rear fuselage length. The horizontal stabilizer is located more rearward for the NLL compared to the TU Delft model.

The geometry of the wing and stabilizer of the TU Delft and NLL F-27 model is presented in the wind tunnel test series of technical reports by TU Delft [11, 49, 10] and NLL respectively [55, 1]. Table A.1 summarizes the geometry of the TU Delft and NLL models. Where the geometry values are directly read from or calculated using the model sketches of the mentioned technical reports. The sketches of the NLL and TU Delft F-27 models are presented on the next pages respectively [55, 10].

Table A.1: The wing and horizontal stabilizer geometry of the TU Delft and NLL F-27 models.

	Wing		Horizontal Stabilizer	
	TU Delft	NLL	TU Delft	NLL
b [m]	1.45	1.936	0.4875	0.636
c_r [m]	0.17325	0.2310	0.11875	0.15833
c_t [m]	0.07	0.0933	0.0475	0.06333
i [°]	3.46	3.42	0	0
ε [°]	-2	-2	0	0
Root airfoil, Tip airfoil	NACA64421, NACA64415	NACA64421, NACA64415	NACA63-014A	NACA63-014A
x_{LE_r} [m]	0	0	0.54	0.7779
x_{LE_t} [m]	0.0413	0.0551	0.05	0.06667
z [m]	0	0	0.005	0.00667

[1] Fokker 27 General, fokker-aircraft.info, http://www.fokker-aircraft.info/f27general.htm [Accessed 29/3/2023]

NATIONAAL LUCHTVAARTLABORATORIUM	Rapport A.1403	Fig. 1

Maatschets van het F-27 model 1:15 met verlengde romp

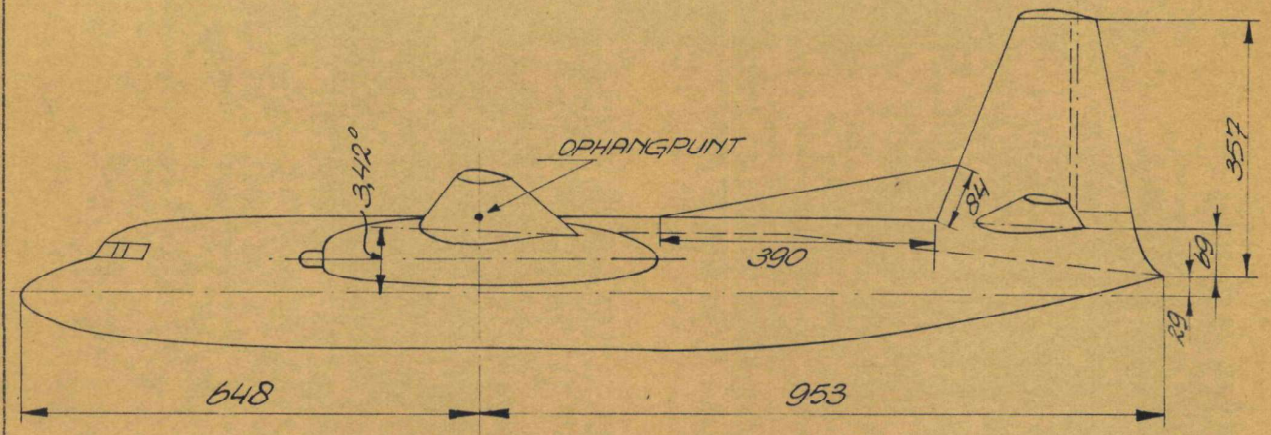

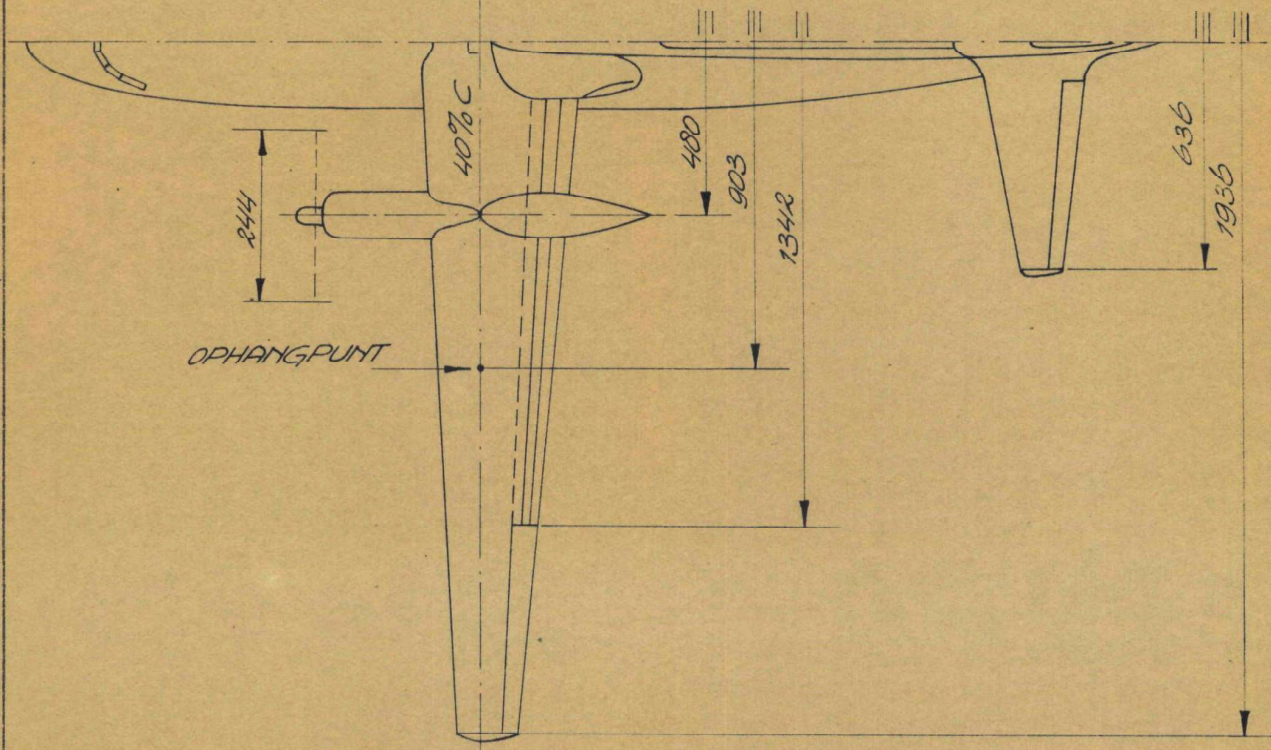

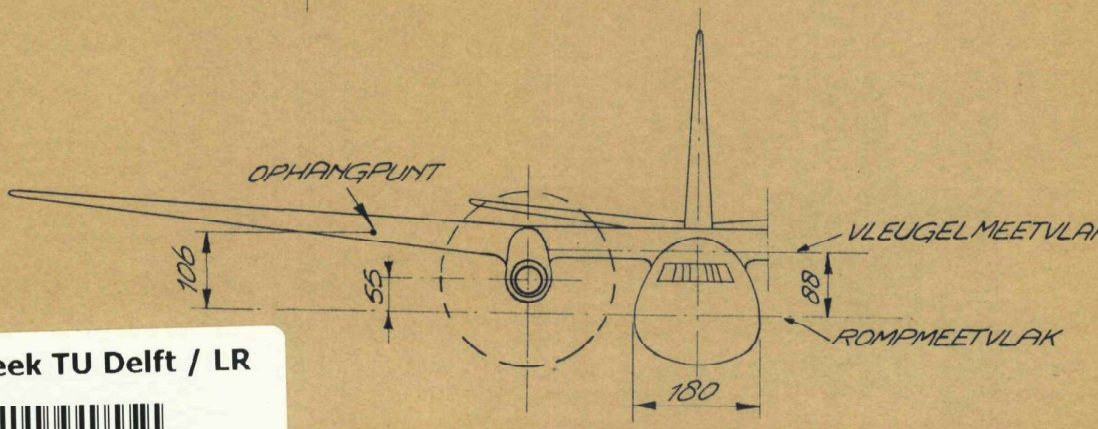

SCHAAL 1:10 MATEN IN mm

P.L.

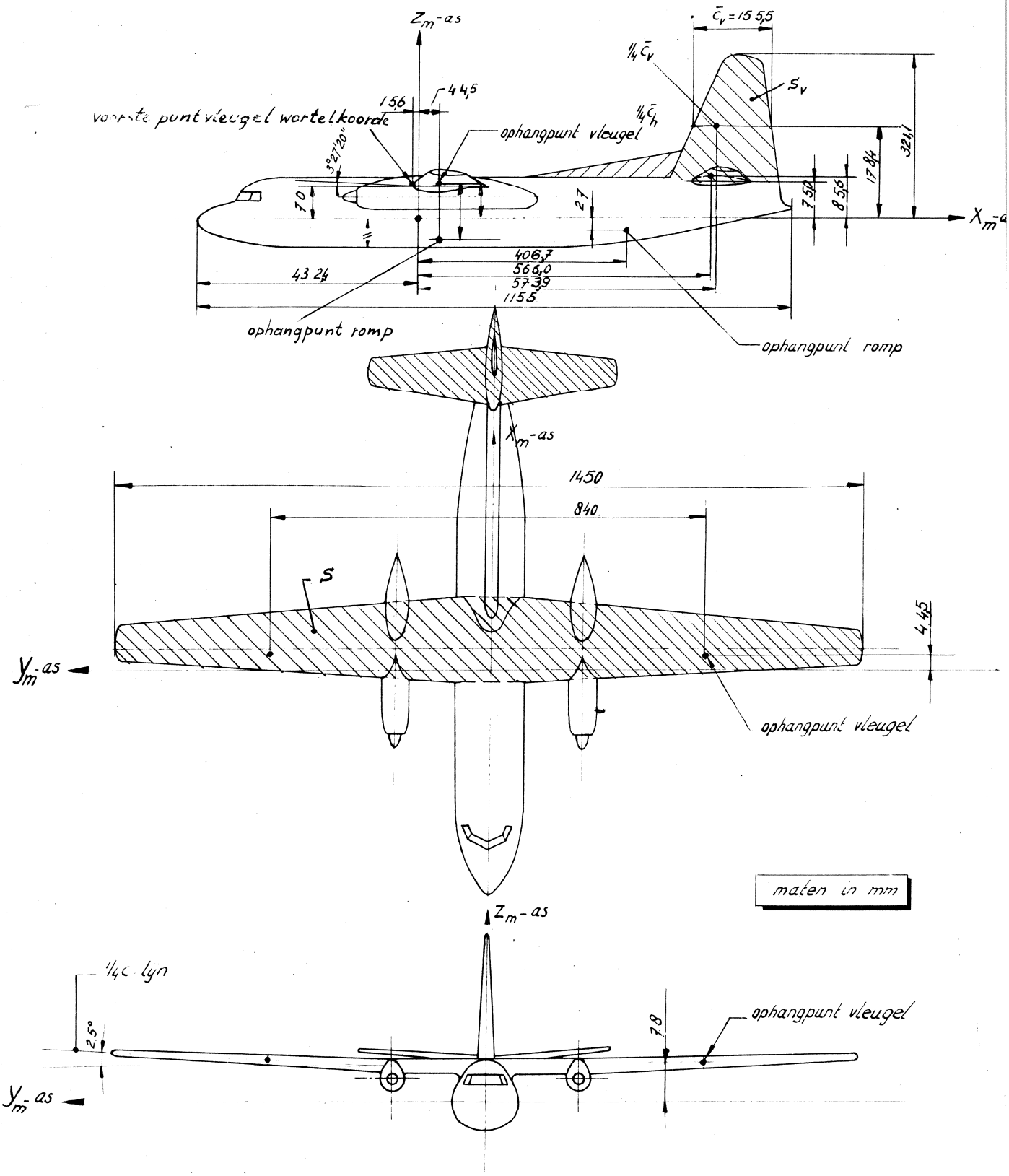

Fig. 1-b: De afmetingen van het model en het gebruikte meetassenstelsel.

B

Fokker F-27 Propeller Model

The propeller geometry for the BEM model for the F-27 used in this thesis report is covered in this chapter. Very little literature is available on the propeller geometry of the propeller used on the F-27. A propeller model is therefore created to resemble the propeller model used during the wind tunnel tests by NLL, for the purpose of this case study.

For inspiration, literature on the propellers of the F-27 aircraft series, including the Fokker 50, is considered. Although similar to the F-27, Fokker 50 is a different aircraft and is the descendant of the F-27. The Fokker 50 aircraft series featured various propellers, a two-blade, four-blade and six-blade propeller. The later versions of the Fokker 50 featured the six-bladed propeller, while the earliest versions featured the two-bladed propeller [3]. The Pilot Operating Handbook of the Fokker 50 mentions the propeller blades are manufactured by Dowty Rotol[1]. The type certification documentation of the Fokker F-27 and 50 models mention various propeller blade models used on the Fokker 50 series [3], such as the Dowty Rotol Model (c) R175/4-30-4/13E with 4 RA.25899 blades and many more. Bouquet mentions an N250 six-bladed propeller used for the Fokker 50 in this masters thesis [13], originating from a propeller test shop report by Munniksma [34]. Van Wonderen created an aircraft and propeller model based on a report by Manée, which is based on the Fokker 50 [57, 28].

A propeller model is created for the F-27 NLL model based on the propeller geometry by van Wonderen, featuring an N250 propeller blade section. The propeller geometry is presented in Table B.1. The propeller features four blades, to match the amount of propeller blades used by the wind tunnel tests by NLL [1], with a diameter D_p of 0.244 m and the hub radius set to be located at the fist radial r/R station mentioned in Table B.1.

Table B.1: The F27 NLL model propeller geometry, based on the propeller geometry of van Wonderen [57].

r/R [-]	0.1315	0.3036	0.4991	0.7000	0.8324	0.9495	0.9991
c/R [-]	0.099	0.190	0.221	0.229	0.221	0.190	0.004
θ [°]	62.83	39.86	27.08	19.93	17.00	15.01	14.30

The propeller pitch setting is varied over J to calibrate the propeller performance to the propeller performance documented by NLL. Figure B.1 shows the pitch β_p settings for the considered range of propeller J operating points.

Figure B.2 shows the propeller thrust coefficient T_c of the calibrated propeller model compared to the propeller performance of the wind tunnel tests.

No data is available on the torque performance of the propeller used during the wind tunnel tests by the NLL. This creates uncertainty with regards to the torque performance of the propeller model, thus creating uncertainties in the tangential velocity component generated by the propeller model. Possibly affecting the locally induced AoA of any lifting surface engulfed by the slipstream as a result of the tangential flow component [39].

[1] Fokker 50 Systems, Smartcockpit, https://www.smartcockpit.com/plane/FOKKER/FOKKER%2050.html [Accessed 6/5/2023]

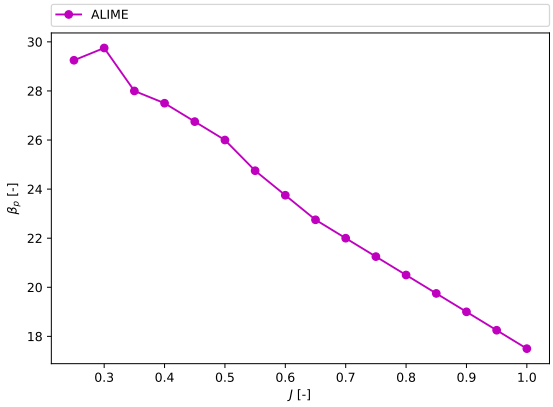

Figure B.1: The F-27 propeller calibration pitch settings to match the propeller performance of the wind tunnel experiment by the NLL [55].

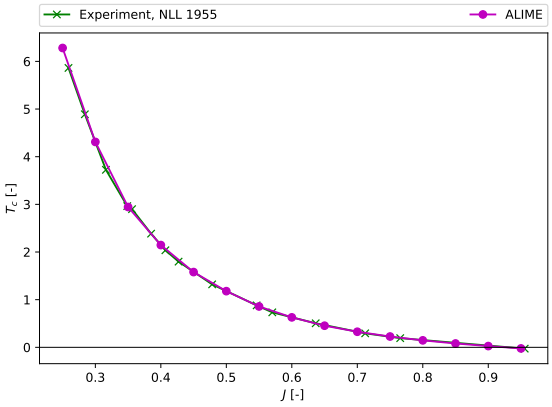

Figure B.2: The F-27 propeller model thrust coefficient T_c compared to the experiment propeller performance in the wind tunnel experiment by the NLL [55].

C

ALIME Extras

This chapter contains extra results and descriptions of implementations that are performed for ALIME, but are not important in the context of the thesis project or became obsolete. This concerns the induced drag coefficient, described in section C.1 and an implementation for a wing kink in ALIME, discussed in section C.2.

C.1. Drag Coefficient

This thesis is not concerned with the drag coefficient as explained in Chapter 1. However the verification and sensitivity analysis also covered the drag coefficient to make sure that the implementations in ALIME also worked for the drag coefficient.

ALIME features two implementation for the calculation of the induced drag coeffcient, from now on referred to as the drag coefficient. The first being the determination of the drag coefficient in the Trefftz plane, as described by Willemsen [56]. The other being the projection of the panel axial and normal forces in the aerodynamic reference frame by means of the angle α. The results in this section feature only the drag coefficient as determined in the Trefftz plane. However, it turns out that both methods determine the drag coefficient very closely. Only at high AoA do both methods start to reveal differences in terms of the drag coefficient [56].

The verification of the drag coefficient for the implementation of the stabilizer is presented in subsection C.1.1, while the sensitivity study results are presented in subsection C.1.2.

C.1.1. Verification

The implementation of the horizontal stabilizer adds another lifting surface, which generates lift and thus induced drag. The induced drag of the complete aircraft, including the propeller force contributions, is calculated in ALIME using Equation 2.34. The induced drag implementation for ALIME is again verified using XFLR5 in Figure C.1, without the contribution of the propeller forces. The results by ALIME agree well with XFLR5.

$$D_{tot} = D_w + D_h - \Delta T_p \cos(\alpha_p) - \Delta N_p \sin(\alpha_p), \qquad C_D = \frac{D_{tot}}{q_\infty S_w} \tag{C.1}$$

C.1.2. Sensitivity Analysis

The sensitivity study covered in subsection 3.2.1 has also been performed for the drag coefficient of the F-27. Note that the mesh chosen in this thesis also takes into account the drag coefficient sensitivity. The drag coefficient turns out not to be the critical when it comes to mesh selection for the F-27. Figure C.2 and C.3 contain the mesh convergence space for the F-27 drag coefficient for the isolated wing and wing-stabilizer combination.

C.2. Wing Kink Implementation

During the first months of the thesis project, another reference aircraft was considered. This reference aircraft featured a kink in its wing. For this reason, the ability to model wing kinks is implemented in ALIME. Over time, it is decided that the F-27 is a more suitable reference aircraft for this thesis project. The F-27 does

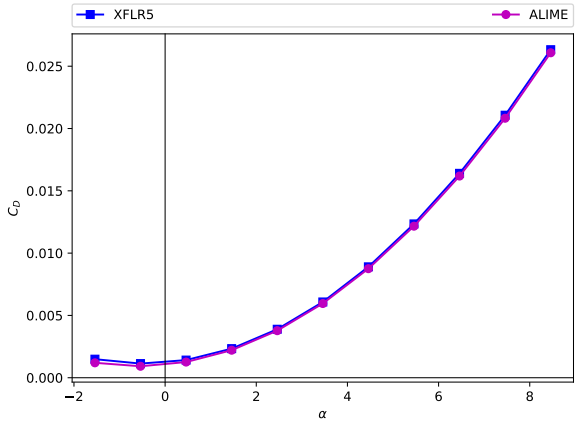

Figure C.1: A comparison between the drag coefficient C_D curve of the TU Delft F-27 wing and stabilizer combination as predicted by ALIME and XFLR5.

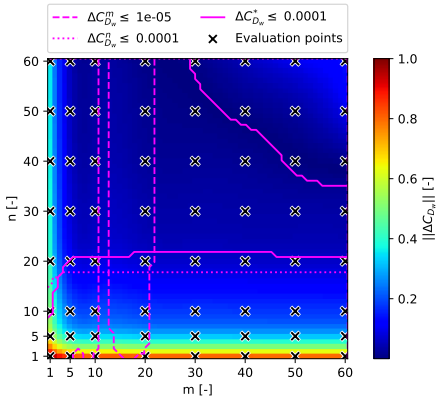

Figure C.2: The convergence space of the F-27 TU Delft model isolated wing C_{D_w} as determined with the *3D* method at $\alpha = 5.46°$, with the lower and upper n and m-direction convergence boundaries.

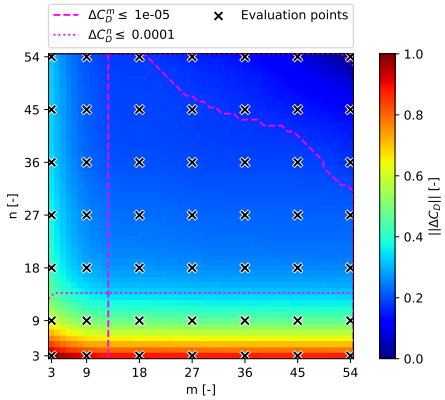

Figure C.3: The convergence field of the F-27 TU Delft model wing-stabilizer combination $C_D = C_{D_w} + C_{D_h}$ as determined with the *3D* method at $\alpha = 5.46°$, with the n and m-direction convergence boundaries.

not feature a wink kink, making the wing kink implementation obselete for the purposes of this thesis. The implementation is fully verified before it is decided to switch reference aircraft. The verification of this wing kink implementation is not removed from ALIME after this fact. The verification of the wink kink is therefore discussed in this appendix.

The ability to model LE, TE or both a LE and TE wing kink exists in ALIME. Kinks can be put on both the main wing and the stabilizer. The implementation consists of adding another wing section to the wing, allowing the location of the wing LE and TE to be specified by the user, effectively creating a kink in the wing. However, the wing kink implementation is limited to one kink only per lifting surface. In addition, when modeling any wing-IB propeller system in ALIME, the wink kink position is limited to the confines of the IB propeller diameter. If no IB propeller is modeled, this limitation on the wing kink position does not apply.

The verification for the wink kink implementation is discussed in subsection C.2.1.

C.2.1. Verification

The verification of the wing kink implementation is done for three different low sweep wing geometries that are based on the verification performed by Willemsen, over an AoA range of $-5° \leq \alpha \leq 15°$. One with a LE kink, a second with a TE kink and the third one with both a LE and TE kink. The wings all feature a NACA2412 airfoil. All geometries are ran with XFLR5 at the same conditions with the same mesh. The results for the wing geometries turn out to be very similar. So only the result for the wing with both the LE and TE are presented.

The LE and TE kink geometry wing features a span of $b = 20m$. The kink wing section is located at $y = 2m$,

with the LE position of the kink section being located at $x = 1.561m$ and this a chord length of $1.279m$. To form the flat TE kink in the wing, the root chord is set to $c_r = 1.840m$. The outer part of the wing features a constant sweep angle of 5.66° beyond the kink and has a tip chord of $c_t = 0.5m$.

The lift and drag distribution at $\alpha = 5°$ and the lift and drag coefficient curves are presented for this wing in Figure C.4 to C.7 respectively. Note, all results in this section are computed using the *farfield* method of determining the AICs, since this verification is performed before the implementation of the horizontal stabilizer. The results agree well with XFLR5. Only at high AoA, so differences between ALIME and XFLR5 become apparent. XFLR5 determines the AIC matrix in 3D while ALIME uses the 2D *farfield* method for these results [58]. The lift and drag distribution magnitude between ALIME and XFLR5 seem to match well, as also observed by Willemsen [56].

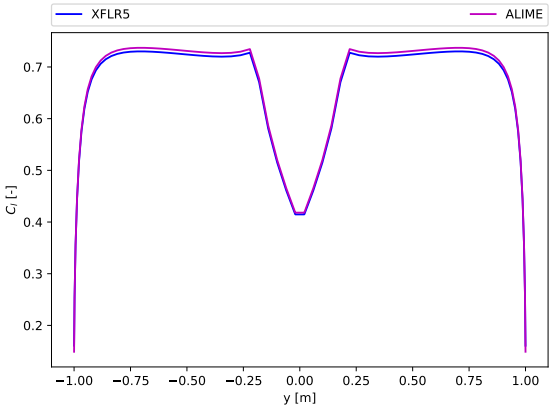

Figure C.4: A comparison of the LE and TE swept wing lift C_l distribution by ALIME as determined with the *farfield* method and XFLR5 at $\alpha = 5°$.

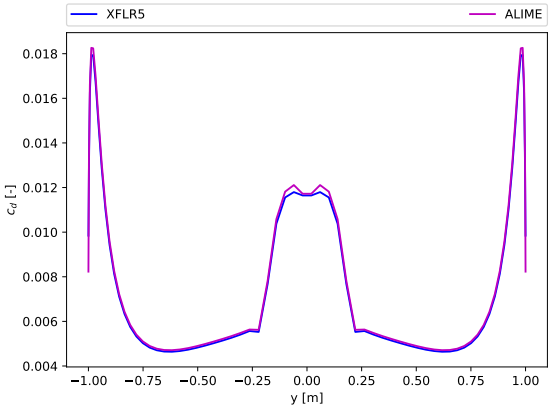

Figure C.5: A comparison of the LE and TE swept wing drag C_d distribution by ALIME as determined with the *farfield* method and XFLR5 at $\alpha = 5°$.

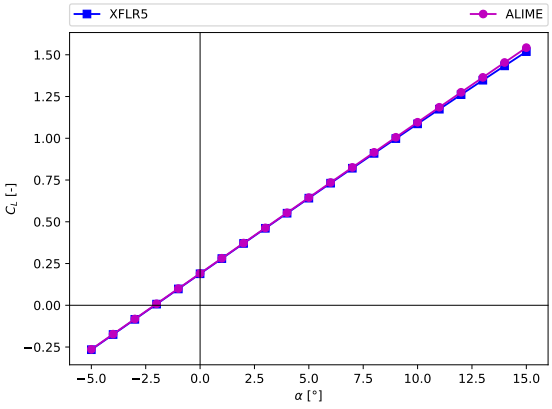

Figure C.6: A comparison of the LE and TE swept wing lift C_L curve by ALIME as determined with the *farfield* method and XFLR5.

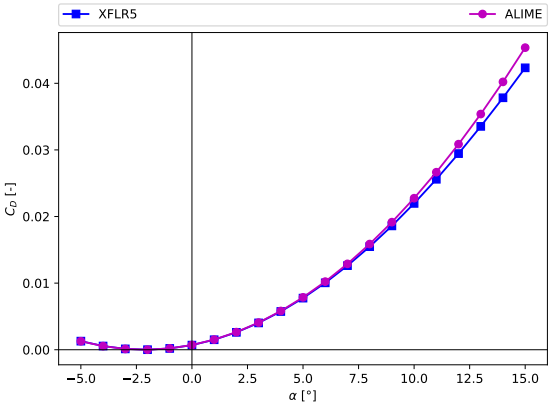

Figure C.7: A comparison of the LE and TE swept wing drag C_D curve by ALIME as determined with the *farfield* method and XFLR5.

D

Fokker F-27 LSS Derivation

The normal N and axial A force of the WFN combination and the horizontal tail as well as the propeller thrust and normal force all contribute to the total aircraft moment around a certain reference point, as shown in Figure D.1. The N_{wfn}, A_{wfn}, N_h and A_h contain the propulsion effects [39].

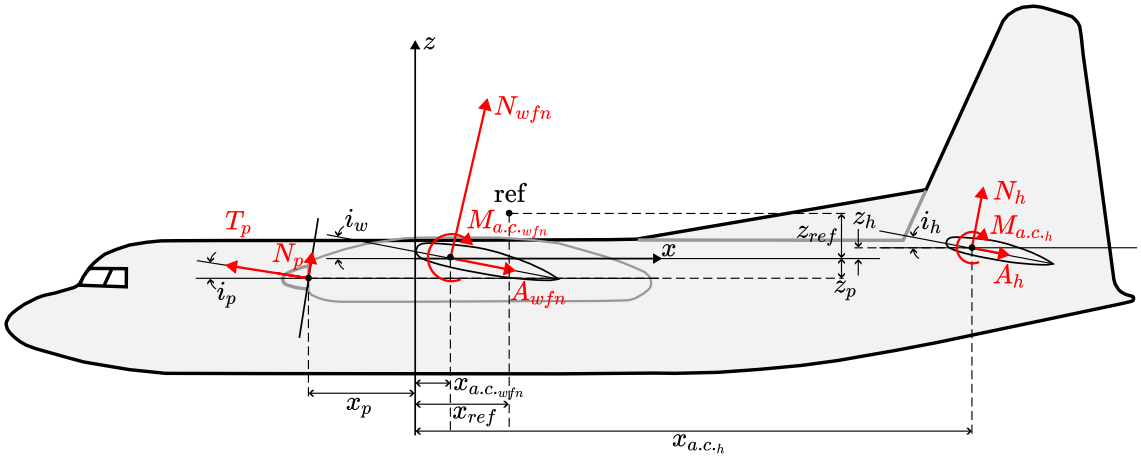

Figure D.1: A schematic of the wing, stabilizer and propeller forces and moments acting on the Fokker F-27.

The moment around the reference point is taken in the body/fuselage coordinate system, since all the distances between the force application point are defined in this coordinate system. For notation simplicity, the positions of the a.c. are denoted as: $x_{a.c._{wfn}} = x_{wfn}$, $z_{a.c._{wfn}} = z_{wfn}$, $x_{a.c._h} = x_h$ and $z_{a.c._h} = z_h$. Taking the CW rotation as positive results in the moment balance:

$$\begin{aligned}\sum M \overset{\curvearrowright}{+} : M = {} & M_{a.c._{wfn}} + N_{wfn}\cos(i_w)\left(x_{ref} - x_{wfn}\right) - N_{wfn}\sin(i_w)\left(z_{ref} - z_{wfn}\right) - A_{wfn}\cos(i_w)\left(z_{ref} - z_{wfn}\right) \\ & - A_{wfn}\sin(i_w)\left(x_{ref} - x_{wfn}\right) + M_{a.c._h} + N_h\cos(i_h)\left(x_{ref} - x_h\right) + N_h\sin(i_h)\left(z_{ref} - z_h\right) \\ & + A_h\cos(i_h)\left(z_{ref} - z_h\right) - A_h\sin(i_h)\left(x_{ref} - x_h\right) + T\cos(i_p)\left(z_{ref} - z_p\right) + T\sin(i_p)\left(x_{ref} - x_p\right) + \\ & N_p\cos(i_p)\left(x_{ref} - x_p\right) - N_p\sin(i_p)\left(z_{ref} - z_p\right)\end{aligned}$$

Non-dimensionalizing the moment balance by dividing by $q_w S_w \bar{c}$, yields Equation D.1.

$$\begin{aligned} C_{M_{tot}} = C_{M_{a.c._{wfn}}} &+ C_{N_{wfn}} \cos(i_w) \frac{(x_{ref} - x_{wfn})}{\bar{c}} - C_{N_{wfn}} \sin(i_w) \frac{(z_{ref} - z_{wfn})}{\bar{c}} \\ -C_{A_{wfn}} \sin(i_w) &\frac{(x_{ref} - x_{wfn})}{\bar{c}} - C_{A_{wfn}} \cos(i_w) \frac{(z_{ref} - z_{wfn})}{\bar{c}} + C_{M_{a.c._h}} \frac{q_h}{q_w} \frac{S_h}{S_w} \\ +C_{N_h} \cos(i_h) &\frac{(x_{ref} - x_h)}{\bar{c}} \frac{q_h}{q_w} \frac{S_h}{S_w} + C_{N_h} \sin(i_h) \frac{(z_{ref} - z_h)}{\bar{c}} \frac{q_h}{q_w} \frac{S_h}{S_w} \\ +C_{A_h} \sin(i_w) &\frac{(x_{ref} - x_h)}{\bar{c}} \frac{q_h}{q_w} \frac{S_h}{S_w} - C_{A_h} \cos(i_h) \frac{(z_{ref} - z_h)}{\bar{c}} \frac{q_h}{q_w} \frac{S_h}{S_w} \\ &+ T_c \cos(i_p) \left(\frac{z_{ref} - z_p}{\bar{c}} \right) + T_c \sin(i_p) \left(\frac{x_{ref} - x_p}{\bar{c}} \right) \\ &+ C_{n_p} \cos(i_p) \left(\frac{x_{ref} - x_p}{\bar{c}} \right) + C_{n_p} \sin(i_p) \left(\frac{z_{ref} - z_p}{\bar{c}} \right) \end{aligned} \tag{D.1}$$

The normal and tangential forces become normal and tangential force coefficients C_N, C_A. The terms belonging to the horizontal stabilizer have the additional terms $\frac{q_h}{q_w}$, $\frac{S_h}{S_w}$. Note that the propeller thrust and normal force coefficients T_c and C_N are normalized with respect to the wing parameters in Equation D.1. When assuming that:

- The AoA α is small:

$$C_L = C_N \cos(\alpha) - C_A \sin(\alpha) \approx C_N,$$
$$C_D = C_A \cos(\alpha) + C_N \sin(\alpha) \approx C_A,$$

- The drag force is much smaller than the lift force: $C_D << C_L$,
- The incidence angle of the wing is small: $i_w \approx 0$,

and when considering the following known facts on the F-27:

- The moment around the a.c. of the horizontal stabilizer is zero since the airfoil of the horizontal stabilizer is symmetric: $C_{M_{a.c._h}} = 0$,
- The incidence angle of the horizontal stabilizer is zero: $i_h = 0$,
- The incidence angle of the propeller is zero: $i_p = 0$,

a simplified expression, Equation D.2, can be obtained for the moment coefficient of the F-27.

$$C_M = C_{M_{a.c._{wfn}}} + C_{L_{\alpha_{wfn}}} (\alpha - \alpha_0) \frac{x_{ref} - x_{wfn}}{\bar{c}_w} + C_{L_{\alpha_h}} (\alpha - \varepsilon + i_h) \frac{x_{ref} - x_h}{\bar{c}_w} \frac{q_h}{q_w} \frac{S_h}{S_w} + T_c \frac{z_{ref} + z_p}{\bar{c}_w} + C_{N_p} \frac{x_{ref} + x_p}{\bar{c}_w} \tag{D.2}$$

Where the WFN and horizontal stabilizer lift is substituted with $C_{L_{wfn}} = C_{L_{\alpha_{wfn}}} (\alpha - \alpha_0)$, $C_{L_h} = C_{L_{\alpha_h}} (\alpha - \varepsilon + i_h)$ [39]. Highlighting the importance of the lift curve slopes, the zero-lift AoA and the downwash at the horizontal tail.

Taking the derivative of Equation D.2 with respect to α results in an equation for the LSS, see Equation D.3. Showing that the LSS is a function of the lift slope of the WFN combination, the stabilizer and the propeller forces.

$$C_{M_\alpha} = C_{L_{\alpha_{wfn}}} \frac{x_{ref} - x_{wfn}}{\bar{c}_w} + C_{L_{\alpha_h}} (-\varepsilon + i_h) \frac{x_{ref} - x_h}{\bar{c}_w} \frac{q_h}{q_w} \frac{S_h}{S_w} + T_{c_\alpha} \frac{z_{ref} + z_p}{\bar{c}_w} + C_{N_{p\alpha}} \frac{x_{ref} + x_p}{\bar{c}_w} \tag{D.3}$$